In-silico design of electrode meso-arquitecture for shape morphing dielectric elastomers

J. Martínez-Frutos[†1], R. Ortigosa[†2], A. J. Gil[‡3]

† *Computational Mechanics and Scientific Computing Group,*
Technical University of Cartagena, Campus Muralla del Mar, 30202, Cartagena (Murcia), Spain
‡ *Zienkiewicz Centre for Computational Engineering, College of Engineering*
Swansea University, Bay Campus, SA1 8EN, United Kingdom

Abstract

This paper presents a novel in-silico tool for the design of complex multilayer Dielectric Elastomers (DEs) characterised by recently introduced layer-by-layer reconfigurable electrode meso-arquitectures. Inspired by cutting-edge experimental work at Clarke Lab (Harvard) [21], this contribution introduces a novel approach underpinned by a diffuse interface treatment of the electrodes, whereby a spatially varying electro-mechanical free energy density is introduced whose active properties are related to the electrode meso-architecture of choice. State-of-the-art phase-field optimisation techniques are used in conjunction with the latest developments in the numerical solution of electrically stimulated DEs undergoing large (potentially extreme) deformations, in order to address the challenging task of finding the most suitable electrode layer-by-layer meso-architecture that results in a specific three-dimensional actuation mode. The paper introduces three key novelties. First, the consideration of the phase-field method for the implicit definition of reconfigurable electrodes placed at user-defined interface regions. Second, the extension of the electrode in-surface phase-field functions to the surrounding dielectric elastomeric volume in order to account for the effect of the presence (or absence) of electrodes within the adjacent elastomeric layers. Moreover, an original energy interpolation scheme of the free energy density is put forward where only the electromechanical contribution is affected by the extended phase-field function, resulting in an equivalent spatially varying active material formulation. Third, consideration of a non-conservative Allen-Cahn type of law for the evolution of the in-surface electrode phase field functions, adapted to the current large strain highly nonlinear electromechanical setting. A series of proof-of-concept examples (in both circular and squared geometries) are presented in order to demonstrate the robustness of the methodology and its potential as a new tool for the design of new DE-inspired soft-robotics components. The ultimate objective is to help thrive the development of this technology through the in-silico production of voltage-tunable (negative and positive Gaussian curvature) DEs shapes beyond those obtained solely via trial-and-error experimental investigation.

Keywords: Electrode meso-architecture; Shape Morphing; Dielectric Elastomer; Phase-Field; Topology Optimisation

1. Introduction

Since the early 1940s, the field of robotics has evidenced a paradigm shift from conventional hard robotics to soft robotics, through the exploration of machines or components with biomimetic

[1]Corresponding author: jesus.martinez@upct.es
[2]Corresponding author: rogelio.ortigosa@upct.es
[3]Corresponding author: a.j.gil@swansea.ac.uk

dexterous features capable of superseding the ability of humans whilst safely interacting with them. Dielectric Elastomers (DEs) [24, 29, 44, 45, 58] have been identified as excellent candidates for their use as soft robotics components [13, 15, 46, 52]. DEs represent an important family of Electro Active Polymers (EAPs), a well-known sub-group within the wider spectrum of soft smart materials. Since their discovery, DEs have demonstrated outstanding actuation capabilities which, in conjunction with their low stiffness, make them ideal for their application in the field of soft robotics. However, their potential use is not strictly limited to the field of electrically induced actuation, as they have been successfully used as Braille displays, deformable lenses, haptic devices and energy generators, to name but a few [37].

DEs exhibit electrically induced deformations triggered by Coulomb forces developed between two oppositely charged electrodes placed across the thickness of a typically thin DE layer. Coulomb forces induce thinning across the thickness of the DE which, due to the near-incompressibility of the elastomeric material, lead to in-plane expansion, potentially resulting in extremely large area expansions for highly compliant DEs [24, 27, 28]. For the case of nearly flat DE designs, the electric field remains mostly homogenous everywhere within the elastomeric material and, therefore, the electrically induced deformation remains also homogeneous (prior to the development of wrinkles associated with the onset of geometrical instability [28, 47, 65]). The attachment of passive elastomeric layers lead to the development of slightly more complex electrically induced three dimensional bending deformations. As an example, the manufacturing of tunable lenses [43, 55] via the use of DEs has been identified as a field of immediate application for this type of technology, where the inherent lens' curvature gradually evolves according to the application of external electric stimuli. However, more advanced actuation modes are still hindered by the relatively homogeneous electric field distribution across the DE device.

With that in mind, very recent research at Clarke Lab (Harvard) [21] has sought the introduction of new technology capable of generating highly in-homogeneous electric field distributions, through a layer-by-layer (or multi-layer) layout comprising a set of elastomeric DE layers intercalating compliant electrodes (of alternating polarity) and with different shapes. Under this radically new engineering design approach, the attainability of more complex shapes under the application of electric stimuli on geometrically complex electrodes is contingent upon the expertise and physical intuition of the researcher responsible of devising a suitable internal electrode meso-architecture. This expertise and physical intuition has allowed Clarke et. al. [21] to conceive electrode meso-architectures enabling actuated shapes far more sophisticated than those generated by classical electrode layouts (see Figure 1).

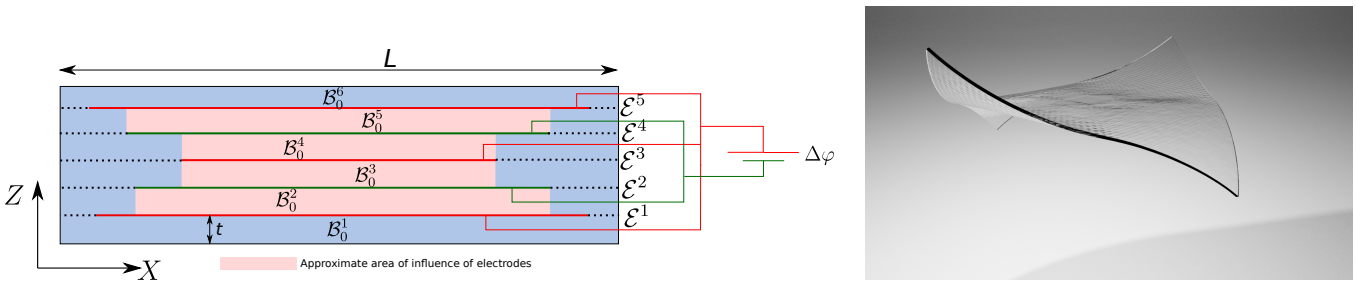

(a) (b)

Figure 1: A generalizable method for shape morphing of thin sheets of elastomer by creating spatially varying internal electric field. (a) A multilayered structure of circular elastomer sheets interleaved with concentric, interdigitated electrodes of decreasing radii with height. The electric field is primarily concentrated in the regions of overlap between the adjacent electrodes as illustrated by the so-called *area of influence of electrodes*. (b) Applying a voltage to the electrodes the elastomeric squared device induces a positive and negative Gaussian curvature (simulation) that increases with increasing voltage.

However, as it has been acknowledged in [21], the attainability of more complex electrically induced morphologies cannot simply rely on useful and valuable intuition and physical arguments.

Mathematical tools such as Topology Optimisation (TO) can clearly aid in the design, that is, can assist experienced researchers to conceive novel internal electrode meso-architectures enablers of shapes otherwise unachievable. As a result, this paper represents a first attempt at using TO as a means to obtaining optimal internal electrode layer-by-layer meso-architectures for reconfigurable shape morphing DEs. Recently, the work in Reference [14] made use of the level-set method for the optimal design of electrodes in the case where in-plane displacements of non-multilayered DEs were sought. A crucial challenge is the definition of the electrodes, whose position evolves during the TO process. In this paper, we advocate for a novel approach underpinned by a diffuse interface treatment of the electrodes, whereby a spatially varying electro-mechanical free energy density is introduced whose active properties are related to the electrode meso-architecture of choice. With that in mind, in-surface phase-field functions are used for the implicit definition of the electrodes placed at interface regions between adjacent elastomeric layers. Next, a Laplacian type extension of the surface-restricted phase-field functions to the volume of the surrounding elastomeric layers is formulated in order to incorporate the effect of the presence (or absence) of electrodes within the free energy density of the DE.

With regards to TO of smart materials, there is a wide spectrum of robust approaches available [1, 66], ranging from density-based methods with the Solid Isotropic Material with Penalisation (SIMP) method as their maximum representative [3], level-set methods [2, 62], phase-field methods [10, 60], topological derivative methods [59] and evolutionary methods [35]. We hereby provide a non exhaustive list of scientific works where TO has been applied with the aforementioned aim. Kang and Wang [23] used the SIMP method for the topology optimisation of piezoelectric ceramics, an electro-active material which, unlike EAPs, is restricted to scenarios characterised by very small deformations/displacements. A comparison is carried out between bi-morph and multilayered configurations in order to improve the action properties of the resulting device. The works in references [36] and [64] investigate TO of piezoelectric ceramics and flexoelectric materials. Zhang et. al. also investigated TO of piezoelectric sensors with active vibration control purposes. Other works [16, 17, 25, 53] have investigated the simultaneous optimisation of polarisation and layout of piezoelectric ceramics over a fixed host (passive) material, and when the host structure is also included in the optimisation process [48–50]. Furthermore, the work in [51] carries out the TO of piezoelectric ceramic-based micro-grippers considering large displacements but small deformations. Some recent works include the TO design of thermoelectric coolers and generators [30–32]. More recently, some works have ventured into the TO of dielectric elastomers. For instance, the work in [63] delves into the TO of these materials with the aim of maximising the electrically induced rotation of a rotary device. Extremely interesting is the work in [9], where the TO is applied with the objective of conceiving intelligent microstructures for the design of wide tunable band gaps. In this paper, we advocate for a phase field Allen-Cahn type evolution law [60] for the surface-restricted phase-field functions, adapted to the current DE multiphysics electro-mechanical setting.

With the aim of modelling more complex actuation scenarios in DEs, the use of computational methods constructed on the basis of variational principles is nowadays acknowledged as the preferred method of choice [11, 12, 18, 19, 34, 61]. In the most classical formulation, displacements and the scalar electric potential [18, 61] are regarded as the unknown fields. In this formulation, the constitutive information is encapsulated in the free energy density via its invariant-based representation depending upon kinematic strain measures and the Lagrangian electric field [61]. The nonlinear nature of the coupled electromechanical free energy density fosters its eventual loss of convexity with respect to the deformation gradient tensor at a given electrical excitation, leading to physically-based electromechanical instabilities. Beyond the onset of these instabilities, the constitutive model can potentially exhibit loss of ellipticity, which will reflect in spurious numerical results. Under these extreme scenarios, special care needs to be taken for the definition of the electromechanical constitutive law of a DE. For instance, inspired from the field of

polyconvexity in nonlinear elasticity, the authors in Reference [20] postulate sufficient convexity conditions that preclude *ab initio* the loss of ellipticity of the internal energy functional for the entire range of deformations and electric fields. In this paper, and without loss of generality, we do not contemplate these extreme scenarios. Hence, commonly used free energy densities will be used. Furthermore, more complex computational formulations than the classical two-field displacement-potential formulation have been employed for the numerical analysis of DEs. The reader is referred to References [38, 40] where, in addition to these fields, strains and the electric field, in conjunction with their work conjugates are also part of the set of unknown fields, with the aim of circumventing drawbacks inherent to low order displacement-potential formulations. In addition, Reference [47] establishes a comprehensive comparison between truly high order displacement-potential formulations and the mixed formulations in [40].

The layout of this paper is as follows: Section 2 introduces the governing equations in nonlinear reversible electro-mechanics and the variational formulation adopted in the paper, namely in terms of the displacement and the scalar electric potential. Section 3 describes the layer-by-layer design layout and introduces two different modelling approaches. A sharp interface treatment of the electrodes will be briefly discussed first followed by a diffuse interface treatment, which will be discussed in depth, where the inclusion of electrodes is described by a spatially varying electro-mechanical free energy density whose active properties are related to the electrode meso-architecture of choice. Section 4 describes the TO approach employed in the paper, characterised by the use of in-surface phase field functions used to describe the presence (or absence) of electrodes in the interface between adjacent elastomeric layers. The Section concludes with an algorithmic flowchart that summarises the in-silico modelling approach. Section 5 presents a series of numerical examples in order to demonstrate the robustness of the proposed methodology and present various sophisticated electrode meso-architectures for complex three dimensional actuation modes. Section 6 provides some concluding remarks and future lines of research. Finally, Appendix 6 summarises the Finite Element spatial discretisation technique.

2. Governing equations in nonlinear reversible electro-mechanics

This section introduces the fundamental equations governing the response of a Dielectric Elastomer (DE) actuated through an electric field generated via the positioning of electrodes *only* on some parts of the outer boundary of the DE. For simplicity, the electro-mechanical properties of the DE are considered homogenous, namely, spatially independent, and the electro-mechanical coupling to be reversible, disregarding thus any time-history effects. A differential based description of the governing equations is presented first, followed by appropriate variational statements more amenable to Finite Element implementation and large scale three-dimensional simulations.

2.1. Differential governing equations in nonlinear electromechanics

Let us consider the motion (actuation) of a generic DE with reference configuration $\mathcal{B}_0 \subset \mathbb{R}^3$ and boundary $\partial\mathcal{B}_0$ with unit outward normal $\boldsymbol{N}$ (refer to Figure 1). After the motion, the DE occupies a deformed configuration $\mathcal{B} \subset \mathbb{R}^3$ with boundary $\partial\mathcal{B}$ and unit outward normal $\boldsymbol{n}$. The motion of the DE is defined by a deformation mapping $\boldsymbol{\phi}$ which relates material particles $\boldsymbol{X} \in \mathcal{B}_0$ to the deformed configuration $\boldsymbol{x} \in \mathcal{B}$ according to $\boldsymbol{x} = \boldsymbol{\phi}(\boldsymbol{X})$. Associated with the mapping $\boldsymbol{\phi}(\boldsymbol{X})$, we introduce the deformation gradient tensor $\boldsymbol{F}$ [8], the co-factor $\boldsymbol{H}$ and its Jacobian J as

$$\boldsymbol{F} = \boldsymbol{\nabla}_0 \boldsymbol{\phi}; \qquad \boldsymbol{H} = \frac{1}{2}\boldsymbol{F} \times \boldsymbol{F}; \qquad J = \frac{1}{3}\boldsymbol{H} : \boldsymbol{F}, \tag{1}$$

where $\boldsymbol{\nabla}_0$ represents the material gradient operator, namely $\boldsymbol{\nabla}_0(\bullet) = \partial_{\boldsymbol{X}}(\bullet)$, $\times$ represents a tensor cross product operation [6, 7] between second order tensors defined as $(\boldsymbol{A} \times \boldsymbol{B})_{iI} =$

$\mathcal{E}_{ijk}\mathcal{E}_{IJK}A_{jJ}B_{kK}$, $\forall \boldsymbol{A}, \boldsymbol{B} \in \mathbb{R}^{3\times 3}$, where $\mathcal{E}_{ijk}$ (or $\mathcal{E}_{IJK}$) symbolises the third-order alternating tensor components and the use of repeated indices implies summation[4]. As it will be shown in Section 2.2, the triad of deformation measures $\{\boldsymbol{F}, \boldsymbol{H}, J\}$ is essential in the definition of the constitutive model of a DE.

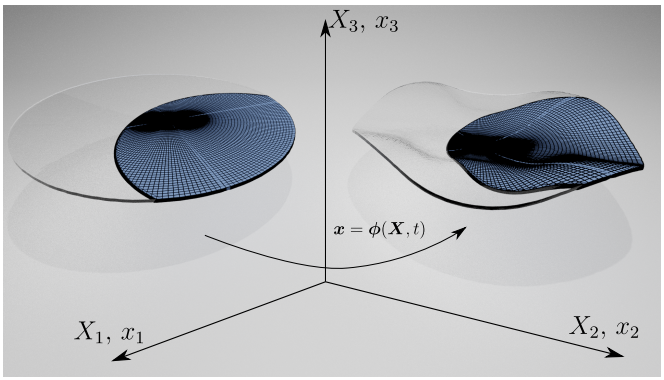

Figure 2: Deformation mapping $\boldsymbol{\phi}(\boldsymbol{X})$ for the DE in material configuration (left) and deformed configuration (right).

The electro-mechanical boundary value problem describing the response of the DE is comprised of a set of partial differential equations and associated boundary conditions. Specifically, in the absence of inertia effects, the mechanical response of the DE is represented by

$$\boldsymbol{F} = \boldsymbol{\nabla}_0 \boldsymbol{\phi}; \qquad \text{in } \mathcal{B}_0; \tag{2a}$$

$$\mathrm{DIV}\boldsymbol{P} + \boldsymbol{f}_0 = \boldsymbol{0}; \qquad \text{in } \mathcal{B}_0; \tag{2b}$$

$$\boldsymbol{P}\boldsymbol{N} = \boldsymbol{t}_0; \qquad \text{on } \partial_{\boldsymbol{t}}\mathcal{B}_0; \tag{2c}$$

$$\boldsymbol{\phi} = \bar{\boldsymbol{\phi}}^b; \qquad \text{on } \partial_{\boldsymbol{\phi}}\mathcal{B}_0, \tag{2d}$$

where (2a) represents the kinematic compatibility equation and (2b) the quasi-static version of the conservation of linear momentum in a Lagrangian description. In above equations, $\boldsymbol{f}_0$ represents a body force per unit undeformed volume, $\boldsymbol{P}$ is the first Piola-Kirchhoff stress tensor, $\boldsymbol{t}_0$ is a possible external traction vector per unit undeformed area $\partial_{\boldsymbol{t}}\mathcal{B}_0 \subset \partial\mathcal{B}_0$ and $\bar{\boldsymbol{\phi}}^b$ a possible external Dirichlet type boundary condition on $\partial_{\boldsymbol{\phi}}\mathcal{B}_0 \subset \partial\mathcal{B}_0$, with $\partial_{\boldsymbol{t}}\mathcal{B}_0 \cup \partial_{\boldsymbol{\phi}}\mathcal{B}_0 = \partial\mathcal{B}_0$ and $\partial_{\boldsymbol{t}}\mathcal{B}_0 \cap \partial_{\boldsymbol{\phi}}\mathcal{B}_0 = \emptyset$. Furthermore, conservation of angular momentum entails the well-known tensor condition $\boldsymbol{\sigma} = \boldsymbol{\sigma}^T$, where the Cauchy stress tensor is related with the first Piola-Kirchhoff stress tensor $\boldsymbol{P}$ through the standard Piola transformation $\boldsymbol{\sigma} = J^{-1}\boldsymbol{P}\boldsymbol{F}^T$.

Similarly, and in the absence of magnetic effects, the electrical response of the DE is represented by

$$\boldsymbol{E}_0 = -\boldsymbol{\nabla}_0 \varphi; \qquad \text{in } \mathcal{B}_0; \tag{3a}$$

$$\mathrm{DIV}\boldsymbol{D}_0 - \rho_0 = 0; \qquad \text{in } \mathcal{B}_0; \tag{3b}$$

$$\boldsymbol{D}_0 \cdot \boldsymbol{N} = -\omega_0; \qquad \text{on } \partial_\omega \mathcal{B}_0; \tag{3c}$$

$$\varphi = \bar{\varphi}^b; \qquad \text{on } \partial_\varphi \mathcal{B}_0, \tag{3d}$$

where (3a) and (3b) denote the quasi-static version of the Gauss' and Faraday's laws in a Lagrangian description. In above equations, φ represents an scalar electric potential, $\boldsymbol{E}_0$ denotes

[4]In addition, throughout the paper, the symbol $(\cdot)$ indicates the scalar product or contraction of a single index $\boldsymbol{a}\cdot\boldsymbol{b} = a_i b_i$; the symbol $(:)$, double contraction of two indices $\boldsymbol{A}:\boldsymbol{B} = A_{ij}B_{ij}$; the symbol $(\times)$, the cross product between vectors $(\boldsymbol{a}\times\boldsymbol{b})_i = \mathcal{E}_{ijk}a_j b_k$; and the symbol $(\otimes)$, the outer or dyadic product $(\boldsymbol{a}\otimes\boldsymbol{b})_{ij} = a_i b_j$.

the material electric field, $\boldsymbol{D}_0$ the material electric displacement, ρ_0 represents an electric charge per unit of undeformed volume, ω_0 an electric charge per unit of undeformed area $\partial_\omega \mathcal{B}_0 \subset \partial\mathcal{B}_0$ and $\bar{\varphi}^b$ a suitable external potential applied on electrodes for the actuation of the DE. These electrodes are positioned on $\partial_\varphi \mathcal{B}_0 \subset \partial\mathcal{B}_0$, such that $\partial_\omega \mathcal{B}_0 \cup \partial_\varphi \mathcal{B}_0 = \partial\mathcal{B}_0$ and $\partial_\omega \mathcal{B}_0 \cap \partial_\varphi \mathcal{B}_0 = \emptyset$. In above equations, both $\boldsymbol{D}_0$ and $\boldsymbol{E}_0$ can be related with their spatial counterparts $\boldsymbol{D}$ and $\boldsymbol{E}$, respectively, through the following standard relations $\boldsymbol{E} = \boldsymbol{F}^{-T}\boldsymbol{E}_0$ and $\boldsymbol{D} = J^{-1}\boldsymbol{F}\boldsymbol{D}_0$ [18, 19][5].

For closure of the coupled boundary value problem defined by equations (2) and (3), a constitutive law is required in order to relate the first Piola-Kirchhoff stress tensor $\boldsymbol{P}$ and the electric displacement $\boldsymbol{D}_0$ with the deformation gradient tensor $\boldsymbol{F}$ and the electric field $\boldsymbol{E}_0$, namely $\boldsymbol{P} = \boldsymbol{P}(\boldsymbol{F}, \boldsymbol{E}_0)$ and $\boldsymbol{D}_0 = \boldsymbol{D}_0 = (\boldsymbol{F}, \boldsymbol{E}_0)$, which will be presented next.

2.2. Constitutive equations in reversible nonlinear electromechanics

In the case of reversible nonlinear electromechanics, the constitutive law is traditionally [18, 22, 26, 56, 57] introduced through the definition of a suitable free energy density per unit undeformed volume $\mathcal{B}_0$, denoted as $\Psi = \Psi(\boldsymbol{X}, \boldsymbol{F}, \boldsymbol{E}_0)$. For the special case of a homogeneous DE, with no spatially varying electro-mechanical properties, the free energy density can be simplified as $\Psi = \Psi(\boldsymbol{F}, \boldsymbol{E}_0)$. In this context, the first Piola-Kirchhoff stress tensor $\boldsymbol{P}$ and the electric displacement field $\boldsymbol{D}_0$ (energy dual/conjugates of $\boldsymbol{F}$ and $\boldsymbol{E}_0$, respectively) emerge form the first derivatives of the free energy density as

$$\boldsymbol{P}(\boldsymbol{F}, \boldsymbol{E}_0) = \partial_{\boldsymbol{F}}\Psi(\boldsymbol{F}, \boldsymbol{E}_0); \qquad \boldsymbol{D}_0(\boldsymbol{F}, \boldsymbol{E}_0) = -\partial_{\boldsymbol{E}_0}\Psi(\boldsymbol{F}, \boldsymbol{E}_0), \tag{4}$$

where $\partial_{\boldsymbol{A}}(\bullet)$ denotes the partial derivative of $(\bullet)$ with respect to the field $\boldsymbol{A}$. Furthermore, the second partial derivatives of the free energy density yield the so-called constitutive tensors, namely the fourth order elasticity tensor $\boldsymbol{\mathcal{C}}$, the third order piezoelectric tensor $\boldsymbol{\mathcal{P}}$ and the second order dielectric tensor $\boldsymbol{\varepsilon}$, defined respectively as

$$\boldsymbol{\mathcal{C}}(\boldsymbol{F}, \boldsymbol{E}_0) = \partial^2_{\boldsymbol{F}\boldsymbol{F}}\Psi(\boldsymbol{F}, \boldsymbol{E}_0); \quad \boldsymbol{\mathcal{P}}(\boldsymbol{F}, \boldsymbol{E}_0) = -\partial^2_{\boldsymbol{E}_0\boldsymbol{F}}\Psi(\boldsymbol{F}, \boldsymbol{E}_0); \quad \boldsymbol{\varepsilon}(\boldsymbol{F}, \boldsymbol{E}_0) = -\partial^2_{\boldsymbol{E}_0\boldsymbol{E}_0}\Psi(\boldsymbol{F}, \boldsymbol{E}_0). \tag{5}$$

Typically, the free energy density of a DE is additively decomposed into mechanical $\Psi_m(\boldsymbol{F})$ and electromechanical $\Psi_{em}(\boldsymbol{F}, \boldsymbol{E}_0)$ contributions as

$$\Psi(\boldsymbol{F}, \boldsymbol{E}_0) = \Psi_m(\boldsymbol{F}) + \Psi_{em}(\boldsymbol{F}, \boldsymbol{E}_0). \tag{6}$$

A commonly used model to define the mechanical Ψ_m contribution is the (isotropic) Mooney-Rivlin model [54] $\Psi_m = \Psi_m^{MR}$, defined as

$$\Psi_m^{MR}(\boldsymbol{F}) := \frac{\mu_1}{2}\left(II_{\boldsymbol{F}} - 3\right) + \frac{\mu_2}{2}\left(II_{\boldsymbol{H}} - 3\right) + f(J); \qquad f(J) = -\left(\mu_1 + 2\mu_2\right)\ln(J) + \frac{\lambda}{2}\left(J-1\right)^2, \tag{7}$$

with $II_{\boldsymbol{A}} = \boldsymbol{A} : \boldsymbol{A}$ and $\{\mu_1, \mu_2, \lambda\}$ are three material parameters. For the case of a DE, a commonly used model for the electromechanical contribution Ψ_{em} is that of an ideal dielectric $\Psi_{em} = \Psi_{em}^{ID}$, defined as

$$\Psi_{em}^{ID}(\boldsymbol{F}, \boldsymbol{E}_0) = -\frac{\varepsilon_r\varepsilon_0}{2J} II_{\boldsymbol{H}\boldsymbol{E}_0}; \qquad II_{\boldsymbol{H}\boldsymbol{E}_0} = \boldsymbol{H}\boldsymbol{E}_0 \cdot \boldsymbol{H}\boldsymbol{E}_0, \tag{8}$$

where ε_0 represents the electric permittivity of vacuum, being $\varepsilon_0 = 8.854 \times 10^{-12}\,\mathrm{Fm}^{-1}$, and ε_r the relative electric permittivity. Notice that material parameters $\{\mu_1, \mu_2, \lambda\}$ are related to the

[5] These relationships are particularly useful as Maxwell equations are typically understood in the current configuration.

Young's modulus E and Poisson ratio ν in the origin, namely when $\boldsymbol{F} = \boldsymbol{I}$ (being $\boldsymbol{I}$ the second order identity tensor) and $\boldsymbol{E}_0 = \boldsymbol{0}$, as

$$\mu_1 + \mu_2 = \frac{E}{2(1+\nu)}; \qquad \lambda + 2\mu_2 = \frac{E\nu}{(1+\nu)(1-2\nu)}. \tag{9}$$

Although more sophisticated constitutive laws to those shown in (7) and (8) can be used to describe the response of a DE, see for instance [20, 39–41] for the use of Convex-Multivariable constitutive laws, the remainder of the paper is focused, without loss of generality, on the use of the simpler model defined by (7) and (8).

2.3. Variational formulation in reversible nonlinear electromechanics

In this section, we present the variational formulation associated with the solution of the system of nonlinear coupled equations (2) and (3). For simplicity, we use the variational formulation derived from the classical two-field variational principle with unknown fields $\boldsymbol{\phi} \in \mathbb{V}^{\boldsymbol{\phi}}$ and $\varphi \in \mathbb{V}^{\varphi}$, with $\mathbb{V}^{\boldsymbol{\phi}}, \mathbb{V}^{\varphi}$ suitable functional spaces satisfying the essential boundary conditions in (2d) and (3d), namely

$$\mathbb{V}^{\boldsymbol{\phi}} = \{\boldsymbol{\phi} \in (H^1(\mathcal{B}_0))^3 : \text{s.t. (2d)}\}; \qquad \mathbb{V}^{\varphi} = \{\varphi \in H^1(\mathcal{B}_0) : \text{s.t. (3d)}\}. \tag{10}$$

The variational principle states[6]

$$\Pi(\boldsymbol{\phi}^*, \varphi^*) = \inf_{\boldsymbol{\phi}} \sup_{\varphi} \left\{ \int_{\mathcal{B}_0} \Psi\left(\boldsymbol{F}, \boldsymbol{E}_0\right) \, dV - \Pi^m_{\text{ext}}\left(\boldsymbol{\phi}\right) - \Pi^{em}_{\text{ext}}\left(\varphi\right) \right\}, \tag{11}$$

where Π^m_{ext} and Π^{em}_{ext} represent the external work done due to mechanical and electrical actions, respectively, defined as

$$\Pi^m_{\text{ext}}\left(\boldsymbol{\phi}\right) = \int_{\mathcal{B}_0} \boldsymbol{f}_0 \cdot \boldsymbol{\phi} \, dV + \int_{\partial_t \mathcal{B}_0} \boldsymbol{t}_0 \cdot \boldsymbol{\phi} \, dA; \qquad \Pi^{em}_{\text{ext}}\left(\varphi\right) = -\int_{\mathcal{B}_0} \rho_0 \varphi \, dV - \int_{\partial_\omega \mathcal{B}_0} \omega_0 \varphi \, dA. \tag{12}$$

The stationary conditions of $\Pi(\boldsymbol{\phi}, \varphi)$ (11), stemming from its directional derivatives with respect to independent virtual variations $\delta\boldsymbol{\phi} \in \mathbb{V}^{\boldsymbol{\phi}}_0$ and $\delta\varphi \in \mathbb{V}^{\varphi}_0$ [7], yield the variational forms of the conservation of linear momentum and Gauss's law, namely

$$D\Pi(\boldsymbol{\phi}, \varphi)[\delta\boldsymbol{\phi}] = \int_{\mathcal{B}_0} \boldsymbol{P}\left(\boldsymbol{F}, \boldsymbol{E}_0\right) : \boldsymbol{\nabla}_0 \delta\boldsymbol{\phi} \, dV - D\Pi^m_{\text{ext}}\left(\boldsymbol{\phi}\right)[\delta\boldsymbol{\phi}] = 0; \tag{13a}$$

$$D\Pi(\boldsymbol{\phi}, \varphi)[\delta\varphi] = \int_{\mathcal{B}_0} \boldsymbol{D}_0\left(\boldsymbol{F}, \boldsymbol{E}_0\right) \cdot \boldsymbol{\nabla}_0 \delta\varphi \, dV - D\Pi^{em}_{\text{ext}}\left(\varphi\right)[\delta\varphi] = 0, \tag{13b}$$

where

$$D\Pi^m_{\text{ext}}\left(\boldsymbol{\phi}\right)[\delta\boldsymbol{\phi}] = \int_{\mathcal{B}_0} \boldsymbol{f}_0 \cdot \delta\boldsymbol{\phi} \, dV + \int_{\partial_t \mathcal{B}_0} \boldsymbol{t}_0 \cdot \delta\boldsymbol{\phi} \, dA; \tag{14a}$$

$$D\Pi^{em}_{\text{ext}}\left(\varphi\right)[\delta\varphi] = -\int_{\mathcal{B}_0} \rho_0 \delta\varphi \, dV - \int_{\partial_\omega \mathcal{B}_0} \omega_0 \delta\varphi \, dA. \tag{14b}$$

In order to solve the coupled system of nonlinear variational forms in (13) (the coupling and its nonlinear nature are induced by the constitutive relationships in (4)), use is made of a

[6] More accurate and sophisticated variational principles can also be employed, as previously presented by the authors in [40, 41].

[7] As usual, the subindex 0 for a functional space is used to indicate satisfaction of homogeneous essential boundary conditions.

Newton-Raphson k-iterative scheme where both variational forms are linearised with respect to incremental fields $\Delta\boldsymbol{\phi} \in \mathbb{V}_0^{\boldsymbol{\phi}}$ and $\Delta\varphi \in \mathbb{V}_0^{\varphi}$ as

$$D^2\Pi(\boldsymbol{\phi}^k, \varphi^k)[\delta\boldsymbol{\phi}; \Delta\boldsymbol{\phi}] + D^2\Pi(\boldsymbol{\phi}^k, \varphi^k)[\delta\boldsymbol{\phi}; \Delta\varphi] = -D\Pi(\boldsymbol{\phi}^k, \varphi^k)[\delta\boldsymbol{\phi}]; \tag{15a}$$

$$D^2\Pi(\boldsymbol{\phi}^k, \varphi^k)[\delta\varphi; \Delta\boldsymbol{\phi}] + D^2\Pi(\boldsymbol{\phi}^k, \varphi^k)[\delta\varphi; \Delta\varphi] = -D\Pi(\boldsymbol{\phi}^k, \varphi^k)[\delta\varphi], \tag{15b}$$

which permit the update of the solution fields $\boldsymbol{\phi}$ and φ at Newton-Raphson iteration k as

$$\boldsymbol{\phi}^{k+1} = \boldsymbol{\phi}^k + \Delta\boldsymbol{\phi}; \qquad \varphi^{k+1} = \varphi^k + \Delta\varphi. \tag{16}$$

In equations (15), the terms involving the second directional derivatives of the functional $\Pi(\boldsymbol{\phi}, \varphi)$ can be obtained as

$$\begin{aligned}
D^2\Pi(\boldsymbol{\phi}, \varphi)[\delta\boldsymbol{\phi}; \Delta\boldsymbol{\phi}] &= \int_{\mathcal{B}_0} \boldsymbol{\nabla}_0\delta\boldsymbol{\phi} : \boldsymbol{\mathcal{C}}\left(\boldsymbol{F}, \boldsymbol{E}_0\right) : \boldsymbol{\nabla}_0\Delta\boldsymbol{\phi}\, dV; \\
D^2\Pi(\boldsymbol{\phi}, \varphi)[\delta\boldsymbol{\phi}; \Delta\varphi] &= \int_{\mathcal{B}_0} \boldsymbol{\nabla}_0\delta\boldsymbol{\phi} : \boldsymbol{\mathcal{P}}^T\left(\boldsymbol{F}, \boldsymbol{E}_0\right) \cdot \boldsymbol{\nabla}_0\Delta\varphi\, dV; \\
D^2\Pi(\boldsymbol{\phi}, \varphi)[\delta\varphi; \Delta\boldsymbol{\phi}] &= \int_{\mathcal{B}_0} \boldsymbol{\nabla}_0\delta\varphi \cdot \boldsymbol{\mathcal{P}}\left(\boldsymbol{F}, \boldsymbol{E}_0\right) : \boldsymbol{\nabla}_0\Delta\boldsymbol{\phi}\, dV; \\
D^2\Pi(\boldsymbol{\phi}, \varphi)[\delta\varphi; \Delta\varphi] &= -\int_{\mathcal{B}_0} \boldsymbol{\nabla}_0\delta\varphi \cdot \boldsymbol{\varepsilon}\left(\boldsymbol{F}, \boldsymbol{E}_0\right) \boldsymbol{\nabla}_0\Delta\varphi\, dV,
\end{aligned} \tag{17}$$

with $\boldsymbol{\mathcal{C}}$, $\boldsymbol{\mathcal{P}}$ and $\boldsymbol{\varepsilon}$ defined in (5) and where $\left(\boldsymbol{\mathcal{P}}^T\right)_{jJI} = \left(\boldsymbol{\mathcal{P}}\right)_{IjJ}$.

3. Computational approaches for layer-by-layer layout

This section extends and generalises the concepts presented previously. Specifically, the restriction regarding the positioning of the electrodes *only* on some parts of the boundary of the DE will be lifted; and electrodes will be allowed to be placed inside the matrix of the DE. As it will be shown, the lifting of this restriction permits the development of sophisticated meso-architectures (i.e. elastomer and electrode distribution), paving the way towards the exploration of complex actuation patterns, otherwise inaccessible. In line with very recent work in [21], we consider a layer-by-layer *reconfigurable* design layout of the DE, as depicted in Figure 3. Specifically,

I The DE undeformed configuration $\mathcal{B}_0$ is comprised of the union of N_{L} elastomeric layers, defined by $\{\mathcal{B}_0^1, \ldots, \mathcal{B}_0^{N_L}\}$.

II Electrodes are intercalated between adjacent elastomer layers where tailor-made in-surface spatially varying electric potential will be applied.

III The thickness of the electrodes is regarded as negligible in comparison with that of the elastomeric layers. This permits the identification of the *surface* regions where the electrodes will be placed, denoted as $\{\mathcal{E}^1, \ldots, \mathcal{E}^{N_L-1}\}$, as the intersection between adjacent elastomeric layers, namely

$$\mathcal{E}^i = \bar{\mathcal{B}}_0^i \cap \bar{\mathcal{B}}_0^{i+1}; \qquad i = \{1, \ldots, N_{\mathrm{L}} - 1\}. \tag{18}$$

IV For simplicity, in this work, all electrode regions contained within a given interface surface are subjected to the same voltage value, either positive or negative in magnitude.

V Interaction between electrodes of opposite potential placed at non-adjacent layers cannot occur. This can be visualised in Figure 6. In that figure, for instance, layer $\mathcal{E}^1$ is blocked physically (in the Z direction) by layers $\mathcal{E}^2$ and $\mathcal{E}^3$, preventing its interaction with layer $\mathcal{E}^4$. Although this designing limitation is not general, it imposes that the actuation of the DE device is driven by the interaction between adjacent layers, which are indeed the ones subjected to the higher voltage gradients.

The outer boundary of the DE $\mathcal{B}_0$ is decomposed into a lateral boundary $\partial\mathcal{B}_0^l$, and top and bottom boundaries $\partial\mathcal{B}_0^t$ and $\partial\mathcal{B}_0^b$, respectively (see Figure 3), as

$$\partial\mathcal{B}_0 = \partial\mathcal{B}_0^t \cup \partial\mathcal{B}_0^b \cup \partial\mathcal{B}_0^l. \tag{19}$$

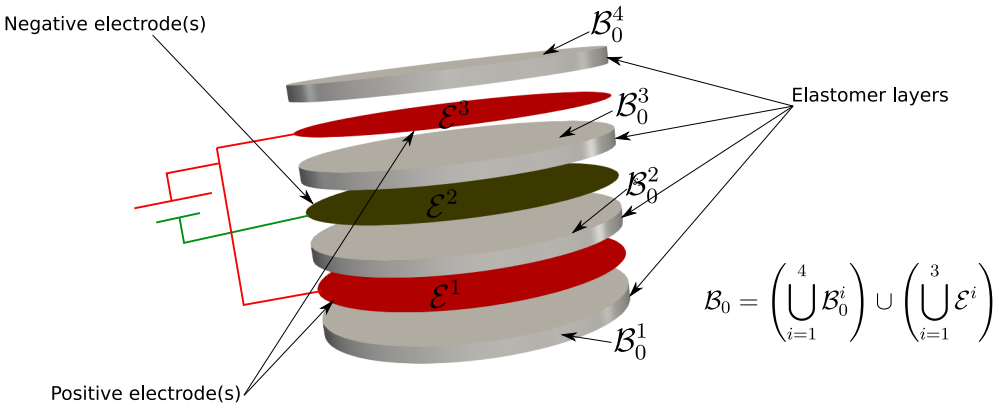

Figure 3: Example illustrating the initial (prior to optimisation) layer-by-layer DE layout: four layers of DE are considered $\{\mathcal{B}_0^1, \ldots, \mathcal{B}_0^4\}$, where three (infinitely) thin layers of electrodes are intercalated $\{\mathcal{E}^1, \ldots, \mathcal{E}^3\}$. All red electrodes are interconnected. All green electrodes (if there were more than one) are interconnected.

It is worthwhile emphasising that the interfaces $\mathcal{E}^i$ do not necessarily represent the actual electrode regions, but rather the latter must be understood as a *reconfigurable* subset of the former. This can be easily observed in Figure 4_a, where the green circular surface represents one of the interfaces $\mathcal{E}^i$, whilst the brown areas lying within it correspond to the actual electrode locations, with all of them subjected to the same voltage value. The reason for this spatial distribution of electrodes within every interface $\mathcal{E}^i$ is two-fold: i) in order to generate a tailor-made spatial variation of the electric field across each layer of dielectric elastomer $\mathcal{B}_0^i$, ultimately leading to non-conventional electrically actuated shapes and ii) in order to permit the possibility of reconfigurable designs where the actual electrode locations can be changed in position (within a given interface $\mathcal{E}^i$) at the will of the designer. Based on the above considerations **I-III**, we discuss next two different modelling approaches, depending on the treatment of the embedded electrodes, namely, *sharp* approach (refer to Section 3.1) and *diffuse* approach (refer to Section 3.2). In the *sharp* approach, the elastomeric layers are described with homogeneous (constant) active properties and the spatial variation of the actuating electric potential within an interface surface region is modelled via the use of spatially varying in-surface characteristic functions. On the contrary, in the *diffuse* approach, the actuating electric potential is assumed constant across the entire interface surface region and the elastomer layers are endowed with spatially varying active properties.

3.1. Sharp interface treatment of the electrodes

In this approach, actual electrodes within a given interface surface $\mathcal{E}^i$ are described via a characteristic function $\chi_{\mathcal{E}^i}(\boldsymbol{\xi})$, with discrete values $\{0, 1\}$ and $\boldsymbol{\xi} \in \mathcal{E}^i$. Every point $\boldsymbol{\xi} \in \mathcal{E}^i$ with a value of $\chi_{\mathcal{E}^i}(\boldsymbol{\xi}) = 1$ corresponds with the region $\mathcal{E}^i_{\text{Elec}} \subset \mathcal{E}^i$ where the electrode is actuated (i.e. a given voltage value is applied). On the other hand, every point $\boldsymbol{\xi} \in \mathcal{E}^i$ with a value of $\chi_{\mathcal{E}^i}(\boldsymbol{\xi}) = 0$ corresponds with the region of $\mathcal{E}^i$ where electrode collocation is avoided, that is

$$\forall \boldsymbol{\xi} \in \mathcal{E}^i, \begin{cases} \chi_{\mathcal{E}^i}(\boldsymbol{\xi}) = 1; & \text{if } \boldsymbol{\xi} \in \mathcal{E}^i_{\text{Elec}}; \\ \chi_{\mathcal{E}^i}(\boldsymbol{\xi}) = 0; & \text{if } \boldsymbol{\xi} \in \mathcal{E}^i \setminus \mathcal{E}^i_{\text{Elec}}. \end{cases} \tag{20}$$

Figure 5 illustrates the *extruded* spatial distribution of the regions $\mathcal{E}^i_{\text{Elec}}$ within each of the surfaces $\{\mathcal{E}^1, \ldots, \mathcal{E}^{N_L-1}\}$. In this figure, six layers of elastomer are considered, i.e. $N_L = 6$,

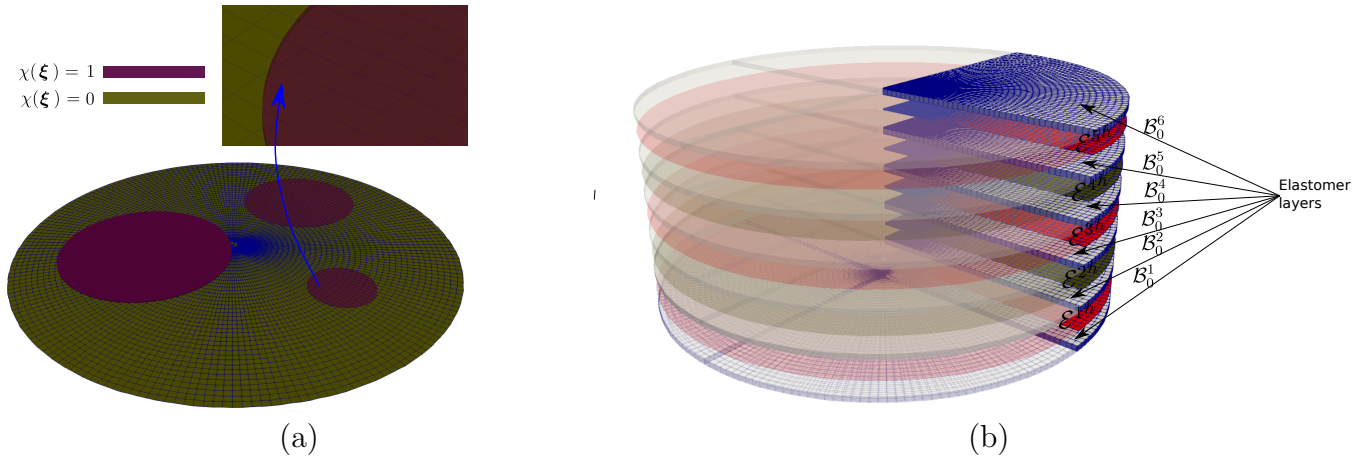

(a) (b)

Figure 4: (a) Surface region $\mathcal{E}^i$ and spatial distribution of electrodes of same voltage over $\mathcal{E}^i$ (brown regions); (b) Layer-by-layer discretisation DE devices complying with modelling assumptions **I-IV** described in Section 3.

which are separated by five interface (electrode) surfaces, i.e. $\{\mathcal{E}^1, \ldots, \mathcal{E}^5\}$. An important design/computational/manufacturing challenge resides on the application of the electric potential only in the regions defined by $\mathcal{E}^i_{\text{Elec}}$, whilst maintaining the remainder of the interface surface $\mathcal{E}^i \setminus \mathcal{E}^i_{\text{Elec}}$ not actuated. Referring to Figure 4$_a$, electrical potential must only be imposed in the brown regions contained within the interface surface region. Moreover, as shown in Figure 5, and following the modelling assumption **IV** presented above, all the electrodes with positive prescribed voltage $\bar{\varphi}$ are contained within the set of surface regions $\mathcal{E}^+ = \{\mathcal{E}^1, \mathcal{E}^3, \ldots, \mathcal{E}^{N_L-1}\}$, and all the electrodes under negative prescribed voltage are contained within the set of surface regions $\mathcal{E}^- = \{\mathcal{E}^2, \mathcal{E}^4, \ldots, \mathcal{E}^{N_L-2}\}$, i.e.

$$\varphi = \bar{\varphi}; \text{ on } \boldsymbol{\xi} \in \mathcal{E}^i \subset \mathcal{E}^+ : \chi_{\mathcal{E}^i}(\boldsymbol{\xi}) = 1; \qquad \varphi = -\bar{\varphi}; \text{ on } \boldsymbol{\xi} \in \mathcal{E}^i \subset \mathcal{E}^- : \chi_{\mathcal{E}^i}(\boldsymbol{\xi}) = 1. \tag{21}$$

The mechanical part of the boundary value problem describing the response of the layer-by-layer DE can be formulated by a careful extension of that in (2) as

$$\boldsymbol{F} = \boldsymbol{\nabla}_0 \boldsymbol{\phi}; \qquad \text{in } \mathcal{B}_0^j; \tag{22a}$$
$$\text{DIV}\boldsymbol{P}(\boldsymbol{F}, \boldsymbol{E}_0) + \boldsymbol{f}_0 = \boldsymbol{0}; \qquad \text{in } \mathcal{B}_0^j; \tag{22b}$$
$$\boldsymbol{P}\boldsymbol{N} = \boldsymbol{t}_0; \qquad \text{on } \partial_{\boldsymbol{t}}\mathcal{B}_0; \tag{22c}$$
$$\boldsymbol{\phi} = \bar{\boldsymbol{\phi}}^b; \qquad \text{on } \partial_{\boldsymbol{\phi}}\mathcal{B}_0; \tag{22d}$$
$$[\![\boldsymbol{\phi}]\!] = \boldsymbol{0}; \qquad \text{on } \mathcal{E}^i; \tag{22e}$$
$$[\![\boldsymbol{P}]\!]\, \boldsymbol{N}|_{\mathcal{E}^i} = \boldsymbol{0}; \qquad \text{on } \mathcal{E}^i, \tag{22f}$$

where equations (22e)-(22f) represent interface conditions introduced as a result of the layer-by-layer design fabrication process[8]. Equations (22a)-(22d) are identical to those already shown in (2), albeit particularised for the case of multiple ($i = 1 \ldots N_L - 1$, $j = 1 \ldots N_L$) elastomeric layers, and equations (22e)-(22f) represent appropriate jump conditions for the geometry and the traction vector, respectively, where the symbol $[\![\bullet]\!]$ is used to denote the jump of a field across the surface $\mathcal{E}^i$ and $\boldsymbol{N}|_{\mathcal{E}^i}$ its associated unit normal.

Analogously, the electrical part of the boundary value problem describing the response of the

[8]Notice that further kinematic jump conditions [5, 20] involving the jump in $\boldsymbol{F}$ and $\boldsymbol{H}$ could have been introduced in the case of using a more sophisticated mixed variational approach.

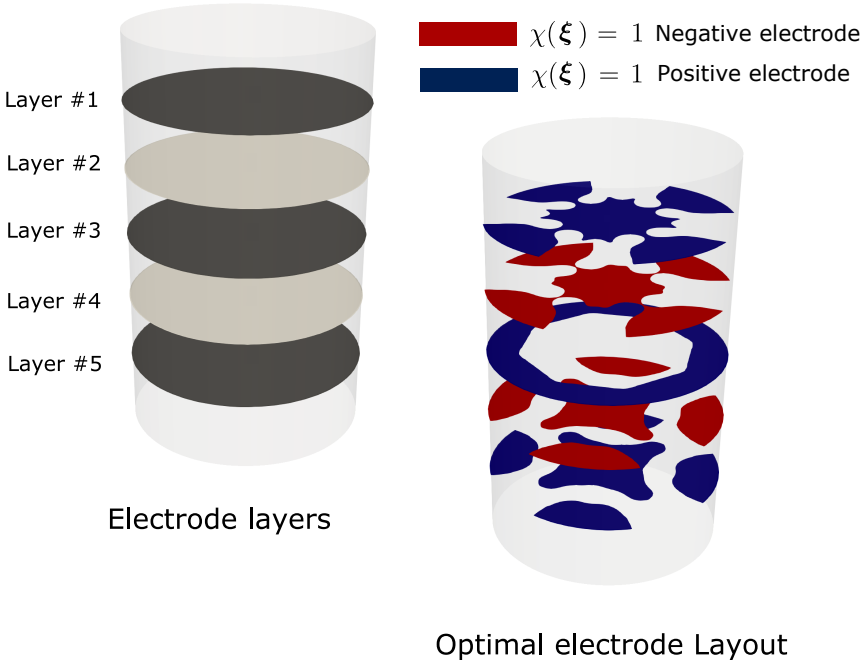

Figure 5: Layer-by-layer layout within the sharp interface setting. **Left**: DE device comprising six elastomer layers $\{\mathcal{B}_0^1, \dots, \mathcal{B}_0^6\}$ and five intercalated surface regions $\{\mathcal{E}^1, \dots, \mathcal{E}^5\}$. **Right**: final distribution of the characteristic function with value $\chi(\boldsymbol{\xi}) = 1$, representing the electrode regions $\{\mathcal{E}^1_{\text{Elec}}, \dots, \mathcal{E}^5_{\text{Elec}}\}$.

layer-by-layer DE can be formulated by a careful extension of that in (3) as

$$\boldsymbol{E}_0 = -\boldsymbol{\nabla}_0 \varphi; \qquad \text{in } \mathcal{B}_0^j; \tag{23a}$$

$$\text{DIV}\boldsymbol{D}_0(\boldsymbol{F}, \boldsymbol{E}_0) = \rho_0; \qquad \text{in } \mathcal{B}_0^j; \tag{23b}$$

$$\boldsymbol{D}_0 \cdot \boldsymbol{N} = -\omega_0; \qquad \text{on } \partial_\omega \mathcal{B}_0; \tag{23c}$$

$$\varphi = \bar{\varphi}^b; \qquad \text{on } \partial_\varphi \mathcal{B}_0; \tag{23d}$$

$$\varphi = \pm\bar{\varphi}; \qquad \text{on } \boldsymbol{\xi} \in \mathcal{E}^i \subset \mathcal{E}^{\pm} : \chi_{\mathcal{E}^i}(\boldsymbol{\xi}) = 1; \tag{23e}$$

$$[\![\varphi]\!] = 0; \qquad \text{on } \boldsymbol{\xi} \in \mathcal{E}^i : \chi_{\mathcal{E}^i}(\boldsymbol{\xi}) = 0; \tag{23f}$$

$$[\![\boldsymbol{D}_0]\!] \cdot \boldsymbol{N}|_{\mathcal{E}^i} = 0; \qquad \text{on } \boldsymbol{\xi} \in \mathcal{E}^i : \chi_{\mathcal{E}^i}(\boldsymbol{\xi}) = 0, \tag{23g}$$

where equation (23e)-(23g) represent interface conditions introduced as a result of the layer-by-layer design fabrication process[9]. Equations (23a)-(23d) are identical to those shown in (3), albeit particularised for the case of multiple elastomeric layers ($i = 1 \dots N_L - 1$, $j = 1 \dots N_L$) and equation (23e) denotes the application of electrical potential in positive and negative electrode regions, defined by suitable in-surface characteristic functions $\chi_{\mathcal{E}^i}$.

The expression for the first Piola-Kirchhoff stress tensor and the electric displacement (within every elastomeric layer $\mathcal{B}_0^j$) can be obtained from the use of the homogeneous constitutive model described in Section 2.2. Naturally, a challenge (specially for the case of reconfigurable electrode positioning) remains as to the application of the electric potential on interface regions via the presence of the characteristic function, that is, equation (23e).

[9]Notice that further electrical jump conditions [20] involving the jump in $\boldsymbol{E}_0$ could have been introduced in the case of using a more sophisticated mixed variational approach.

3.2. Diffuse interface treatment of the electrodes

In design practice, the thickness t^j of the elastomeric layers $\mathcal{B}_0^j$ is very small when compared to the in-plane characteristic dimension of the overall DE, denoted as L, namely $t^j << L$. Under this scenario, the existence of non-zero electric displacement $\boldsymbol{D}_0$ (and thus non-zero electric field $\boldsymbol{E}_0$) is restricted to the vicinity of the electrode regions, hereby denoted as the ***region of influence of electrodes*** (see Figure 6$_a$), rapidly decreasing to zero away from this region of influence, namely $\boldsymbol{D}_0 \to \boldsymbol{0}$. This physical consideration justifies the use of an alternative diffuse approach for the treatment of the electrode regions, which will be constructed based on the following key ingredients:

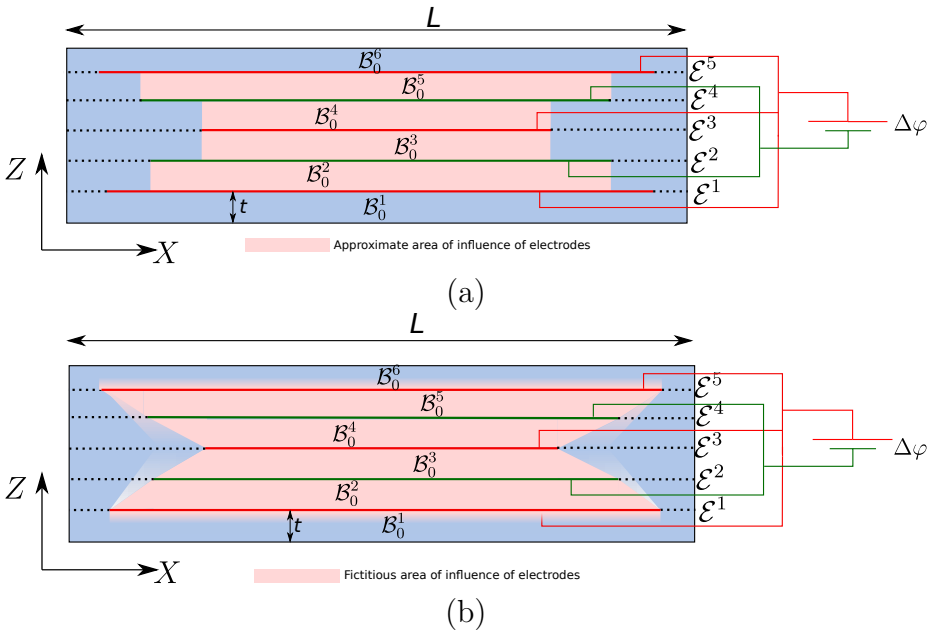

Figure 6: (a) Approximate region of influence of electrodes in the sharp interface approach. (b) Diffuse region of influence of electrodes in the diffuse interface approach. The region of influence corresponds with the regions across the elastomeric layers $\{\mathcal{B}_0^1, \ldots, \mathcal{B}_0^{N_L}\}$ where the electric field is mostly confined.

- Smooth in-surface representation of the electrodes within the interface $\mathcal{E}^i$ via an in-surface phase-field function $\psi_{\mathcal{E}^i}$, which will replace the sharpest characteristic function $\chi_{\mathcal{E}^i}$.
- Smooth (Laplacian) extension of the in-plane phase-field function $\psi_{\mathcal{E}^i}$ into the volume of the adjacent elastomeric layers, resulting into the phase field function $\psi_{\mathcal{B}_0}$, which will represent the so-called ***region of influence of electrodes***. This extension is essential to impose the design feature in point **V** at the beginning of Section 3, restricting the interaction of electrodes only to those placed between adjacent layers.
- Definition of a suitable (spatially varying) free energy density capable of recreating an electric displacement $\boldsymbol{D}_0$ rapidly decreasing to zero away from the ***region of influence of electrodes***.

Regarding the first ingredient above, the sharpest characteristic function $\chi_{\mathcal{E}^i}$ in (20) is replaced by a smooth phase field function $\psi_{\mathcal{E}^i} \in \mathbb{V}^{\psi_{\mathcal{E}^i}}$ on each surface region $\mathcal{E}^i$, such that

$$\mathbb{V}^{\psi_{\mathcal{E}^i}} = \left\{\psi_{\mathcal{E}^i} : \mathcal{E}^i \to [0,1]\,, \quad \psi_{\mathcal{E}^i} \in H^1(\mathcal{E}^i)\right\}; \qquad i = \{1, \ldots, N_{L-1}\}, \tag{24}$$

where $\boldsymbol{\xi} \in \mathcal{E}^i$ with a value of $\psi_{\mathcal{E}^i}(\boldsymbol{\xi}) = 1$ corresponds with the region $\mathcal{E}^i_{\text{Elec}} \in \mathcal{E}^i$ where the electrode is actuated. On the other hand, $\boldsymbol{\xi} \in \mathcal{E}^i$ with a value of $\psi_{\mathcal{E}^i}(\boldsymbol{\xi}) = 0$ corresponds with the region of

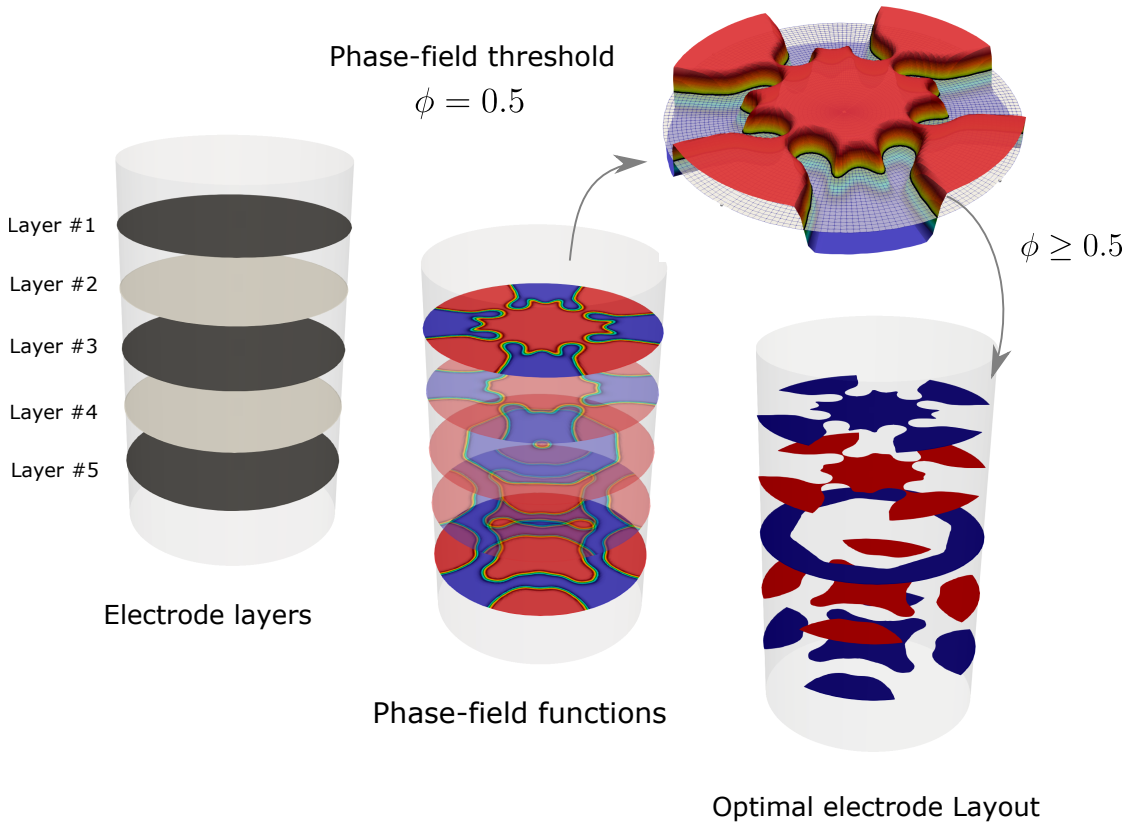

Figure 7: Layer-by-layer layout within the diffuse interface setting. **Left**: DE device comprising six elastomer layers $\{\mathcal{B}_0^1, \ldots, \mathcal{B}_0^6\}$ and five intercalated surface regions $\{\mathcal{E}^1, \ldots, \mathcal{E}^5\}$. **Centre**: final distribution of the functions $\psi_{\mathcal{E}^i}(\boldsymbol{\xi})$ with value $\psi_{\mathcal{E}^i}(\boldsymbol{\xi}) = 1$, representing the electrode regions $\{\mathcal{E}^1_{\text{Elec}}, \ldots, \mathcal{E}^5_{\text{Elec}}\}$. **Right**: representation of each of the five electrodes by selecting the threshold value of $\psi_{\mathcal{E}^i}(\boldsymbol{\xi}) \geq 0.5$ for all the electrode surfaces.

$\mathcal{E}^i$ where electrode collocation is avoided. Finally, $\boldsymbol{\xi} \in \mathcal{E}^i$ with intermediate values $0 < \psi_{\mathcal{E}^i}(\boldsymbol{\xi}) < 1$ represent the in-surface diffuse interface of the electrode $\partial\mathcal{E}^i_{\text{Elec}}$, that is

$$\forall \boldsymbol{\xi} \in \mathcal{E}^i, \begin{cases} \psi_{\mathcal{E}^i}(\boldsymbol{\xi}) = 1; & \text{if } \boldsymbol{\xi} \in \mathcal{E}^i_{\text{Elec}}; \\ 0 < \psi_{\mathcal{E}^i}(\boldsymbol{\xi}) < 1; & \text{if } \boldsymbol{\xi} \in \partial\mathcal{E}^i_{\text{Elec}}; \\ \psi_{\mathcal{E}^i}(\boldsymbol{\xi}) = 0; & \text{if } \boldsymbol{\xi} \in \mathcal{E}^i \setminus \left(\mathcal{E}^i_{\text{Elec}} \cup \partial\mathcal{E}^i_{\text{Elec}}\right). \end{cases} \tag{25}$$

Figure 7 perfectly showcases the difference of the diffuse interface approach with respect to the sharp approach, previously depicted in Figure 5. The same DE as in Figure 5-left, characterised by six elastomer layers $\{\mathcal{B}^1_0, \ldots, \mathcal{B}^6_0\}$ (hence with five interfaces $\{\mathcal{E}^1, \ldots, \mathcal{E}^5\}$), is considered. Figure 7-centre shows the three regions $\mathcal{E}^i_{\text{Elec}}$ (in red), $\partial\mathcal{E}^i_{\text{Elec}}$ (in yellow), and $\mathcal{E}^i \setminus (\mathcal{E}^i_{\text{Elec}} \cup \partial\mathcal{E}^i_{\text{Elec}})\}$ (in blue). Clearly, under this approach, the thickness of the interface region $\partial\mathcal{E}^i_{\text{Elec}}$ is not strictly zero, in contrast with the sharp interface approach described in Section 3.1. For convenience, all the in-surface phase field functions can be combined into a set $\boldsymbol{\psi}_{\mathcal{E}}$ defined as

$$\boldsymbol{\psi}_{\mathcal{E}} = \{\psi_{\mathcal{E}^1} \ldots \psi_{\mathcal{E}^{N_L-1}}\}. \tag{26}$$

Next, a smooth (Laplacian) extension of the in-surface phase functions $\psi_{\mathcal{E}^i}(\boldsymbol{\xi})$ into the volume $\mathcal{B}_0$ is formulated by means of a (volumetric) extension $\psi_{\mathcal{B}_0}(\boldsymbol{X})$ complying with the following essential boundary conditions

$$\psi_{\mathcal{B}_0} = \psi_{\mathcal{E}^i} \qquad \text{on } \mathcal{E}^i,\ i = \{1, \ldots, N_L - 1\}; \tag{27a}$$

$$\psi_{\mathcal{B}_0} = 1 \qquad \text{on } \partial_\varphi\mathcal{B}_0; \tag{27b}$$

$$\psi_{\mathcal{B}_0} = 0 \qquad \text{on } \partial_\omega\mathcal{B}_0. \tag{27c}$$

Thus, the function $\psi_{\mathcal{B}_0}$ can be derived from the following variational principle

$$\Lambda(\boldsymbol{\psi}_{\mathcal{E}}, \psi^*_{\mathcal{B}_0}) = \inf_{\psi_{\mathcal{B}_0}} \left\{ \int_{\mathcal{B}_0} \frac{1}{2} |\boldsymbol{\nabla}_0 \psi_{\mathcal{B}_0}|^2 \, dV \right\}, \tag{28}$$

where the field $\psi_{\mathcal{B}_0}$ is selected within a suitable functional space $\mathbb{V}^{\psi_{\mathcal{B}_0}}$ defined by

$$\mathbb{V}^{\psi_{\mathcal{B}_0}} = \left\{ \psi_{\mathcal{B}_0} : \mathcal{B}_0 \to [0, 1], \quad \psi_{\mathcal{B}_0} \in H^1(\mathcal{B}_0), \text{ s.t. } (27) \right\}. \tag{29}$$

As can be seen, $\psi_{\mathcal{B}_0}$ is a function of position $\boldsymbol{X}$ and the set of in-surface phase field functions $\boldsymbol{\psi}_{\mathcal{E}}$, that is $\psi_{\mathcal{B}_0}(\boldsymbol{X}, \boldsymbol{\psi}_{\mathcal{E}})$. The stationary conditions of $\Lambda(\boldsymbol{\psi}_{\mathcal{E}}, \psi_{\mathcal{B}_0})$ (28), stemming from its directional derivative with respect to independent virtual variations $\delta\psi_{\mathcal{B}_0} \in \mathbb{V}_0^{\psi_{\mathcal{B}_0}}$, yield the following variational statement

$$D\Lambda(\boldsymbol{\psi}_{\mathcal{E}}, \psi_{\mathcal{B}_0})[\delta\psi_{\mathcal{B}_0}] = \int_{\mathcal{B}_0} \boldsymbol{\nabla}_0 \psi_{\mathcal{B}_0} \cdot \boldsymbol{\nabla}_0 \delta\psi_{\mathcal{B}_0} \, dV = 0. \tag{30}$$

Solution of above variational statement (30) leads to the definition of the extended function $\psi_{\mathcal{B}_0}(\boldsymbol{X}, \boldsymbol{\psi}_{\mathcal{E}})$, representing the diffuse ***region of influence of electrodes***, depicted in Figure 6$_b$.

It remains to introduce the final ingredient, namely, a suitable (spatially varying) free energy density, capable of recreating an electric displacement $\boldsymbol{D}_0$ rapidly decreasing to zero away from the ***region of influence of electrodes***. This can be accomplished through the following free energy density definition

$$\Psi(\psi_{\mathcal{B}_0}(\boldsymbol{X}, \boldsymbol{\psi}_{\mathcal{E}}), \boldsymbol{F}, \boldsymbol{E}_0) = \Psi_m(\boldsymbol{F}) + \bar{\Psi}_{em}(\psi_{\mathcal{B}_0}(\boldsymbol{X}, \boldsymbol{\psi}_{\mathcal{E}}), \boldsymbol{F}, \boldsymbol{E}_0), \tag{31}$$

where $\Psi_m(\boldsymbol{F})$ represents the mechanical contribution to the free energy density (refer to (7)) and $\bar{\Psi}_{em}(\psi_{\mathcal{B}_0}(\boldsymbol{X}, \boldsymbol{\psi}_{\mathcal{E}}), \boldsymbol{F}, \boldsymbol{E}_0)$ represents a spatially varying electromechanical energy contribution

which remains to be defined. In this work, we propose $\bar{\Psi}_{em}(\psi_{\mathcal{B}_0}(\boldsymbol{X},\boldsymbol{\psi}_{\mathcal{E}}),\boldsymbol{F},\boldsymbol{E}_0)$ to be defined as a convex interpolation between the electromechanical energy of the DE (when $\psi_{\mathcal{B}_0}\to 1$) and an extremely small electromechanical energy contribution (when $\psi_{\mathcal{B}_0}\to 0$). Specifically,

$$\bar{\Psi}_{em}(\psi_{\mathcal{B}_0}(\boldsymbol{X},\boldsymbol{\psi}_{\mathcal{E}}),\boldsymbol{F},\boldsymbol{E}_0)\big|_{\psi_{\mathcal{B}_0}=1} = \Psi_{em}(\boldsymbol{F},\boldsymbol{E}_0); \tag{32a}$$

$$\bar{\Psi}_{em}(\psi_{\mathcal{B}_0}(\boldsymbol{X},\boldsymbol{\psi}_{\mathcal{E}}),\boldsymbol{F},\boldsymbol{E}_0)\big|_{\psi_{\mathcal{B}_0}=0} = \alpha\Psi_{em}(\boldsymbol{F},\boldsymbol{E}_0), \tag{32b}$$

where α is a dimensionless parameter of the order of $\alpha\approx 10^{-8}$ and $\Psi_{em}(\boldsymbol{F},\boldsymbol{E}_0)$ is defined as in (8). A suitable representation of $\bar{\Psi}_{em}$ complying with the above two conditions in (32), typically considered in the context of SIMP-based topology optimisation [42], is as follows

$$\bar{\Psi}_{em}(\psi_{\mathcal{B}_0}(\boldsymbol{X},\boldsymbol{\psi}_{\mathcal{E}}),\boldsymbol{F},\boldsymbol{E}_0) = (\psi_{\mathcal{B}_0}(\boldsymbol{X},\boldsymbol{\psi}_{\mathcal{E}}))^p\,\Psi_{em}(\boldsymbol{F},\boldsymbol{E}_0) + (1-(\psi_{\mathcal{B}_0}(\boldsymbol{X},\boldsymbol{\psi}_{\mathcal{E}}))^p)\,\alpha\Psi_{em}(\boldsymbol{F},\boldsymbol{E}_0). \tag{33}$$

The dimensionless exponent p is traditionally given the value $p=3$ in the context of SIMP-based topology optimisation for linear elasticity, in order to fulfil the so-called Hashin–Strikman bounds [42]. To the best of the authors' knowledge, analogous physical bounds for the case nonlinear electromechanics are not known and hence, we will use $p=3$ in what follows. Above representation (33) can be further manipulated to yield

$$\begin{aligned}\bar{\Psi}_{em}(\psi_{\mathcal{B}_0}(\boldsymbol{X},\boldsymbol{\psi}_{\mathcal{E}}),\boldsymbol{F},\boldsymbol{E}_0) &= \left[(\psi_{\mathcal{B}_0}(\boldsymbol{X},\boldsymbol{\psi}_{\mathcal{E}}))^p + \alpha\,(1-(\psi_{\mathcal{B}_0}(\boldsymbol{X},\boldsymbol{\psi}_{\mathcal{E}}))^p)\right]\Psi_{em}(\boldsymbol{F},\boldsymbol{E}_0)\\ &\approx \underbrace{\left[(\psi_{\mathcal{B}_0}(\boldsymbol{X},\boldsymbol{\psi}_{\mathcal{E}}))^p + \alpha\right]}_{f(\psi_{\mathcal{B}_0}(\boldsymbol{X},\boldsymbol{\psi}_{\mathcal{E}}))}\Psi_{em}(\boldsymbol{F},\boldsymbol{E}_0),\end{aligned} \tag{34}$$

where $f(\psi_{\mathcal{B}_0}(\boldsymbol{X},\boldsymbol{\psi}_{\mathcal{E}}))$ represents an interpolation function in the range $[\alpha,1]$ written in terms of the volume extended phase field function $\psi_{\mathcal{B}_0}(\boldsymbol{X},\boldsymbol{\psi}_{\mathcal{E}})$.

Remark 1. Notice that the definition of the interpolated electromechanical contribution $\bar{\Psi}_{em}$ in (34) is not the only possible one. An alternative expression for $\bar{\Psi}_{em}$ can be

$$\bar{\Psi}_{em}(\psi_{\mathcal{B}_0}(\boldsymbol{X},\boldsymbol{\psi}_{\mathcal{E}}),\boldsymbol{F},\boldsymbol{E}_0) = \Psi_{em}(\boldsymbol{F},\bar{\boldsymbol{E}}_0(\psi_{\mathcal{B}_0}(\boldsymbol{X},\boldsymbol{\psi}_{\mathcal{E}}),\boldsymbol{E}_0)), \tag{35}$$

with

$$\bar{\boldsymbol{E}}_0(\psi_{\mathcal{B}_0}(\boldsymbol{X},\boldsymbol{\psi}_{\mathcal{E}}),\boldsymbol{E}_0) = (\psi_{\mathcal{B}_0}(\boldsymbol{X},\boldsymbol{\psi}_{\mathcal{E}}))^p\,\boldsymbol{E}_0 + (1-(\psi_{\mathcal{B}_0}(\boldsymbol{X},\boldsymbol{\psi}_{\mathcal{E}}))^p)\,\alpha\boldsymbol{E}_0, \tag{36}$$

where instead of interpolating the electromechanical energy of the DE Ψ_{em} as in (34), the interpolation is applied on the electric field $\boldsymbol{E}_0$.

Associated with the spatially varying interpolated free energy density $\Psi(\psi_{\mathcal{B}_0}(\boldsymbol{X},\boldsymbol{\psi}_{\mathcal{E}}),\boldsymbol{F},\boldsymbol{E}_0)$ (refer to equations (31) and (34)), it is now possible to obtain the spatially varying first Piola-Kirchoff stress tensor $\boldsymbol{P}$ and electric displacement field $\boldsymbol{D}_0$, by making use of equations in (4), yielding

$$\boldsymbol{P}(\psi_{\mathcal{B}_0}(\boldsymbol{X},\boldsymbol{\psi}_{\mathcal{E}}),\boldsymbol{F},\boldsymbol{E}_0) = \partial_{\boldsymbol{F}}\Psi_m^{\text{solid}}(\boldsymbol{F}) + f(\psi_{\mathcal{B}_0}(\boldsymbol{X},\boldsymbol{\psi}_{\mathcal{E}}))\partial_{\boldsymbol{F}}\Psi_{em}(\boldsymbol{F},\boldsymbol{E}_0); \tag{37a}$$

$$\boldsymbol{D}_0(\psi_{\mathcal{B}_0}(\boldsymbol{X},\boldsymbol{\psi}_{\mathcal{E}}),\boldsymbol{F},\boldsymbol{E}_0) = -f(\psi_{\mathcal{B}_0}(\boldsymbol{X},\boldsymbol{\psi}_{\mathcal{E}}))\partial_{\boldsymbol{E}_0}\Psi_{em}(\boldsymbol{F},\boldsymbol{E}_0). \tag{37b}$$

Similarly, the spatially varying fourth order elasticity tensor $\boldsymbol{\mathcal{C}}$, third order piezoelectric tensor $\boldsymbol{\mathcal{P}}$ and second order dielectric tensor $\boldsymbol{\varepsilon}$ associated with $\Psi(\psi_{\mathcal{B}_0}(\boldsymbol{X},\boldsymbol{\psi}_{\mathcal{E}}),\boldsymbol{F},\boldsymbol{E}_0)$ (refer to equations (31) and (34)) can be computed by making use of equations in (5), resulting in

$$\boldsymbol{\mathcal{C}}(\psi_{\mathcal{B}_0}(\boldsymbol{X},\boldsymbol{\psi}_{\mathcal{E}}),\boldsymbol{F},\boldsymbol{E}_0) = \partial^2_{\boldsymbol{F}\boldsymbol{F}}\Psi_m(\boldsymbol{F}) + f(\psi_{\mathcal{B}_0}(\boldsymbol{X},\boldsymbol{\psi}_{\mathcal{E}}))\partial^2_{\boldsymbol{F}\boldsymbol{F}}\Psi_{em}(\boldsymbol{F},\boldsymbol{E}_0); \tag{38a}$$

$$\boldsymbol{\mathcal{P}}(\psi_{\mathcal{B}_0}(\boldsymbol{X},\boldsymbol{\psi}_{\mathcal{E}}),\boldsymbol{F},\boldsymbol{E}_0) = -f(\psi_{\mathcal{B}_0}(\boldsymbol{X},\boldsymbol{\psi}_{\mathcal{E}}))\partial^2_{\boldsymbol{E}_0\boldsymbol{F}}\Psi_{em}(\boldsymbol{F},\boldsymbol{E}_0); \tag{38b}$$

$$\boldsymbol{\varepsilon}(\psi_{\mathcal{B}_0}(\boldsymbol{X},\boldsymbol{\psi}_{\mathcal{E}}),\boldsymbol{F},\boldsymbol{E}_0) = -f(\psi_{\mathcal{B}_0}(\boldsymbol{X},\boldsymbol{\psi}_{\mathcal{E}}))\partial^2_{\boldsymbol{E}_0\boldsymbol{E}_0}\Psi_{em}(\boldsymbol{F},\boldsymbol{E}_0). \tag{38c}$$

Remark 2. For the case where $\psi_{\mathcal{B}_0} = 0$, the interpolation scheme in (33) renders a material with effective relative permittivity $\bar{\varepsilon}_r$ which does not correspond with any real material (see equation (32b)), namely

$$\bar{\Psi}_{em}(\psi_{\mathcal{B}_0}(\boldsymbol{X}, \boldsymbol{\psi}_{\mathcal{E}}), \boldsymbol{F}, \boldsymbol{E}_0)\big|_{\psi_{\mathcal{B}_0}=0} = \alpha \Psi_{em}(\boldsymbol{F}, \boldsymbol{E}_0) = -\frac{\bar{\varepsilon}_r \varepsilon_0}{2J} II_{\boldsymbol{H}\boldsymbol{E}_0}; \qquad \bar{\varepsilon}_r = \alpha \varepsilon_r << 1. \tag{39}$$

However, the objective of such interpolation is to introduce a *dummy* electric potential in areas where $\psi_{\mathcal{B}_0} \approx 0$ so that the contribution on the stress tensor $\boldsymbol{P}$ in (37a) is negligible. Associated with $\bar{\Psi}_{em}$ in (33) it is possible to obtain its contribution within the first Piola-Kirchhoff stress tensor $\boldsymbol{P}_{em}$ as

$$\boldsymbol{P}_{em} := \partial_{\boldsymbol{F}} \bar{\Psi}_{em} = \psi^p_{\mathcal{B}_0} \partial_{\boldsymbol{F}} \Psi_{em}(\boldsymbol{F}, \boldsymbol{E}_0) + \alpha(1 - \psi^p_{\mathcal{B}_0}) \partial_{\boldsymbol{F}} \Psi_{em}(\boldsymbol{F}, \boldsymbol{E}_0) \tag{40}$$

Clearly, for $\psi_{\mathcal{B}_0} = 0$ above equation yields

$$\boldsymbol{P}_{em} = \alpha \partial_{\boldsymbol{F}} \Psi_{em}(\boldsymbol{F}, \boldsymbol{E}_0). \tag{41}$$

Essentially, even though the distribution of electric potential, and hence, of electric field does not correspond with that of a real material in those areas where $\psi_{\mathcal{B}_0} \approx 0$, the underlying objective, which is to obtain an almost vanishing contribution on the stress tensor, is achieved, as it is shown in equation (41). Of course, this is not the only way to achieve such an objective. An alternative energy interpolation would be

$$\bar{\Psi}_{em}(\psi_{\mathcal{B}_0}(\boldsymbol{X}, \boldsymbol{\psi}_{\mathcal{E}}), \boldsymbol{F}, \boldsymbol{E}_0) = (\psi_{\mathcal{B}_0}(\boldsymbol{X}, \boldsymbol{\psi}_{\mathcal{E}}))^p \, \Psi_{em}(\boldsymbol{F}, \boldsymbol{E}_0) + (1 - (\psi_{\mathcal{B}_0}(\boldsymbol{X}, \boldsymbol{\psi}_{\mathcal{E}}))^p) \, \Psi_0(\boldsymbol{E}_0),$$

where $\Psi_0(\boldsymbol{E}_0)$ is similar to the electromechanical energy of the vacuum for the specific case where $\boldsymbol{F} = \boldsymbol{I}$, namely

$$\Psi_0(\boldsymbol{E}_0) = -\frac{\varepsilon_0}{2} \boldsymbol{E}_0 \cdot \boldsymbol{E}_0,$$

and therefore, for the case where $\psi_{\mathcal{B}_0} \approx 0$, no electromechanical contribution is included in the stress, namely $\partial_{\boldsymbol{F}} \bar{\Psi}_{em}\big|_{\psi_{\mathcal{B}_0}=0} = \boldsymbol{0}$. It is important to emphasise though that the focus of this paper is on actuation, and not energy harvesting, which would require an accurate resolution of the electric potential field, rather than the accurate capture of the deformation.

Having presented the three ingredients of the diffuse interface approach, that is the in-surface phase field function $\psi_{\mathcal{E}^i}$, the Laplacian extension $\psi_{\mathcal{B}_0}$ and the spatially varying energy functional, the actuation response of the DE can be described by the boundary value problem described previously through equations (22) and (23), but where the first Piola-Kirchhoff stress tensor $\boldsymbol{P}$ and the electric displacement $\boldsymbol{D}_0$ featuring therein are now computed based on the spatially varying free energy density (refer to equations (31) and (34)) and where equation (23e) is replaced by the simpler equation

$$\varphi = \pm \bar{\varphi}; \quad \text{on } \boldsymbol{X} \in \mathcal{E}^i \subset \mathcal{E}^{\pm}. \tag{42}$$

Notice that the difference in electromechanical response of the DE as a result of the replacement of (23e) with (42) is strictly localised to the interface regions defined by $\mathcal{E}^i \setminus \mathcal{E}^i_{Elec}$. From the actuation design standpoint, this difference is negligible due to the counterbalancing effect introduced by the in-surface phase function $\psi_{\mathcal{E}^i}$, which takes null values in $\mathcal{E}^i \setminus \mathcal{E}^i_{Elec}$. This permits to circumvent the time consuming task posed by the challenging application of the sharp interface approach, namely equation (23e).

For the sake of simplicity, we restrict ourselves to the use of spatial discretisations which are C^0 conforming in the fields $\{\boldsymbol{\phi}, \varphi\}$ across interfaces, as this permits the trivial satisfaction of equations (22e), (22f), (23f) and (23g), resulting in the following electro-mechanical boundary value problem

$$\boldsymbol{F} = \boldsymbol{\nabla}_0 \boldsymbol{\phi}; \qquad \text{in } \mathcal{B}_0; \tag{43a}$$

$$\mathrm{DIV}\boldsymbol{P}(\psi_{\mathcal{B}_0}(\boldsymbol{X}, \boldsymbol{\psi}_{\mathcal{E}}), \boldsymbol{F}, \boldsymbol{E}_0) + \boldsymbol{f}_0 = \boldsymbol{0}; \qquad \text{in } \mathcal{B}_0; \tag{43b}$$

$$\boldsymbol{P}\boldsymbol{N} = \boldsymbol{t}_0; \qquad \text{on } \partial_{\boldsymbol{t}}\mathcal{B}_0; \tag{43c}$$

$$\boldsymbol{\phi} = \bar{\boldsymbol{\phi}}^b; \qquad \text{on } \partial_{\boldsymbol{\phi}}\mathcal{B}_0, \tag{43d}$$

and

$$\boldsymbol{E}_0 = -\boldsymbol{\nabla}_0 \varphi; \qquad \text{in } \mathcal{B}_0; \tag{44a}$$

$$\mathrm{DIV}\boldsymbol{D}_0(\psi_{\mathcal{B}_0}(\boldsymbol{X}, \boldsymbol{\psi}_{\mathcal{E}}), \boldsymbol{F}, \boldsymbol{E}_0) = \rho_0; \qquad \text{in } \mathcal{B}_0; \tag{44b}$$

$$\boldsymbol{D}_0 \cdot \boldsymbol{N} = -\omega_0; \qquad \text{on } \partial_{\omega}\mathcal{B}_0; \tag{44c}$$

$$\varphi = \bar{\varphi}^b; \qquad \text{on } \partial_{\varphi}\mathcal{B}_0; \tag{44d}$$

$$\varphi = \pm\bar{\varphi}; \qquad \text{on } \mathcal{E}^{\pm}, \tag{44e}$$

where $\psi_{\mathcal{B}_0}(\boldsymbol{X}, \boldsymbol{\psi}_{\mathcal{E}})$ is obtained from the Laplacian extension (30) and where the first Piola-Kirchhoff stress tensor $\boldsymbol{P}$ and the electric displacement $\boldsymbol{D}_0$ are derived from the spatially varying free energy density (refer to equations (31) and (34)). All in all, equations (30), (31), (34), (43), (44) define the governing equations of the *diffuse* electro-mechanical DE response. Solution of the electro-mechanical boundary value problem defined above (refer to equations (43) and (44)) by using a variational formulation requires a straightforward modification of the variational principle (11). Specifically, the modified variational principle can be formulated as

$$\Pi(\psi_{\mathcal{B}_0}(\boldsymbol{\psi}_{\mathcal{E}}), \boldsymbol{\phi}^*, \varphi^*) = \inf_{\boldsymbol{\phi}} \sup_{\varphi} \left\{ \int_{\mathcal{B}_0} \Psi\left(\psi_{\mathcal{B}_0}(\boldsymbol{X}, \boldsymbol{\psi}_{\mathcal{E}}), \boldsymbol{F}, \boldsymbol{E}_0\right) dV - \Pi^m_{\text{ext}}\left(\boldsymbol{\phi}\right) - \Pi^{em}_{\text{ext}}\left(\varphi\right) \right\}, \tag{45}$$

where the unknown fields $\{\boldsymbol{\phi}, \varphi\}$ are chosen within suitable functional spaces satisfying this time the additional essential condition (44e), that is

$$\mathbb{V}^{\boldsymbol{\phi}} = \{\boldsymbol{\phi} \in (H^1(\mathcal{B}_0))^3 : \text{ s.t. } (43\text{d})\}; \qquad \mathbb{V}^{\varphi} = \{\varphi \in H^1(\mathcal{B}_0) : \text{ s.t. } (44\text{d}), (44\text{e})\}. \tag{46}$$

Remark 3. The free energy density (31) featuring in above variational principle (45) can be additively re-written as

$$\Psi\left(\psi_{\mathcal{B}_0}(\boldsymbol{X}, \boldsymbol{\psi}_{\mathcal{E}}), \boldsymbol{F}, \boldsymbol{E}_0\right) = \Psi\left(\boldsymbol{F}, \boldsymbol{E}_0\right) - (1 - f(\psi_{\mathcal{B}_0}(\boldsymbol{X}, \boldsymbol{\psi}_{\mathcal{E}})))\Psi_{em}(\boldsymbol{F}, \boldsymbol{E}_0), \tag{47}$$

in terms of a first homogeneous contribution and a second spatially varying contribution. The second (negative) term is prevalent in those regions of $\mathcal{B}_0$ in the vicinity of $\mathcal{E}^i \setminus (\mathcal{E}^i_{\text{Elec}} \cup \partial\mathcal{E}^i_{\text{Elec}})$ and served to smoothly counterbalance the effect of applying condition (42), instead of the sharpest condition (23e). Thus, referring to the variational principle (45), it yields

$$\lim_{\psi_{\mathcal{B}_0} \to \psi_{\mathcal{E}^i}} \left\{ \int_{\mathcal{B}_0} -(1 - f(\psi_{\mathcal{B}_0}(\boldsymbol{X}, \boldsymbol{\psi}_{\mathcal{E}})))\Psi_{em}(\boldsymbol{F}, \boldsymbol{E}_0) dV \right\} \approx \int_{\mathcal{E}^i_{\text{Elec}}} -\frac{\alpha}{2}(\varphi \pm \bar{\varphi})^2 dA; \qquad \alpha > 0, \tag{48}$$

so that the negative spatially varying term in (47) degenerates to a penalty type removal of the potential on the in-surface non-electrode regions.

As can be observed in (45), the functional Π depends implicitly on the set of in-surface phase field functions $\boldsymbol{\psi}_{\mathcal{E}}$ through the Laplacian extension $\psi_{\mathcal{B}_0}$. The stationary conditions of $\Pi(\psi_{\mathcal{B}_0}(\boldsymbol{\psi}_{\mathcal{E}}), \boldsymbol{\phi}, \varphi)$ (45) stemming from its directional derivatives with respect to independent virtual variations $\delta\boldsymbol{\phi} \in \mathbb{V}_0^{\boldsymbol{\phi}}$ and $\delta\varphi \in \mathbb{V}_0^{\varphi}$, yield the variational forms of the conservation of linear momentum and Gauss's law, namely

$$D\Pi(\psi_{\mathcal{B}_0}(\boldsymbol{\psi}_{\mathcal{E}}), \boldsymbol{\phi}, \varphi)[\delta\boldsymbol{\phi}] = \int_{\mathcal{B}_0} \boldsymbol{P}(\psi_{\mathcal{B}_0}(\boldsymbol{X}, \boldsymbol{\psi}_{\mathcal{E}}), \boldsymbol{F}, \boldsymbol{E}_0) : \boldsymbol{\nabla}_0 \delta\boldsymbol{\phi}\, dV - D\Pi^{m}_{\text{ext}}(\boldsymbol{\phi})[\delta\boldsymbol{\phi}] = 0; \tag{49a}$$

$$D\Pi(\psi_{\mathcal{B}_0}(\boldsymbol{\psi}_{\mathcal{E}}), \boldsymbol{\phi}, \varphi)[\delta\varphi] = \int_{\mathcal{B}_0} \boldsymbol{D}_0(\psi_{\mathcal{B}_0}(\boldsymbol{X}, \boldsymbol{\psi}_{\mathcal{E}}), \boldsymbol{F}, \boldsymbol{E}_0) \cdot \boldsymbol{\nabla}_0 \delta\varphi\, dV - D\Pi^{em}_{\text{ext}}(\varphi)[\delta\varphi] = 0. \tag{49b}$$

The above variational statements (49) along with (30) represent three of the optimality conditions of the meso-architecture design optimisation process to be described in the following section. Naturally, for different definitions of the in-surface phase field functions $\psi_{\mathcal{E}^i}$, $(i = 1 \dots N_L - 1)$, different electro-mechanical DE responses can be anticipated. As such, *reconfigurable* DE designs can be rapidly generated by simply modifying the definition of the in-surface phase field functions $\psi_{\mathcal{E}^i}$, resulting into different actuation modes. Interestingly, an additional positive by-product of the above diffuse formulation, in contrast to the sharp interface approach, is that of the computational efficiency, enabling the fast testing of multiple meso-architectures in the search of user-defined tailor-made actuation modes. Finally, in order to solve the coupled system of nonlinear variational forms in (49), we can use a Newton-Raphson k-iterative scheme where both variational forms are linearised with respect to incremental fields $\Delta\boldsymbol{\phi} \in \mathbb{V}_0^{\boldsymbol{\phi}}$ and $\Delta\varphi \in \mathbb{V}_0^{\varphi}$ as

$$D^2\Pi(\psi_{\mathcal{B}_0}(\boldsymbol{\psi}_{\mathcal{E}}), \boldsymbol{\phi}^k, \varphi^k)[\delta\boldsymbol{\phi}; \Delta\boldsymbol{\phi}] + D^2\Pi(\psi_{\mathcal{B}_0}(\boldsymbol{\psi}_{\mathcal{E}}), \boldsymbol{\phi}^k, \varphi^k)[\delta\boldsymbol{\phi}; \Delta\varphi] = -D\Pi(\psi_{\mathcal{B}_0}(\boldsymbol{\psi}_{\mathcal{E}}), \boldsymbol{\phi}^k, \varphi^k)[\delta\boldsymbol{\phi}]; \tag{50a}$$

$$D^2\Pi(\psi_{\mathcal{B}_0}(\boldsymbol{\psi}_{\mathcal{E}}), \boldsymbol{\phi}^k, \varphi^k)[\delta\varphi; \Delta\boldsymbol{\phi}] + D^2\Pi(\psi_{\mathcal{B}_0}(\boldsymbol{\psi}_{\mathcal{E}}), \boldsymbol{\phi}^k, \varphi^k)[\delta\varphi; \Delta\varphi] = -D\Pi(\psi_{\mathcal{B}_0}(\boldsymbol{\psi}_{\mathcal{E}}), \boldsymbol{\phi}^k, \varphi^k)[\delta\varphi], \tag{50b}$$

which permit the update of the solution fields $\boldsymbol{\phi}$ and φ at Newton-Raphson iteration k as presented in (16) and where the second directional derivative terms are analogous to those shown in (17), except for the use of the potential $\Pi_{\psi_{\mathcal{B}_0}}$, that is

$$\begin{aligned}
D^2\Pi(\psi_{\mathcal{B}_0}(\boldsymbol{\psi}_{\mathcal{E}}), \boldsymbol{\phi}, \varphi)[\delta\boldsymbol{\phi}; \Delta\boldsymbol{\phi}] &= \int_{\mathcal{B}_0} \boldsymbol{\nabla}_0 \delta\boldsymbol{\phi} : \boldsymbol{\mathcal{C}}(\psi_{\mathcal{B}_0}(\boldsymbol{X}, \boldsymbol{\psi}_{\mathcal{E}}), \boldsymbol{F}, \boldsymbol{E}_0) : \boldsymbol{\nabla}_0 \Delta\boldsymbol{\phi}\, dV; \\
D^2\Pi(\psi_{\mathcal{B}_0}(\boldsymbol{\psi}_{\mathcal{E}}), \boldsymbol{\phi}, \varphi)[\delta\boldsymbol{\phi}; \Delta\varphi] &= \int_{\mathcal{B}_0} \boldsymbol{\nabla}_0 \delta\boldsymbol{\phi} : \boldsymbol{\mathcal{P}}^T(\psi_{\mathcal{B}_0}(\boldsymbol{X}, \boldsymbol{\psi}_{\mathcal{E}}), \boldsymbol{F}, \boldsymbol{E}_0) \cdot \boldsymbol{\nabla}_0 \Delta\varphi\, dV; \\
D^2\Pi(\psi_{\mathcal{B}_0}(\boldsymbol{\psi}_{\mathcal{E}}), \boldsymbol{\phi}, \varphi)[\delta\varphi; \Delta\boldsymbol{\phi}] &= \int_{\mathcal{B}_0} \boldsymbol{\nabla}_0 \delta\varphi \cdot \boldsymbol{\mathcal{P}}(\psi_{\mathcal{B}_0}(\boldsymbol{X}, \boldsymbol{\psi}_{\mathcal{E}}), \boldsymbol{F}, \boldsymbol{E}_0) : \boldsymbol{\nabla}_0 \Delta\boldsymbol{\phi}\, dV; \\
D^2\Pi(\psi_{\mathcal{B}_0}(\boldsymbol{\psi}_{\mathcal{E}}), \boldsymbol{\phi}, \varphi)[\delta\varphi; \Delta\varphi] &= -\int_{\mathcal{B}_0} \boldsymbol{\nabla}_0 \delta\varphi \cdot \boldsymbol{\varepsilon}(\psi_{\mathcal{B}_0}(\boldsymbol{X}, \boldsymbol{\psi}_{\mathcal{E}}), \boldsymbol{F}, \boldsymbol{E}_0) \boldsymbol{\nabla}_0 \Delta\varphi\, dV,
\end{aligned} \tag{51}$$

with the spatially varying constitutive tensors $\boldsymbol{\mathcal{C}}(\psi_{\mathcal{B}_0}(\boldsymbol{X}, \boldsymbol{\psi}_{\mathcal{E}}), \boldsymbol{F}, \boldsymbol{E}_0)$, $\boldsymbol{\mathcal{P}}(\psi_{\mathcal{B}_0}(\boldsymbol{X}, \boldsymbol{\psi}_{\mathcal{E}}), \boldsymbol{F}, \boldsymbol{E}_0)$ and $\boldsymbol{\varepsilon}(\psi_{\mathcal{B}_0}(\boldsymbol{X}, \boldsymbol{\psi}_{\mathcal{E}}), \boldsymbol{F}, \boldsymbol{E}_0)$ defined in (38).

4. Layer-by-layer electrode phase-field optimisation

The thin elastomeric layer-by-layer configuration described in the previous section has been conceived by researchers [21] with the aim of attaining a morphology that standard or conventional electrode layouts cannot achieve. The primary aim of this specific layout is not that of perfectly fitting the electrically deformed DE to a given target shape, but rather ensure that its deformed

configuration is endowed with certain desired morphological features, typically defined by specific changes in curvature. The latter can be investigated by focusing on the displacement field $\boldsymbol{u}(\boldsymbol{X}) = \boldsymbol{\phi}(\boldsymbol{X}) - \boldsymbol{X}$ of certain critical points which can ultimately induce the desired morphological pattern.

For instance, let us focus on the DE circular example depicted in Figure 8, constructed via the layer-by-layer layout shown in Figure 3, that is, comprised of four elastomeric layers and three internal electrode interfaces. Let us suppose that we are in search of the optimal electrode distribution on each interface $\{\mathcal{E}^1, \mathcal{E}^2, \mathcal{E}^3\}$ that permits the actuated DE to morph into Figure 8. Specifically, we aim at a final configuration characterised by a vertical displacement $u_Z = \boldsymbol{u} \cdot \boldsymbol{E}_3$ with $\boldsymbol{E}_3 = [0\,0\,1]^T$ on the perimeter of the DE which adopts the following parametrisation in terms of the angle θ (in cylindrical coordinates), i.e., $u_Z = U \sin(4\theta + \pi/2)$, where U is the maximum amplitude whose value is to be maximised. A plausible manner of inducing this desired morphology is by maximising and minimising the vertical displacement of points $\{A, B, C, D\}$ and $\{E, F, G, H\}$, respectively. This design optimisation process will be formalised next.

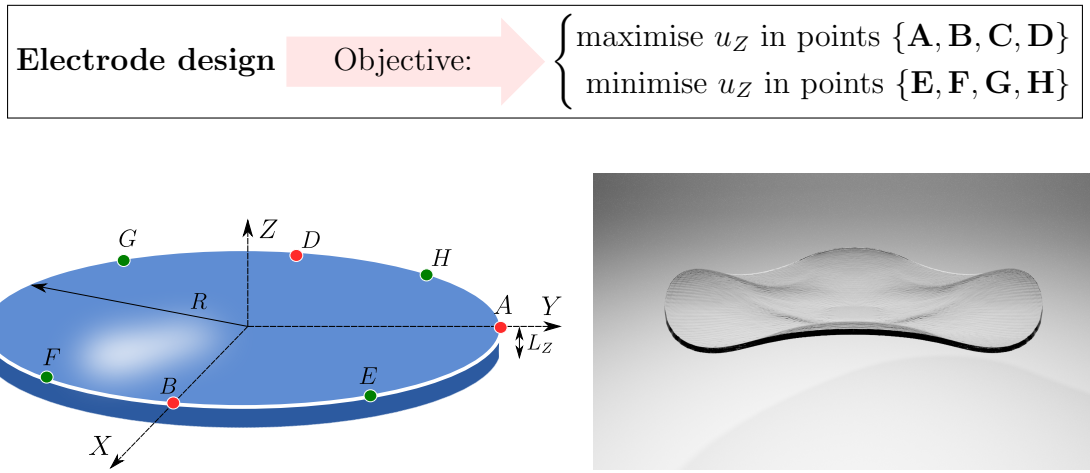

Figure 8: Illustration of the aim of the Topology-Optimisation aided electrode design: the Z displacement of the red and green target points must be maximised along the positive and negative Z direction, respectively.

4.1. The design optimisation problem and the objective function

The above (optimisation) design problem can be formulated in terms of an *objective function*, denoted as $\mathcal{J}(\boldsymbol{\phi})$, whose minimisation is sought. For the problem at hand, this objective function can be defined as

$$\begin{aligned}\mathcal{J}(\boldsymbol{\phi}) = &- ((\boldsymbol{\phi}(\boldsymbol{X}_A) - \boldsymbol{X}_A) + (\boldsymbol{\phi}(\boldsymbol{X}_B) - \boldsymbol{X}_B) + (\boldsymbol{\phi}(\boldsymbol{X}_C) - \boldsymbol{X}_C) + (\boldsymbol{\phi}(\boldsymbol{X}_D) - \boldsymbol{X}_D)) \cdot \boldsymbol{E}_3 \\ &+ ((\boldsymbol{\phi}(\boldsymbol{X}_E) - \boldsymbol{X}_E) + (\boldsymbol{\phi}(\boldsymbol{X}_F) - \boldsymbol{X}_F) + (\boldsymbol{\phi}(\boldsymbol{X}_G) - \boldsymbol{X}_G) + (\boldsymbol{\phi}(\boldsymbol{X}_H) - \boldsymbol{X}_H)) \cdot \boldsymbol{E}_3.\end{aligned} \tag{52}$$

Naturally, different morphing requirements will lead to alternative definitions of the above objective function. In the context of the layer by layer fabrication process, and in so far as the minimisation of the objective function $\mathcal{J}(\boldsymbol{\phi})$ is only driven by the selection of the in-surface phase field functions $\psi_{\mathcal{E}^i}$, $(i = 1 \dots N_L - 1)$, this results in the latter to be considered as the *design variables* of the optimisation problem, with their values restricted to be within the interval $[0, 1]$ (*lower/upper bounds*).

Due to the coupled (electro-mechanical) nature of the response of the DE, the mapping function $\boldsymbol{\phi}$ is intrinsically related to the electric potential φ distribution, and both physical fields $\{\boldsymbol{\phi}, \varphi\}$ must comply with the variational statements (49), embodying the *physical* governing

equations of the problem. As a result, the design optimisation problem can be summarised as

$$(P)\begin{cases}\min\limits_{\psi_{\mathcal{E}^i}(\boldsymbol{X})} \mathcal{J}(\boldsymbol{\phi})\ (52);\\ \text{s.t}\begin{cases}\text{Variational statements (49a) and (49b);}\\ \text{Constitutive model (31) and (34);}\\ \text{Laplacian extension (30);}\\ 0\leq\psi_{\mathcal{E}^i}(\boldsymbol{X})\leq 1;\quad \psi_{\mathcal{E}^i}(\boldsymbol{X})\in H^1(\mathcal{E}^i);\quad i=\{1,\dots,N_L-1\};.\end{cases}\end{cases} \tag{53}$$

The solution of the above optimisation problem (P) can be pursued via the introduction of a suitable Lagrangian functional whose *sensitivity* can be used to drive the optimisation process. The definition of this Lagrangian and the computation of its sensitivity is presented in the following section.

4.2. The optimisation Lagrangian $\mathcal{L}$ and its optimality conditions

In this work we advocate for a gradient-based approach for the solution of the optimisation problem (P) in (53). As it is customary, this requires the definition of a Lagrangian functional $\mathcal{L}$ with the aim of obtaining its sensitivity with respect to the set of design variables $\psi_{\mathcal{E}^i}$, $(i = 1\dots N_L-1)$. For problem (P) in (53), the Lagrangian functional $\mathcal{L}$ can be defined as

$$\mathcal{L}(\psi_{\mathcal{B}_0}(\boldsymbol{\psi}_{\mathcal{E}}),\boldsymbol{\phi},\varphi,\boldsymbol{p}_{\boldsymbol{\phi}},p_{\varphi}) = \mathcal{J}(\boldsymbol{\phi}) - \mathcal{W}^{\text{mec}}(\psi_{\mathcal{B}_0}(\boldsymbol{\psi}_{\mathcal{E}}),\boldsymbol{\phi},\varphi,\boldsymbol{p}_{\boldsymbol{\phi}}) - \mathcal{W}^{\text{ele}}(\psi_{\mathcal{B}_0}(\boldsymbol{\psi}_{\mathcal{E}}),\boldsymbol{\phi},\varphi,p_{\boldsymbol{\varphi}}), \tag{54}$$

where the first term $\mathcal{J}(\boldsymbol{\phi})$ on the right hand side of (54) corresponds to the objective function (52), and the remainder terms can be written as

$$\mathcal{W}^{\text{mec}}(\psi_{\mathcal{B}_0}(\boldsymbol{\psi}_{\mathcal{E}}),\boldsymbol{\phi},\varphi,\boldsymbol{p}_{\boldsymbol{\phi}}) = D\Pi(\psi_{\mathcal{B}_0}(\boldsymbol{\psi}_{\mathcal{E}}),\boldsymbol{\phi},\varphi)[\boldsymbol{p}_{\boldsymbol{\phi}}]; \tag{55a}$$

$$\mathcal{W}^{\text{ele}}(\psi_{\mathcal{B}_0}(\boldsymbol{\psi}_{\mathcal{E}}),\boldsymbol{\phi},\varphi,p_{\boldsymbol{\varphi}}) = D\Pi(\psi_{\mathcal{B}_0}(\boldsymbol{\psi}_{\mathcal{E}}),\boldsymbol{\phi},\varphi)[p_{\varphi}], \tag{55b}$$

where (55a) represents the variational statement of the equilibrium equation with $\boldsymbol{p}_{\boldsymbol{\phi}}\in\mathbb{V}_0^{\boldsymbol{\phi}}$ its associated adjoint state (refer to (49a) just replacing $\delta\boldsymbol{\phi}$ with $\boldsymbol{p}_{\boldsymbol{\phi}}$) and (55b) denotes the variational statement of Gauss' law with $p_{\varphi}\in\mathbb{V}_0^{\varphi}$ its associated adjoint state (refer to (49b) just replacing $\delta\varphi$ with p_{φ}).

Whilst the first term on the right hand side of the Lagrangian functional represents the objective function, the last two terms denote two of the variational statements that must be fulfilled (refer to problem (P) in (53)), and enforced via the introduction of the two adjoint states $\boldsymbol{p}_{\boldsymbol{\mathcal{U}}} = \{\boldsymbol{p}_{\phi}, p_{\varphi}\}$, counterpart of the unknown fields $\boldsymbol{\mathcal{U}} = \{\boldsymbol{\phi},\varphi\}$. It is worthwhile to remember that all fields $\{\boldsymbol{\mathcal{U}},\boldsymbol{p}_{\boldsymbol{\mathcal{U}}}\}$ depend implicitly on the set $\boldsymbol{\psi}_{\mathcal{E}}$ of in-surface phase field functions, namely the so-called design variables. This fact will be later exploited in order to obtain the sensitivity of the Lagrangian with respect to the design variables $\psi_{\mathcal{E}^i}$. Before that, the optimality conditions of $\mathcal{L}$ must be computed.

First, the optimality conditions of $\mathcal{L}$ with respect to the adjoint states $\boldsymbol{p}_{\boldsymbol{\mathcal{U}}}$ are defined as

$$D\mathcal{L}(\psi_{\mathcal{B}_0}(\boldsymbol{\psi}_{\mathcal{E}}),\boldsymbol{\mathcal{U}},\boldsymbol{p}_{\boldsymbol{\mathcal{U}}})[\delta\boldsymbol{p}_{\boldsymbol{\phi}}] = -D\Pi(\psi_{\mathcal{B}_0}(\boldsymbol{\psi}_{\mathcal{E}}),\boldsymbol{\phi},\varphi)[\delta\boldsymbol{p}_{\boldsymbol{\phi}}] = 0; \tag{56a}$$

$$D\mathcal{L}(\psi_{\mathcal{B}_0}(\boldsymbol{\psi}_{\mathcal{E}}),\boldsymbol{\mathcal{U}},\boldsymbol{p}_{\boldsymbol{\mathcal{U}}})[\delta p_{\varphi}] = -D\Pi(\psi_{\mathcal{B}_0}(\boldsymbol{\psi}_{\mathcal{E}}),\boldsymbol{\phi},\varphi)[\delta p_{\boldsymbol{\varphi}}] = 0, \tag{56b}$$

where $\delta\boldsymbol{p}_{\phi}\in\mathbb{V}_0^{\boldsymbol{\phi}}$ and $\delta p_{\varphi}\in\mathbb{V}_0^{\varphi}$ represent virtual variations of the corresponding adjoint states, which can be written by simply replacing $\{\delta\boldsymbol{\phi},\delta\varphi\}$ in (49) with $\{\delta\boldsymbol{p}_{\boldsymbol{\phi}},\delta p_{\varphi}\}$, respectively. Solution of above *nonlinear* coupled variational statements permit the computation of the unknown fields $\boldsymbol{\mathcal{U}}$. This solution can be achieved via the Newton-Raphson strategy already described in (50).

Next, the optimality conditions of $\mathcal{L}$ with respect to the fields $\boldsymbol{\mathcal{U}}$ can be formulated as

$$\begin{aligned} D\mathcal{L}(\psi_{\mathcal{B}_0}(\boldsymbol{\psi}_{\mathcal{E}}),\boldsymbol{\mathcal{U}},\boldsymbol{p}_{\boldsymbol{\mathcal{U}}})[\delta\boldsymbol{\phi}] = &- D^2\Pi(\psi_{\mathcal{B}_0}(\boldsymbol{\psi}_{\mathcal{E}}),\boldsymbol{\phi},\varphi)[\boldsymbol{p}_{\boldsymbol{\phi}};\delta\boldsymbol{\phi}] - D^2\Pi(\psi_{\mathcal{B}_0}(\boldsymbol{\psi}_{\mathcal{E}}),\boldsymbol{\phi},\varphi)[p_\varphi,\delta\boldsymbol{\phi}] \\ &+ D\mathcal{J}(\boldsymbol{\phi})[\delta\boldsymbol{\phi}] = 0; \end{aligned} \tag{57a}$$

$$D\mathcal{L}(\psi_{\mathcal{B}_0}(\boldsymbol{\psi}_{\mathcal{E}}),\boldsymbol{\mathcal{U}},\boldsymbol{p}_{\boldsymbol{\mathcal{U}}})[\delta\varphi] = - D^2\Pi(\psi_{\mathcal{B}_0}(\boldsymbol{\psi}_{\mathcal{E}}),\boldsymbol{\phi},\varphi)[\boldsymbol{p}_{\boldsymbol{\phi}};\delta\varphi] - D^2\Pi(\psi_{\mathcal{B}_0}(\boldsymbol{\psi}_{\mathcal{E}}),\boldsymbol{\phi},\varphi)[p_\varphi;\delta\varphi] = 0, \tag{57b}$$

where the second directional derivative terms featuring in (57) are presented in (51), just by replacing $\{\delta\boldsymbol{\phi},\delta\varphi\}$ with $\{\boldsymbol{p}_{\boldsymbol{\phi}},p_\varphi\}$, and $\{\Delta\boldsymbol{\phi},\Delta\varphi\}$ with $\{\delta\boldsymbol{\phi},\delta\varphi\}$, respectively. Solution of the above *linear* variational statements (57) result in the adjoint states $\boldsymbol{p}_{\boldsymbol{\mathcal{U}}}$.

4.3. The sensitivity of the optimisation Lagrangian $\mathcal{L}$

Once the fields and the adjoint states $\{\boldsymbol{\mathcal{U}},\boldsymbol{p}_{\boldsymbol{\mathcal{U}}}\}$ have been obtained from the solution of the above optimality conditions (56) and (57), it is possible to proceed to the computation of the sensitivity of the Lagrangian $\mathcal{L}$ with respect to the in-surface phase-field functions $\psi_{\mathcal{E}^i}$. At optimality, that is, when (56) and (57) are satisfied, the Lagrangian functional $\mathcal{L}$ can be re-written solely in terms of the set of design variables $\boldsymbol{\psi}_{\mathcal{E}}$, that is

$$\mathcal{F}(\boldsymbol{\psi}_{\mathcal{E}}) = \mathcal{L}(\psi_{\mathcal{B}_0}(\boldsymbol{\psi}_{\mathcal{E}}),\boldsymbol{\mathcal{U}},\boldsymbol{p}_{\boldsymbol{\mathcal{U}}})|_{\text{optimality}}\,, \tag{58}$$

and this permits the so-called sensitivity of the Lagrangian (i.e. $\partial_{\psi_{\mathcal{E}^i}}\mathcal{F}(\boldsymbol{\psi}_{\mathcal{E}})$) to be computed from the directional derivative of $\mathcal{F}$ as

$$D\mathcal{F}(\boldsymbol{\psi}_{\mathcal{E}})[\Delta\psi_{\mathcal{E}^i}] = \partial_{\psi_{\mathcal{E}^i}}\mathcal{F}(\boldsymbol{\psi}_{\mathcal{E}})\,\Delta\psi_{\mathcal{E}^i}. \tag{59}$$

Referring to equation (58), the sensitivity can be obtained as

$$\begin{aligned} D\mathcal{F}(\boldsymbol{\psi}_{\mathcal{E}})[\Delta\psi_{\mathcal{E}^i}] = &\, D\mathcal{L}(\psi_{\mathcal{B}_0},\boldsymbol{\mathcal{U}},\boldsymbol{p}_{\boldsymbol{\mathcal{U}}})[D\psi_{\mathcal{B}_0}(\boldsymbol{\psi}_{\mathcal{E}})[\Delta\psi_{\mathcal{E}^i}]] \\ &+ \underbrace{D\mathcal{L}(\psi_{\mathcal{B}_0},\boldsymbol{\mathcal{U}},\boldsymbol{p}_{\boldsymbol{\mathcal{U}}})[D\boldsymbol{p}_{\boldsymbol{\mathcal{U}}}[\Delta\psi_{\mathcal{E}^i}]]}_{=0\text{ (optimality (56))}} + \underbrace{D\mathcal{L}(\psi_{\mathcal{B}_0},\boldsymbol{\mathcal{U}},\boldsymbol{p}_{\boldsymbol{\mathcal{U}}})[D\boldsymbol{\mathcal{U}}[\Delta\psi_{\mathcal{E}^i}]]}_{=0\text{ (optimality (57))}}, \end{aligned} \tag{60}$$

where application of the optimality conditions has been made use in (60). Above equation (60) can be expanded as

$$D\mathcal{F}(\boldsymbol{\psi}_{\mathcal{E}})[\Delta\psi_{\mathcal{E}^i}] = \left(-\int_{\mathcal{B}_0} g(\boldsymbol{X},\psi_{\mathcal{B}_0})\frac{\partial\psi_{\mathcal{B}_0}(\boldsymbol{X},\boldsymbol{\psi}_{\mathcal{E}})}{\partial\psi^i_{\mathcal{E}}}dV\right)\Delta\psi_{\mathcal{E}^i}, \tag{61}$$

where the term $\frac{\partial\psi_{\mathcal{B}_0}(\boldsymbol{X},\boldsymbol{\psi}_{\mathcal{E}})}{\partial\psi^i_{\mathcal{E}}}$ can be obtained after solution of (30) and the term $g(\boldsymbol{X},\boldsymbol{\psi}_{\mathcal{B}_0})$ is derived from (49), (54) and (55) yielding

$$g(\boldsymbol{X},\boldsymbol{\psi}_{\mathcal{B}_0}) = \boldsymbol{\nabla}_0\boldsymbol{p}_{\boldsymbol{\phi}} : \partial_{\psi_{\mathcal{B}_0}}\boldsymbol{P}(\psi_{\mathcal{B}_0},\boldsymbol{F},\boldsymbol{E}_0) + \boldsymbol{\nabla}_0 p_\varphi\cdot\partial_{\psi_{\mathcal{B}_0}}\boldsymbol{D}_0(\psi_{\mathcal{B}_0},\boldsymbol{F},\boldsymbol{E}_0), \tag{62}$$

with $\partial_{\psi_{\mathcal{B}_0}}\boldsymbol{P}(\psi_{\mathcal{B}_0},\boldsymbol{F},\boldsymbol{E}_0)$ and $\partial_{\psi_{\mathcal{B}_0}}\boldsymbol{D}_0(\psi_{\mathcal{B}_0},\boldsymbol{F},\boldsymbol{E}_0)$ computed from (37) as

$$\partial_{\psi_{\mathcal{B}_0}}\boldsymbol{P}(\psi_{\mathcal{B}_0},\boldsymbol{F},\boldsymbol{E}_0) = \quad f'(\psi_{\mathcal{B}_0})\partial_{\boldsymbol{F}}\Psi_{em}(\boldsymbol{F},\boldsymbol{E}_0); \tag{63a}$$

$$\partial_{\psi_{\mathcal{B}_0}}\boldsymbol{D}_0(\psi_{\mathcal{B}_0},\boldsymbol{F},\boldsymbol{E}_0) = -f'(\psi_{\mathcal{B}_0})\partial_{\boldsymbol{E}_0}\Psi_{em}(\boldsymbol{F},\boldsymbol{E}_0). \tag{63b}$$

The sensitivity of the Lagragian $\mathcal{F}$ with respect to the in-surface phase field functions $\psi_{\mathcal{E}^i}$, that is, $\partial_{\psi_{\mathcal{E}^i}}\mathcal{F}(\boldsymbol{\psi}_{\mathcal{E}})$ is a key ingredient to the evolution of the in-surface phase field functions $\psi_{\mathcal{E}^i}$, which is presented next.

4.4. Evolution of the in-surface phase field functions

In order to describe the evolution of the surface electrode regions $\mathcal{E}^i_{\text{Elec}}$ during the optimisation process, a pseudo-time parameter $\tau \in [\tau_0, \tau_m]$ is introduced, where τ is associated with a continuously evolving topology optimisation. Thus, the configuration of the electrodes can be evolved in pseudo-time through an optimisation process from configuration $\mathcal{E}^i_{\text{Elec}}(\tau_0)$ to configuration $\mathcal{E}^i_{\text{Elec}}(\tau_m)$. The introduction of this pseudo-time parameter implies the following modification with respect to equation (25),

$$\forall \boldsymbol{\xi} \in \mathcal{E}^i, \forall \tau \in [\tau_0, \tau_m], \begin{cases} \psi_{\mathcal{E}^i}(\boldsymbol{\xi}, \tau) = 1; & \text{if } \boldsymbol{\xi} \in \mathcal{E}^i_{\text{Elec}}(\tau); \\ 0 < \psi_{\mathcal{E}^i}(\boldsymbol{\xi}, \tau) < 1; & \text{if } \boldsymbol{\xi} \in \partial\mathcal{E}^i_{\text{Elec}}(\tau); \\ \psi_{\mathcal{E}^i}(\boldsymbol{\xi}, \tau) = 0; & \text{if } \boldsymbol{\xi} \in \mathcal{E}^i \setminus \left(\mathcal{E}^i_{\text{Elec}}(\tau) \cup \partial\mathcal{E}^i_{\text{Elec}}(\tau)\right). \end{cases} \tag{64}$$

In this work, the evolution of the in-surface phase field functions is carried out using the so-called (non-conservative) Allen-Cahn approach, specifically as formalised in [60]. With that in mind, the following initial boundary value problem can be used to evolve each of the in-surface phase field functions

$$\partial_\tau \psi_{\mathcal{E}^i} = \kappa \boldsymbol{\nabla}^2_{\mathcal{E}_i} \psi_{\mathcal{E}_i} - \partial_{\psi_{\mathcal{E}^i}} \left(\frac{1}{4} \Phi(\psi_{\mathcal{E}^i}) + \eta\, \mathcal{G}_{\mathcal{E}^i}(\boldsymbol{\xi}) h(\psi_{\mathcal{E}^i}) \right); \qquad \text{in } \mathcal{E}_i \times [\tau_0, \tau_m]; \tag{65a}$$

$$0 = \boldsymbol{\nabla}_{\mathcal{E}^i} \psi_{\mathcal{E}^i} \cdot \boldsymbol{N}|_{\partial\mathcal{E}^i}; \qquad \text{on } \partial\mathcal{E}_i \times [\tau_0, \tau_m]; \tag{65b}$$

$$\psi_{\mathcal{E}^i}|_{\tau_0} = \psi^0_{\mathcal{E}^i}; \qquad \text{in } \mathcal{E}_i; \tag{65c}$$

where $\boldsymbol{\nabla}_{\mathcal{E}_i}$ and $\boldsymbol{\nabla}^2_{\mathcal{E}_i}$ represent the in-surface $\mathcal{E}^i$ gradient and Laplacian operators, respectively, and $\boldsymbol{N}|_{\partial\mathcal{E}^i}$ is the in-surface $\mathcal{E}^i$ outward unit vector. In addition, κ and η are non-negative numbers (to be set during the optimisation process), $\mathcal{G}_{\mathcal{E}^i}(\boldsymbol{\xi})$ is a scalar field proportional to the sensitivity $\partial_{\psi_{\mathcal{E}^i}} \mathcal{F}(\boldsymbol{\psi}_{\mathcal{E}})$ (59), and $\Phi(\psi_{\mathcal{E}^i})$ and $h(\psi_{\mathcal{E}^i})$ are polynomials given by

$$\Phi(\psi_{\mathcal{E}^i}) = \psi^2_{\mathcal{E}^i}(1 - \psi_{\mathcal{E}^i})^2; \qquad h(\psi_{\mathcal{E}^i}) = \psi^3_{\mathcal{E}^i}(6\psi^2_{\mathcal{E}^i} - 15\psi_{\mathcal{E}^i} + 10), \tag{66}$$

where $\Phi(\psi_{\mathcal{E}^i})$ denotes the well-known double well potential (see Figure 9) and $h(\psi_{\mathcal{E}^i})$ is a carefully designed polynomial satisfying that $h'(\psi_{\mathcal{E}^i}) = 30\Phi(\psi_{\mathcal{E}^i})$ and $h(0) = 0$.

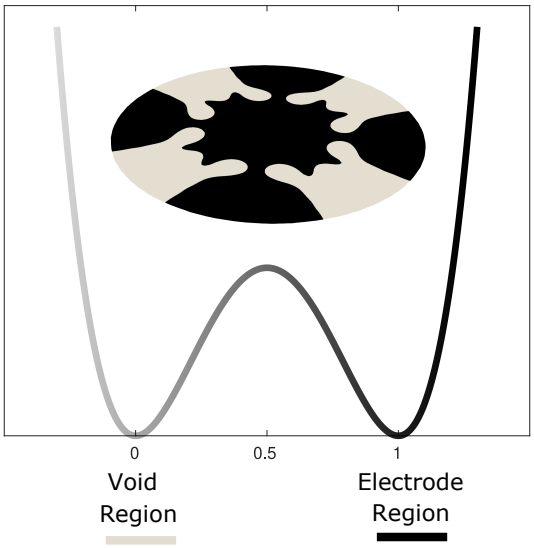

Figure 9: Double well potential representation.

The first term on the right hand side of (65a) represents a diffusion term which only acts on the phase transition region and the second term on the right hand side of (65a) involves the

sensitivity of the design optimisation problem in conjunction with the double well potential which drive the evolution of the phase transition region. A variational statement for the initial boundary value problem defined in (65) can be defined as

$$\int_{\mathcal{E}^i} \partial_\tau \psi_{\mathcal{E}^i} \delta\psi_{\mathcal{E}^i}\, dA = -\int_{\mathcal{E}^i} \kappa \boldsymbol{\nabla}_{\mathcal{E}^i}\psi_{\mathcal{E}^i}\cdot\boldsymbol{\nabla}_{\mathcal{E}^i}\delta\psi_{\mathcal{E}^i}\, dA + \int_{\mathcal{E}^i}\psi_{\mathcal{E}^i}(1-\psi_{\mathcal{E}^i})r(\boldsymbol{\xi},\psi_{\mathcal{E}^i})\delta\psi_{\mathcal{E}^i}\, dA; \tag{67a}$$

$$\psi_{\mathcal{E}^i}|_{\tau_0} = \psi^0_{\mathcal{E}^i}; \quad \text{in } \mathcal{E}_i, \tag{67b}$$

where $\delta\psi_{\mathcal{E}^i} \in \mathbb{V}_0^{\psi_{\mathcal{E}^i}}$ is a suitable virtual field and the scalar field $r(\boldsymbol{\xi},\psi_{\mathcal{E}^i})$ is given by

$$r(\boldsymbol{\xi},\psi_{\mathcal{E}^i}) = \psi_{\mathcal{E}^i} - \frac{1}{2} - 30\eta\mathcal{G}_{\mathcal{E}^i}(\boldsymbol{\xi})\psi_{\mathcal{E}^i}(1-\psi_{\mathcal{E}^i}). \tag{68}$$

All in all, the solution of the initial boundary value problem (67) requires *a priori* knowledge of the sensitivity (refer to (61) and (62)), which needs the prior solution of the optimality conditions of the Lagrangian $\mathcal{L}$ to obtain the unknown fields (refer to (56)) and the adjoint states (refer to (57)). Moreover, solution of (56), (57) and the computation of the sensitivities (61) require the previous knowledge of the extended volume phase field function (30) and the use of the energy interpolation ansatz (31) and (34).

4.5. Pseudo-time marching scheme

Following [60] and considering the pseudo-time slab $[\tau_n,\tau_{n+1}]$ with $\Delta\tau = \tau_{n+1}-\tau_n$, an implicit one-step marching scheme can be used to advance the solution from $\psi^n_{\mathcal{E}^i}$ to $\psi^{n+1}_{\mathcal{E}^i}$ via time discretisation of (67) as

$$\mathcal{T}(\psi^{n+1}_{\mathcal{E}^i}) = \int_{\mathcal{E}^i}\left[\left(\frac{\psi^{n+1}_{\mathcal{E}^i}-\psi^n_{\mathcal{E}^i}}{\Delta\tau}\right)\delta\psi_{\mathcal{E}^i} + \kappa\boldsymbol{\nabla}_{\mathcal{E}^i}\psi^{n+1}_{\mathcal{E}^i}\cdot\boldsymbol{\nabla}_{\mathcal{E}^i}\delta\psi_{\mathcal{E}^i} - S(\psi^n_{\mathcal{E}^i},\psi^{n+1}_{\mathcal{E}^i})r(\boldsymbol{\xi},\psi^n_{\mathcal{E}^i})\delta\psi_{\mathcal{E}^i}\right] dA = 0, \tag{69}$$

with

$$S(\psi^n_{\mathcal{E}^i},\psi^{n+1}_{\mathcal{E}^i}) = \begin{cases} \psi^{n+1}_{\mathcal{E}^i}(1-\psi^n_{\mathcal{E}^i}); & \text{if } r(\boldsymbol{\xi},\psi^n_{\mathcal{E}^i}) \le 0; \\ \psi^n_{\mathcal{E}^i}(1-\psi^{n+1}_{\mathcal{E}^i}); & \text{if } r(\boldsymbol{\xi},\psi^n_{\mathcal{E}^i}) > 0. \end{cases} \tag{70}$$

Contrary to Reference [60], the diffusion term (i.e. second term within the integrand in (69)) is discretised implicitly in order to enhance the stability of the time marching scheme. Solution of (69) is obtained as

$$D\mathcal{T}(\psi_{\mathcal{E}^i})[\Delta\psi_{\mathcal{E}^i}] = -\mathcal{T}(\psi^n_{\mathcal{E}^i}); \qquad \psi^{n+1}_{\mathcal{E}^i} = \psi^n_{\mathcal{E}^i} + \Delta\psi_{\mathcal{E}^i}. \tag{71}$$

Notice that the semi-implicit nature of the term $S(\psi^n_{\mathcal{E}^i},\psi^{n+1}_{\mathcal{E}^i})$ in (70) is carefully chosen to ensure ellipticity of the tangent operator in (71) (i.e. $D\mathcal{T}(\psi_{\mathcal{E}^i})[\delta\psi_{\mathcal{E}^i}] > 0$) and thus the solution of (71).

4.6. Algorithmic flowchart

Algorithm 1 summarises the flowchart of actions of the in-silico design platform.

Initialisation of in-surface phase-field functions $\psi_{\mathcal{E}^i}$ at each interface for $\mathcal{E}^i$

Extension of in-surface phase field functions to the volume, obtaining $\psi_{\mathcal{B}_0}$ (30)

Initialise pseudo-time: $\tau = 0$

Solve $\{\boldsymbol{\phi}, \varphi\}$ from optimality condition (56)

Solve $\{\boldsymbol{p}_{\boldsymbol{\phi}}, p_{\varphi}\}$ from optimality condition (57)

Evaluate objective function $\mathcal{J}(\boldsymbol{\phi})|_{\tau=0}$

Set optimisation parameters $\{\Delta\tau, \kappa, \eta\}$ for (69)-(70)

Define optimisation tolerance ($tol.$) and variable $e > tol.$

while $e > tol.$ **do**

  $\tau \leftarrow \tau + \Delta\tau$

  Compute $\frac{\partial \psi_{\mathcal{B}_0}(\boldsymbol{X}, \boldsymbol{\psi}_{\mathcal{E}})}{\partial \psi^i_{\mathcal{E}}}$

  Get sensitivities $\partial_{\psi_{\mathcal{E}^i}} \mathcal{F}(\boldsymbol{\psi}_{\mathcal{E}})$ from (59)-(61)

  Evolve phase-field functions $\psi_{\mathcal{E}^i}$ using (69)-(70)

  if $\psi_{\mathcal{E}^i} > 1$ **then**
  | $\psi_{\mathcal{E}^i} = 1$
  else
  | Do not correct
  end
  if $\psi_{\mathcal{E}^i} < 0$ **then**
  | $\psi_{\mathcal{E}^i} = 0$
  else
  | Do not correct
  end

  Extension of in-surface phase field functions to the volume, obtaining $\psi_{\mathcal{B}_0}$ (30)

  Solve $\{\boldsymbol{\phi}, \varphi\}$ from optimality condition (56)

  Solve $\{\boldsymbol{p}_{\boldsymbol{\phi}}, p_{\varphi}\}$ from optimality condition (57)

  Evaluate objective function $\mathcal{J}(\boldsymbol{\phi})|_{\tau}$

  Define $e = \mathcal{J}|_{\tau} - \mathcal{J}|_{\tau-\Delta\tau}$

end

Algorithm 1: Pseudo-code of the in-silico meso-architecture design.

5. Numerical examples

This Section presents a series of numerical examples in order to assess the capabilities of the proposed modelling approach. First, an example is presented in order to demonstrate the accuracy of the diffuse interface treatment approach in comparison with the sharp interface approach. A relatively simple layer-by layer DE thin rectangular configuration will be simulated in order to attain a complex bending actuation mode in the form of an S-shape. Next, various non-trivial electrode meso-architectures will be in-silico obtained for different design objective functions for both circular and square DE films.

In all the subsequent examples, tri-quadratic interpolations for both displacement and electric potential fields have been included. Notice that the nearly-incompressible nature of DEs and the generally small thickness of DE devices pose serious limitations for the application of low

order finite element discretisations, prone to exhibit volumetric and bending locking under both scenarios [40, 41].

5.1. Accuracy of the diffuse interface approach with respect to the sharp interface approach

The objective of this example is to demonstrate the accuracy of the diffuse interface approach described in Section 3.2 with respect to the *exact* sharp interface approach in Section 3.1. For that, we consider the set up displayed in Figure 10$_a$, where the electrodes adopt a simple rectangular geometry. Regarding the sharp interface approach in Section 3.1, the Dirichlet boundary conditions for the electric potential are restricted to the blue or red areas in the figure (in compliance with equation (23e)) and the electromechanical energy of the elastomeric material does not need to be interpolated (a value of $\psi_{\mathcal{B}_0} = 1$ is adopted everywhere). On the contrary, when making use of the diffuse interface approach, the Dirichlet boundary conditions are not restricted to the red or blue areas, but are applied on the entire surface with same value of coordinate Z. For instance, a value of $\varphi = 1000\,V$ is applied in the first intercalated surface (at $Z = \min(Z) + L_Z/5$) at every point X and Y (and not just in the region $X > \min(X) + L_X/2$). In addition, the following in-surface phase functions $\{\Psi_{\mathcal{E}^1}, \Psi_{\mathcal{E}^2}, \Psi_{\mathcal{E}^3}, \Psi_{\mathcal{E}^4}\}$, located at the surfaces $Z = \{\min(Z)+L_Z/5, \min(Z)+2L_Z/5, \min(Z)+3L_Z/5, \min(Z)+4L_Z/5\}$, are defined compatible with the exact location of the electrodes, i.e.

$$\Psi_{\mathcal{E}^1} = \begin{cases} 1; & X >= \min(X) + L_X/2 \\ 0; & X < \min(X) + L_X/2 \end{cases} \qquad \Psi_{\mathcal{E}^2} = \begin{cases} 1; & X >= \min(X) + L_X/2 \\ 0; & X < \min(X) + L_X/2 \end{cases}$$
$$\Psi_{\mathcal{E}^3} = \begin{cases} 1; & X <= \min(X) + L_X/2 \\ 0; & X > \min(X) + L_X/2 \end{cases} \qquad \Psi_{\mathcal{E}^4} = \begin{cases} 1; & X <= \min(X) + L_X/2 \\ 0; & X > \min(X) + L_X/2 \end{cases} \tag{72}$$

Making use of the values of $\{\Psi_{\mathcal{E}^1}, \Psi_{\mathcal{E}^2}, \Psi_{\mathcal{E}^3}, \Psi_{\mathcal{E}^4}\}$ in (72), we then compute the volume extended phase-field function $\psi_{\mathcal{B}_0}$ according to equation (27) and (28), which permits to interpolate the electromechanical energy according to equations (31) and (33). For this example, the material parameters used are summarised in Table 1.

μ_1 (Pa)	μ_2 (Pa)	λ (Pa)	ε_r
5×10^4	5×10^4	10^8	4.8

Table 1: Material parameters of the electromechanical constitutive model considered in the numerical examples in Section 5.1. See equations (7) and (8).

From the analysis of these two methodologies, it can be observed from Figure 10$_b$ that the electrically induced deformation predicted by the diffused interface approach (meshed domain) overlaps to that predicted by the exact sharp interface approach (solid grey domain), which confirms the good accuracy of the diffuse interface approach, convenient when the electrodes evolve and adopt potentially complex geometries along the topology optimisation process.

5.2. Optimal design of electro meso-architecture for shape morphing elastomers

The objective of this section is to reveal the performance and suitability of the proposed design methodology, described throughout the preceding sections and concisely summarised in the pseudo-code in Algorithm 1. In the following numerical examples, DE designs characterised by simple geometries (i.e. thin DE with circular or square in-plane geometry) are the focus of our numerical studies. Furthermore, the layer-by-layer layout of the DE designs considered (see Section 3) is comprised of the following common design features:

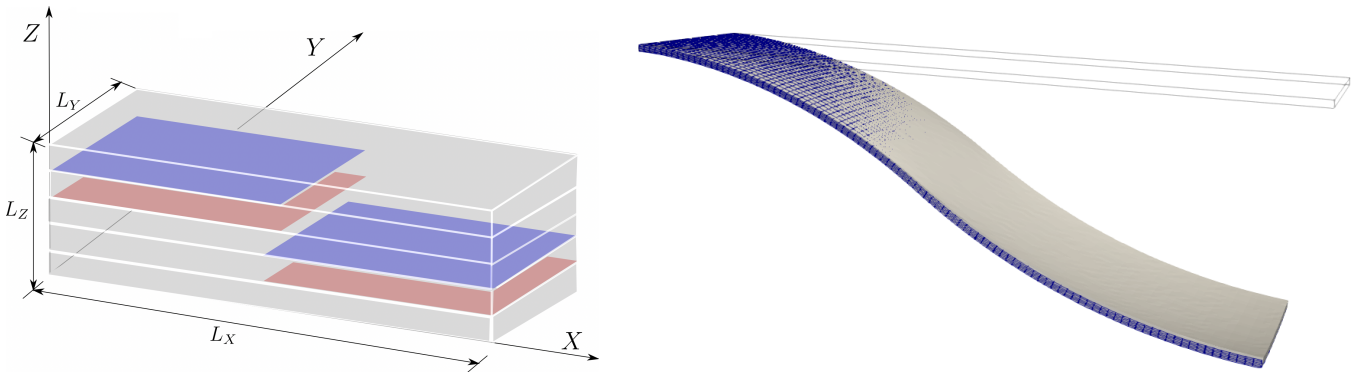

(a) (b)

Figure 10: Accuracy of diffuse interface treatment of electrodes: (a) Geometry and set up for verification, completely fixed at $X = \min(X)$. Five elastomer layers intercalated with four inner electrodes. Red and blue electrodes subjected to $+1000\,V$ and $-1000\,V$, respectively. $\{L_X, L_Y, L_Z\} = \{5 \times 10^{-2}, 1.25 \times 10^{-2}, 5 \times 10^{-4}\}$ (m); (b) Undeformed configuration (transparent) and deformed configurations when considering the exact sharp interface approach (in grey solid color) and the diffuse interface approach (domain with blue mesh).

- Six layers of DE layers are considered, $\{\mathcal{B}_0^1, \ldots, \mathcal{B}_0^6\}$.
- Five intercalated electrode regions $\mathcal{E} = \{\mathcal{E}^1, \ldots, \mathcal{E}^5\}$ are considered.
- Constant thickness of all six elastomeric layers.

The aim of these examples is to obtain a suitable electrode layout complying with the above features such that certain desired morphological attributes are exhibited by the electrically actuated DE device. With regards to the constitutive model used for the elastomeric layers, we use the energy interpolation scheme described by equations (31) and (34) for the definition of the interpolated free energy density $\Psi(\boldsymbol{X}, \boldsymbol{F}, \boldsymbol{E}_0)$. Specifically, in all the examples, the mechanical contribution of the free energy density, namely $\Psi_m(\boldsymbol{F})$, corresponds to that of a Mooney-Rivlin material (see equation (7)) and the electromechanical energy contribution $\Psi_{em}(\boldsymbol{F}, \boldsymbol{E}_0)$ corresponds with that of an ideal dielectric elastomer (see equation (8)). The material parameters featuring on each of these two contributions are summarised in Table 2, and are common for all the numerical examples presented.

μ_1 (Pa)	μ_2 (Pa)	λ (Pa)	ε_r
5×10^4	5×10^4	10^8	4.8

Table 2: Material parameters of the electromechanical constitutive model considered in the numerical examples in Sections 5.2.2 and 5.2.3. See equations (7) and (8).

5.2.1. Numerical example 0

The objective of this preliminar example is to demonstrate the capability of the proposed topology optimisation-based design approach to yield designs which are consistent with those reported experimentally, and in particular, with those in Reference [21]. With that objective in mind, considering the target configuration $\boldsymbol{\phi}^*$ in Reference [21] obtained as a result of a distribution of electrodes similar to that in Figure 11, we define the following objective function

$$\mathcal{J} = \int_{\mathcal{B}_0} \frac{1}{2} ||\boldsymbol{\phi} - \boldsymbol{\phi}^*||^2 \, dV \tag{73}$$

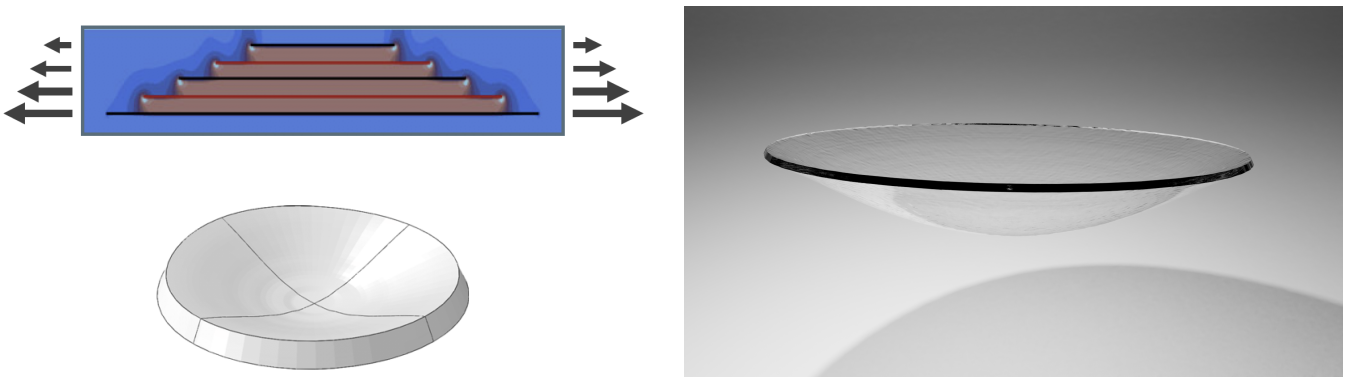

(a) (b)

Figure 11: Example 0: (a) Qualitative distribution of electrodes over a section of the DE device that yields a deformed configuration compatible with that on the right hand-side of the figure; (b) Deformed configuration obtained from the topology optimisation (inverse) problem. Figure (a) taken from [21].

Figure 12_a shows the initial seed that has been considered in order to minimise the objective function in equation (73). After 170 iterations, the final distribution of electrodes obtained is very similar to that in Figure 11, where 7 layers of electrodes have been used. The optimal distribution of electrode layers can indeed be observed in Figure 12_b-$_i$. Furthermore, the deformed configuration obtained for various values of electric potential is also shown in Figure 11_b, very similar to that extracted from Figure 11_a in Reference [21].

5.2.2. Numerical example 1

The geometry considered in this example is depicted in Figure $(13)_a$. The initial seed (at pseudo-time $\tau = 0$) for the phase-field functions, namely $\{\psi_{\mathcal{E}^1}(0), \dots, \psi_{\mathcal{E}^5}(0)\}$ at the five electrode interfaces $\{\mathcal{E}^1, \dots, \mathcal{E}^5\}$ is displayed in Figure $(13)_b$ (all five interfaces are initialised in the same manner), where the red colour is associated with a value of $\psi_{\mathcal{E}^i}(0) = 1$ (i.e. regions $\mathcal{E}^i_{\text{Elec}}(0)$) whilst the blue color is associated with $\psi_{\mathcal{E}^i}(0) = 0$ (i.e. region $\mathcal{E} \setminus \mathcal{E}^i_{\text{Elec}}(0) \cup \partial\mathcal{E}^i_{\text{Elec}}(0)$)). A $Q2$ Finite Element discretisation of the geometry in $(13)_a$ has been carried out, comprising of six layers of elements across the thickness of the DE device (Z direction) with a total of 98415 nodes for both unknown fields $\{\boldsymbol{\phi}, \varphi\}$.

Two different designs have been investigated for the DE layout described above. These correspond with two different actuation modes described as follows. **Actuation mode 1** is induced by minimising the vertical (Z direction) displacement of control points $\{B, D\}$ (see Figure $(13)_a$), whilst maximising that of points $\{A, C\}$. **Actuation mode 2** is induced by maximising the vertical (Z direction) displacement of control points $\{B, A, D, C\}$ whilst minimising that of $\{E, H, G, C\}$. Their respective objective functions can be mathematically stated as

$$\mathcal{J}(\boldsymbol{\phi})|_{\text{mode1}} = -\left(\boldsymbol{\phi}(\boldsymbol{X}_A) - \boldsymbol{X}_A + \boldsymbol{\phi}(\boldsymbol{X}_C) - \boldsymbol{X}_C\right) \cdot \boldsymbol{E}_3 + \left(\boldsymbol{\phi}(\boldsymbol{X}_A) - \boldsymbol{X}_A + \boldsymbol{\phi}(\boldsymbol{X}_C) - \boldsymbol{X}_C\right) \cdot \boldsymbol{E}_3; \tag{74a}$$

$$\begin{aligned}\mathcal{J}(\boldsymbol{\phi})|_{\text{mode2}} = &-\left(\boldsymbol{\phi}(\boldsymbol{X}_B) - \boldsymbol{X}_B + \boldsymbol{\phi}(\boldsymbol{X}_A) - \boldsymbol{X}_A + \boldsymbol{\phi}(\boldsymbol{X}_D) - \boldsymbol{X}_D + \boldsymbol{\phi}(\boldsymbol{X}_C) - \boldsymbol{X}_C\right) \cdot \boldsymbol{E}_3 \\ &+ \left(\boldsymbol{\phi}(\boldsymbol{X}_E) - \boldsymbol{X}_E + \boldsymbol{\phi}(\boldsymbol{X}_H) - \boldsymbol{X}_H + \boldsymbol{\phi}(\boldsymbol{X}_G) - \boldsymbol{X}_G + \boldsymbol{\phi}(\boldsymbol{X}_F) - \boldsymbol{X}_F\right) \cdot \boldsymbol{E}_3. \end{aligned} \tag{74b}$$

Figure 14 shows the electrode layouts for the five interfaces $\{\mathcal{E}^1, \dots, \mathcal{E}^5\}$ for **actuation mode 1**. A more detailed view of the layer-by-layer design can be observed in Figure 14_b, where the intercalated electrode layers are displayed in red and blue, and where the Z dimension of the design has been extruded for visualisation purposes. Figure 15 shows the deformed configuration corresponding with the optimised layout in Figure 14 under increasing electrical actuation. Clearly, the final shape of the electrically deformed DE design is in agreement with the objective function $\mathcal{J}(\boldsymbol{\phi})|_{\text{mode1}}$ in equation (74a).

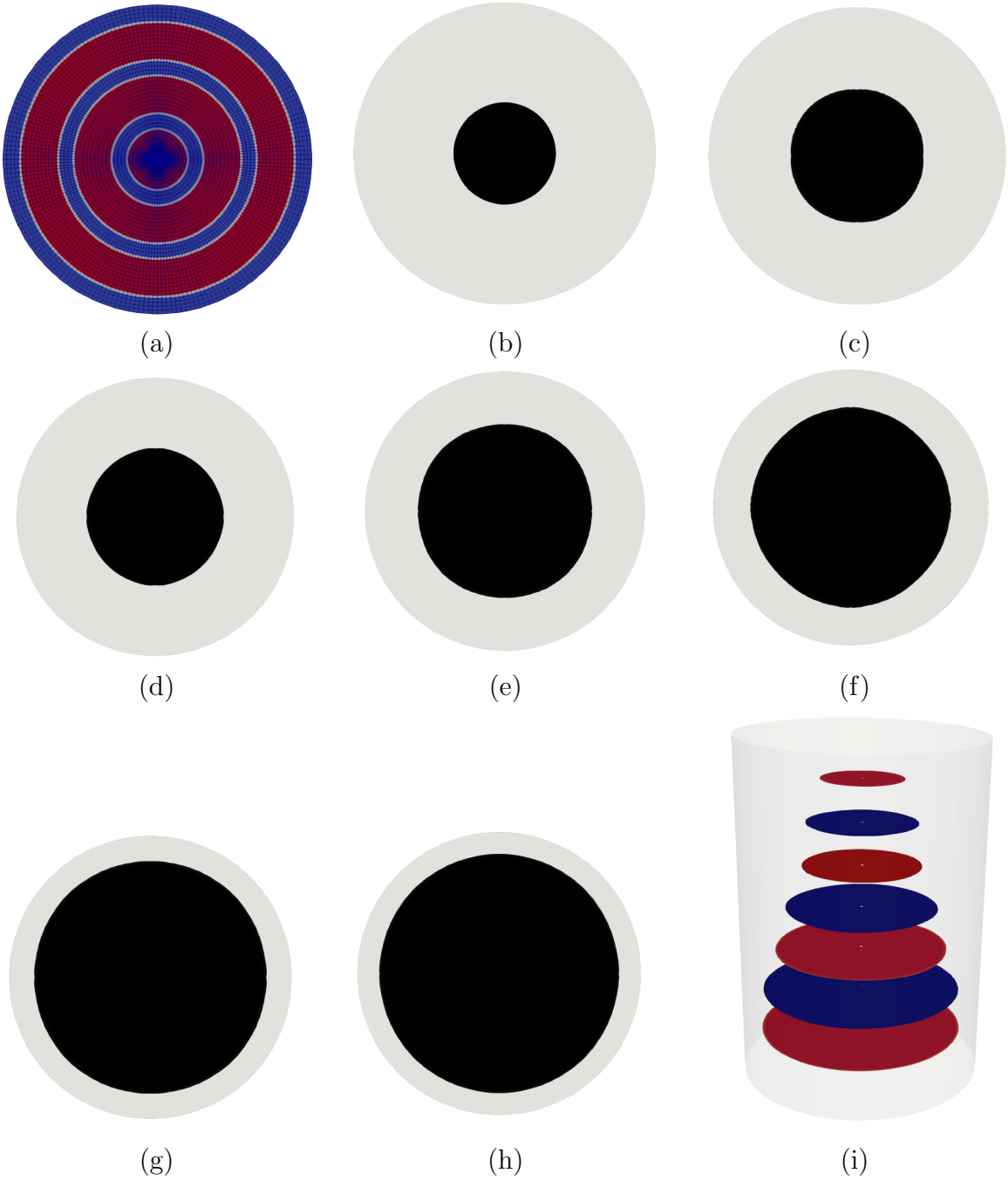

Figure 12: Example 0: (a) Initial seed considered; (b)-(h) Final distribution of the phase-field functions at final TO iteration, namely $\{\psi_{\mathcal{E}^1}(\tau_m), \ldots, \psi_{\mathcal{E}^7}(\tau_m)\}$. Black colour is associated with $\psi_{\mathcal{E}^i} = 1$ and grey colour, with $\psi_{\mathcal{E}^i} = 0$. (i) Display of layer-by-layer layout with intercalated optimal electrode distribution (a threshold value of $\psi_{\mathcal{E}^i=0.5}$ has been used) where the Z dimension of the DE device has been enlarged for visualisation purposes.

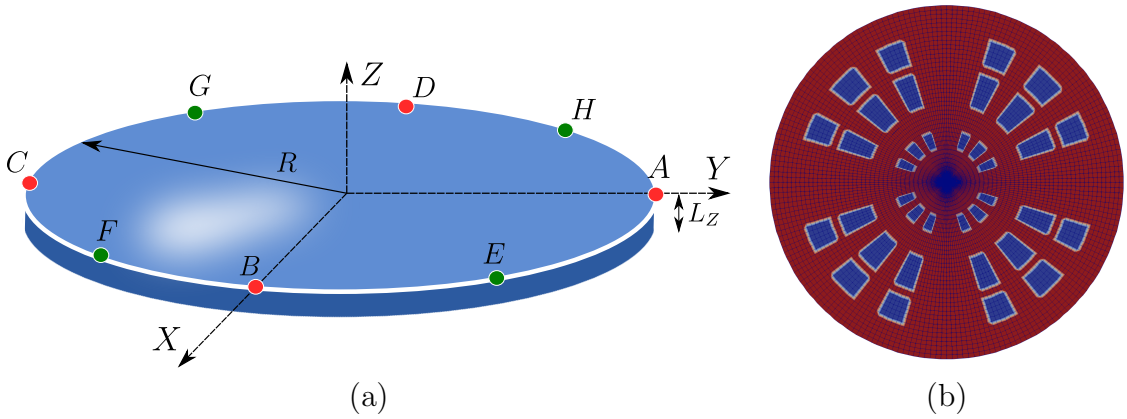

Figure 13: Example 1: (a) Geometry of the DE with $\{R, L_Z\} = \{1, 10^{-3}\}$ (m) and control points for inducing the desired actuation modes when electrical actuation is applied; (b) Initial seed for all the phase-field functions $\{\psi_{\mathcal{E}^1}(0), \ldots, \psi_{\mathcal{E}^5}(0)\}$.

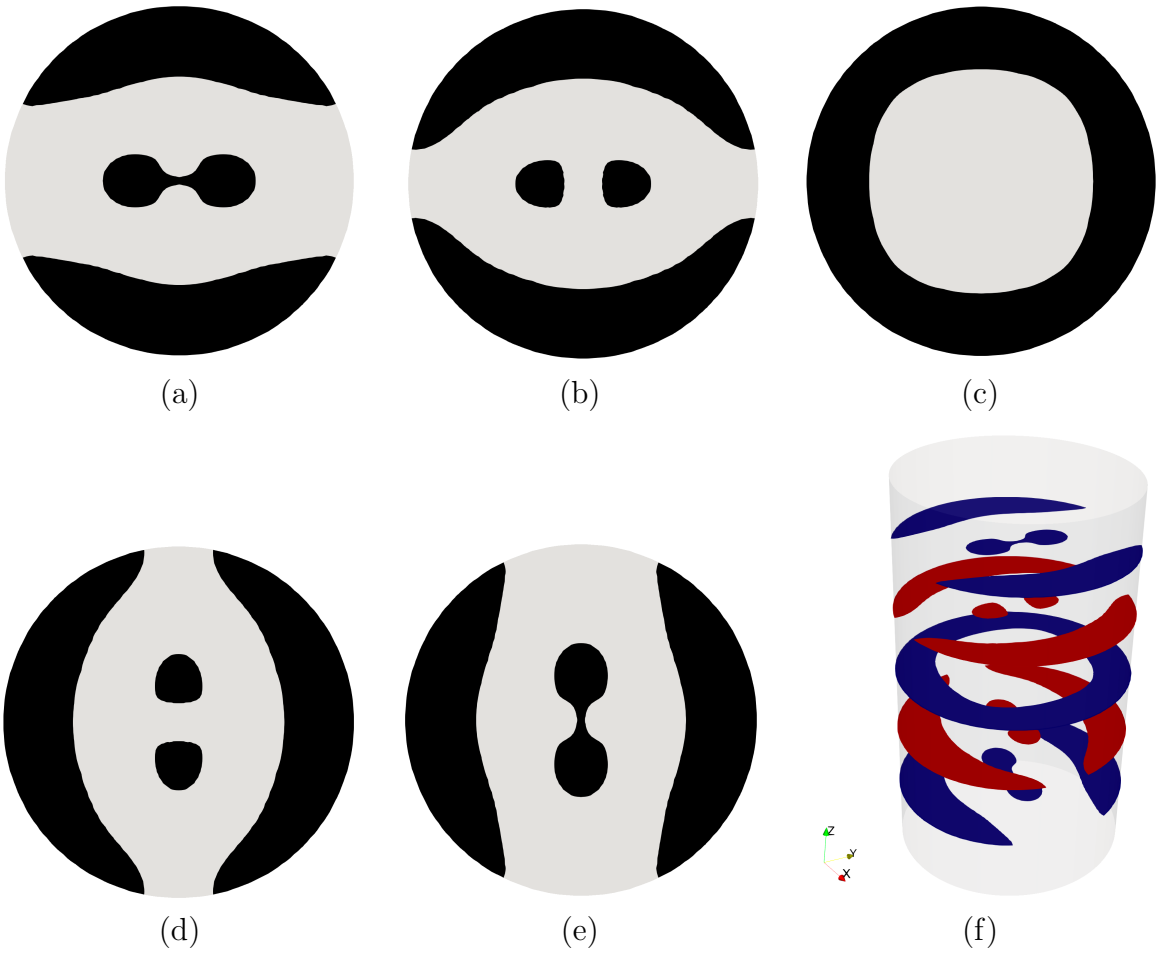

Figure 14: Example 1 (**actuation mode 1**): (a)-(e) Final distribution of the phase-field functions at final TO iteration, namely $\{\psi_{\mathcal{E}^1}(\tau_m), \ldots, \psi_{\mathcal{E}^5}(\tau_m)\}$. Black colour is associated with $\psi_{\mathcal{E}^i} = 1$ and grey colour, with $\psi_{\mathcal{E}^i} = 0$. (f) Display of layer-by-layer layout with intercalated optimal electrode distribution (a threshold value of $\psi_{\mathcal{E}^i=0.5}$ has been used) where the Z dimension of the DE device has been enlarged for visualisation purposes.

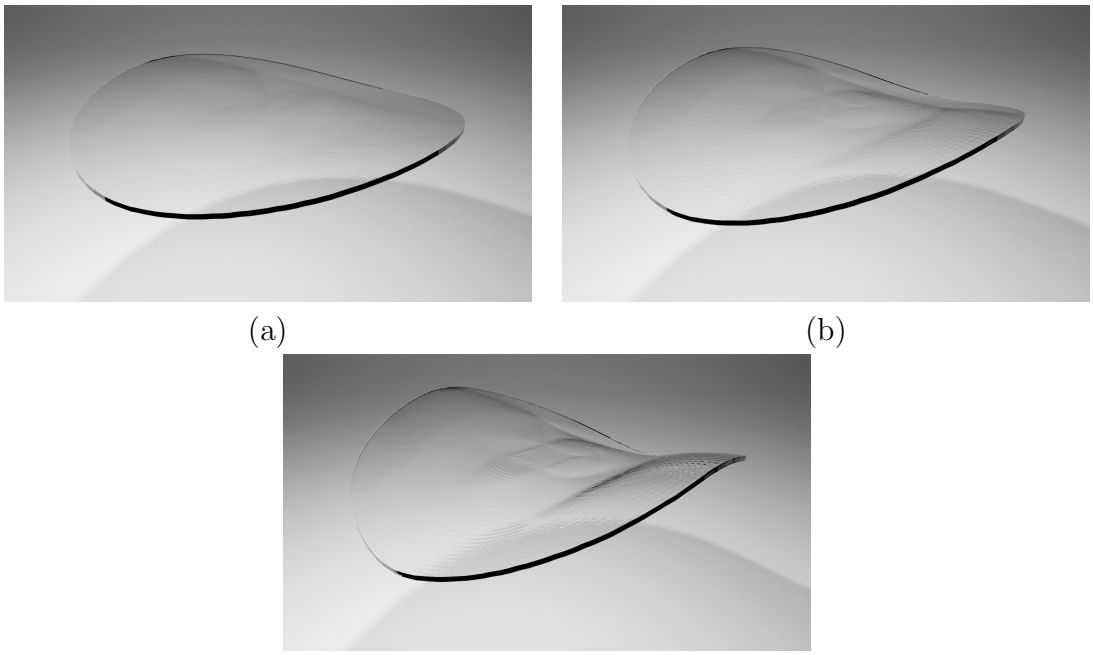

Figure 15: Example 1 (**actuation mode 1**): Evolution of the deformed configuration $\mathcal{B}$ of the optimised layer-by-layer DE device for increasing values of the voltage gradient $\Delta\varphi$ between alternating electrodes.

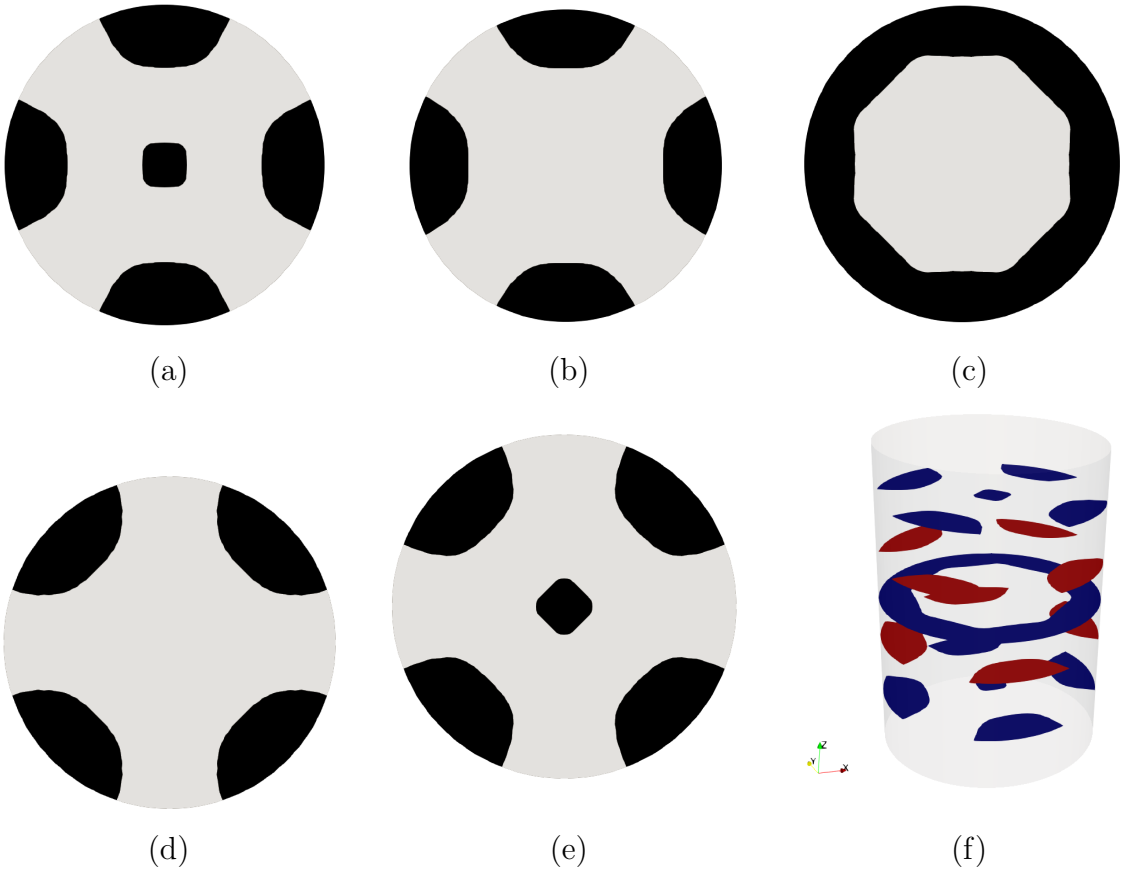

Figure 16: Example 1 (**actuation mode 2**): (a)-(e) Final distribution of the phase-field functions at final TO iteration, namely $\{\psi_{\mathcal{E}^1}(\tau_m), \ldots, \psi_{\mathcal{E}^5}(\tau_m)\}$. Black colour is associated with $\psi_{\mathcal{E}^i} = 1$ and grey colour, with $\psi_{\mathcal{E}^i} = 0$. (f) Display of layer-by-layer layout with intercalated optimal electrode distribution (a threshold value of $\psi_{\mathcal{E}^i=0.5}$ has been used) where the Z dimension of the DE device has been enlarged for visualisation purposes.

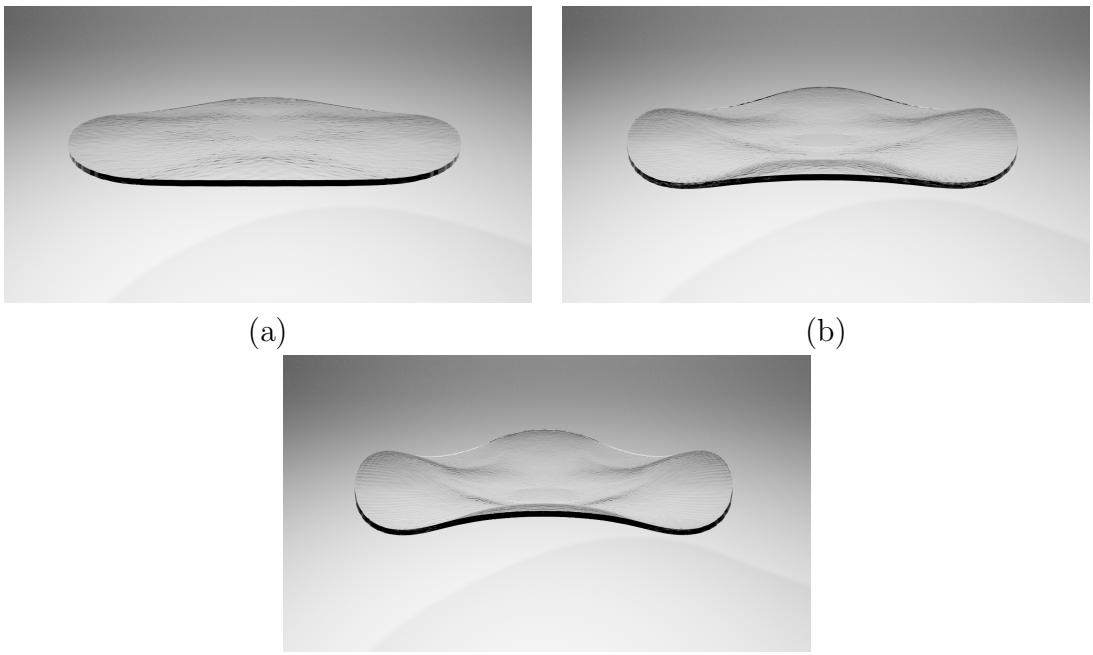

Figure 17: Example 1 (**actuation mode 2**): Evolution of the deformed configuration $\mathcal{B}$ of the optimised layer-by-layer DE device for increasing values of the voltage gradient $\Delta\varphi$ between alternating electrodes.

On the other hand, Figure 16 shows the electrode layouts for the five interfaces $\{\mathcal{E}^1, \dots, \mathcal{E}^5\}$ for **actuation mode 2**. Notice that the higher flexibility demand of this actuation mode with respect to **actuation mode 1** results in more complex topologies for the electrodes with respect to those in Figure 14. Furthermore, Figure 17 shows the deformed configuration corresponding with the optimised layout in Figure 16 under increasing electrical actuation, which is in good agreement with the objective function $\mathcal{J}(\boldsymbol{\phi})|_{\text{mode2}}$ in equation (74b).

Finally, Figure 18 displays the smooth evolution of the respective objective functions $\mathcal{J}$ for both **actuation mode 1** and **actuation mode 2** (see equation (74)) as well as various (pseudo)-time snapshots of the phase-field function at region $\mathcal{E}^1$, i.e. $\psi_{\mathcal{E}^1}$, for both DE designs. It is worth noticing the complexity of the topologies of the electrodes for both actuation modes in Figures 14 and 16, specially the latter, permitting the DE design to deform whilst attaining the desired morphological features (see Figures 15 and 17) inherent in their respective objective functions in (74). The complexity of the final electrode designs perfectly showcases this in-silico design tool as an extremely useful aid to researchers for the design of new DE designs characterised by non-intuitive electrode layouts which can permit outperform conventional DE designs.

In addition, Figure 18_{c-d} demonstrate that the final designs comply with the design hypothesis described in point **V** in Section 3. Specifically, we introduce the thresholded function $\psi^{\star}_{\mathcal{E}^i}$ defined as

$$\psi^{\star}_{\mathcal{E}^i} = \begin{cases} 1 & \psi_{\mathcal{E}^i} > 0.5 \\ 0 & \psi_{\mathcal{E}^i} \leq 0.5 \end{cases} \tag{75}$$

We then monitor the possible influence between layers $\mathcal{E}^1$ and $\mathcal{E}^4$, and also between layers $\mathcal{E}^2$ and $\mathcal{E}^5$. For that we define the following indicators

$$\mathcal{C}_{14} = \begin{cases} 1 & (\psi_{\mathcal{E}^1}, \psi_{\mathcal{E}^2}, \psi_{\mathcal{E}^3}, \psi_{\mathcal{E}^4}) = (1,0,0,1) \\ 0 & \text{otherwise} \end{cases} \qquad \mathcal{C}_{25} = \begin{cases} 1 & (\psi_{\mathcal{E}^2}, \psi_{\mathcal{E}^3}, \psi_{\mathcal{E}^4}, \psi_{\mathcal{E}^5}) = (1,0,0,1) \\ 0 & \text{otherwise} \end{cases} \tag{76}$$

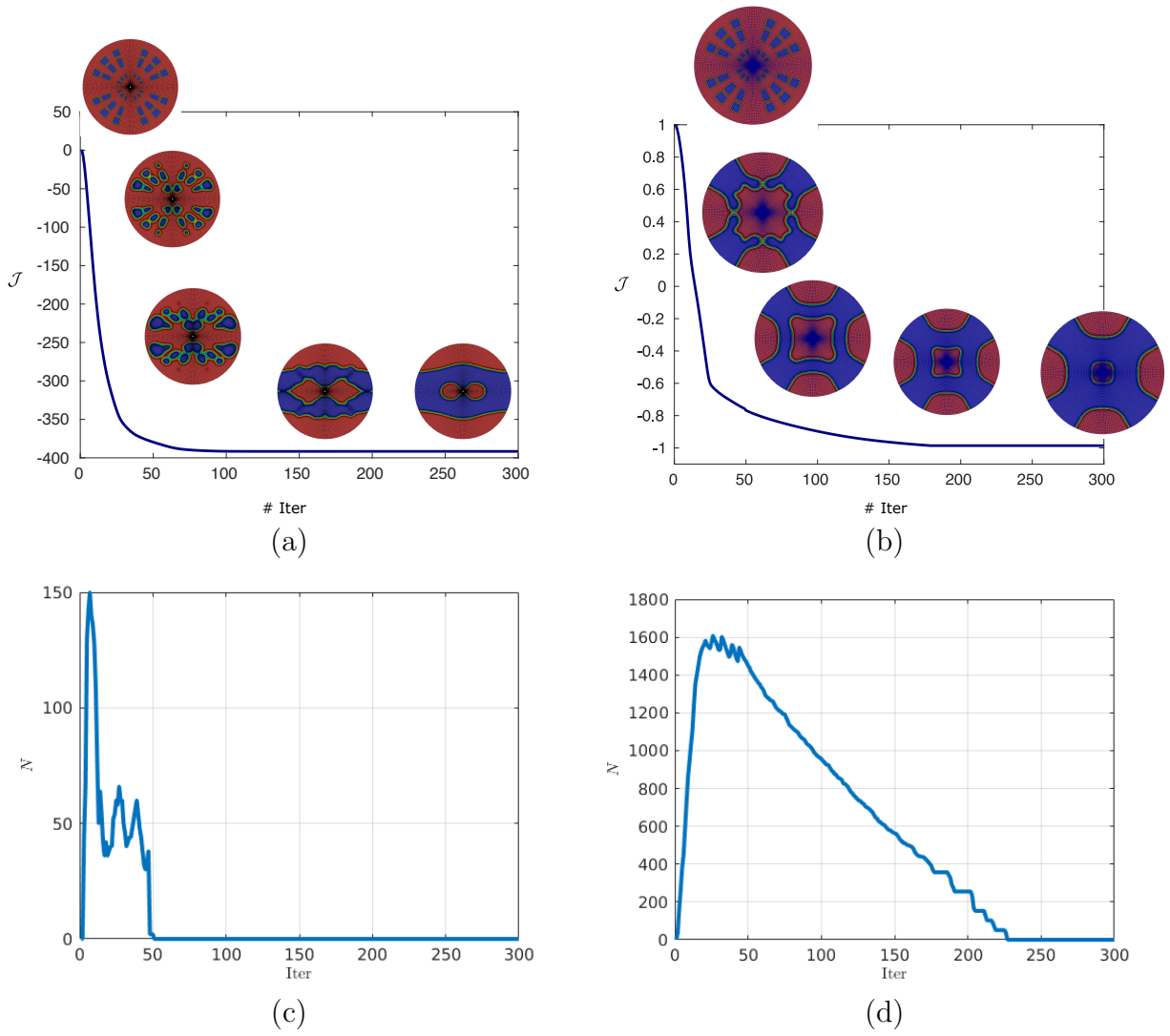

Figure 18: Example 1. Evolution of the objective function $\mathcal{J}(\boldsymbol{\phi})$ in equation (74) and of the phase-field function $\psi_{\mathcal{E}^1}(\tau)$ for (a) **actuation mode 1** and (b) **actuation mode 2** for electrode region $\mathcal{E}^1$. Number of nodes N violating the far field interaction constraint for (c) **actuation mode 1** and (d) **actuation mode 2**.

The indicator $\mathcal{C}_{14}$ adopts a value of 1 if, for the same in-plane coordinate, there exists an electrode on layer $\mathcal{E}^1$ (namely $\psi_{\mathcal{E}^1} = 1$) and there are not electrodes in layers $\mathcal{E}^2$ and $\mathcal{E}^3$ ($\psi_{\mathcal{E}^2} = 0$ and $\psi_{\mathcal{E}^3} = 0$) physically blocking an electrode in layer $\mathcal{E}^4$ (namely $\psi_{\mathcal{E}^4} = 1$). Similar interpretation can be deduced from $\mathcal{C}_{25}$. It can be seen that for both examples, as the optimisation progresses and hence, the phase-field variables $\psi_{\mathcal{E}^i}$ spatially evolve through the optimisation iterations, indicators $\mathcal{C}_{14}$ and $\mathcal{C}_{25}$ can adopt values of one at some nodes of the Finite Element mesh, and hence, the modelling assumption implied by the region of influence would not correspond with the reality, as interaction between either layers $\mathcal{E}^1$ and $\mathcal{E}^4$ or $\mathcal{E}^2$ and $\mathcal{E}^5$ occur. However, as the objective function gets stabilised, the number of nodes where $\mathcal{C}_{14}$ or $\mathcal{C}_{25}$ are 1 is zero. The underlying reason for the lack of interaction between layers which are not immediately adjacent resides in the self-penalising effect introduced by the region of influence, and specifically, by the Laplacian extension in (28). Essentially, the region of influence does not permit to detect electric field in the material whenever, for instance, there is an electrode in both layers $\mathcal{E}^1$ and $\mathcal{E}^4$ and there are not electrodes in layers $\mathcal{E}^2$ and $\mathcal{E}^3$ physically blocking it. Therefore, situations like this cannot contribute advantageously in the objective function, and hence, the final designs are devoid from situations like this.

In addition, the formulation is capable of handling any number of electrode layers $\mathcal{E}^i$, and not necessarily the 5 used in this example. In Figure 19 and 20, the designs for the case where the number of electrode layers is 3 and 7 is shown, respectively, which although not shown, yield a very similar actuated shape as that in Figure 15. The advantage though of employing a larger number of layers resides in the higher flexibility to adapt to more complex shape morphing configurations than those considered in these examples with an increasing number of electrode layers.

5.2.3. Numerical example 2

The geometry considered in this example can be observed in Figure $(21)_a$. The initial seed (at pseudo-time $\tau = 0$) for the phase-field functions, namely $\{\psi_{\mathcal{E}^1}(0), \dots, \psi_{\mathcal{E}^5}(0)\}$ at the five electrode regions $\{\mathcal{E}^1, \dots, \mathcal{E}^5\}$ is displayed in Figure $(21)_b$ (all five regions are initialised in the same manner), where the red colour is associated with a value of $\psi_{\mathcal{E}^i}(0) = 1$ (i.e. regions $\mathcal{E}^i_{\text{Elec}}(0)$) whilst the blue color is associated with $\psi_{\mathcal{E}^i}(0) = 0$ (i.e. region $\mathcal{E} \setminus \mathcal{E}^i_{\text{Elec}}(0) \cup \partial\mathcal{E}^i_{\text{Elec}}(0)$)). A $Q2$ Finite Element discretisation of the geometry in $(21)_a$ has been carried out, comprising of six layers of elements across the thickness of the DE device (Z direction) with a total of 98415 nodes for both unknown fields $\{\boldsymbol{\phi}, \varphi\}$.

As in the previous example, the objective in this example is to find the electrode layout in the five interfaces $\{\mathcal{E}^1, \dots, \mathcal{E}^5\}$ that permits the DE to deform according to two different actuation modes. Specifically, **actuation mode 1** is achieved by maximixing the vertical component (Z direction) of the displacement of the control points $\{E, G\}$, whilst minimising that of points $\{F, H\}$. Notice that this actuation mode is very similar to **actuation mode 1** on the circular geometry described in Section 5.2.2 but particularised to the square geometry in Figure 21. On the other hand, **actuation mode 2** is achieved by fixing the control points in the corners of the square geometry, and then maximising the vertical component of the displacement of control points $\{B, D\}$ and minimising that of $\{A, C\}$. In order to reproduce each actuation mode described under electrical actuation, two separate design problems have been carried out where their respective objective functions are mathematically defined as

$$\mathcal{J}(\boldsymbol{\phi})\big|_{\text{mode1}} = -\left(\boldsymbol{\phi}(\boldsymbol{X}_E) - \boldsymbol{X}_E + \boldsymbol{\phi}(\boldsymbol{X}_G) - \boldsymbol{X}_G\right) \cdot \boldsymbol{E}_3 + \left(\boldsymbol{\phi}(\boldsymbol{X}_F) - \boldsymbol{X}_F + \boldsymbol{\phi}(\boldsymbol{X}_H) - \boldsymbol{X}_H\right) \cdot \boldsymbol{E}_3; \tag{77a}$$

$$\mathcal{J}(\boldsymbol{\phi})\big|_{\text{mode2}} = -\left(\boldsymbol{\phi}(\boldsymbol{X}_B) - \boldsymbol{X}_B + \boldsymbol{\phi}(\boldsymbol{X}_D) - \boldsymbol{X}_D\right) \cdot \boldsymbol{E}_3 + \left(\boldsymbol{\phi}(\boldsymbol{X}_A) - \boldsymbol{X}_A + \boldsymbol{\phi}(\boldsymbol{X}_C) - \boldsymbol{X}_C\right) \cdot \boldsymbol{E}_3. \tag{77b}$$

Figure 22 shows the electrode layout for the five interfaces $\{\mathcal{E}^1, \dots, \mathcal{E}^5\}$ for the case of **actuation mode 1**. A more detailed view of the layer-by-layer design can be observed in Figure 22_b,

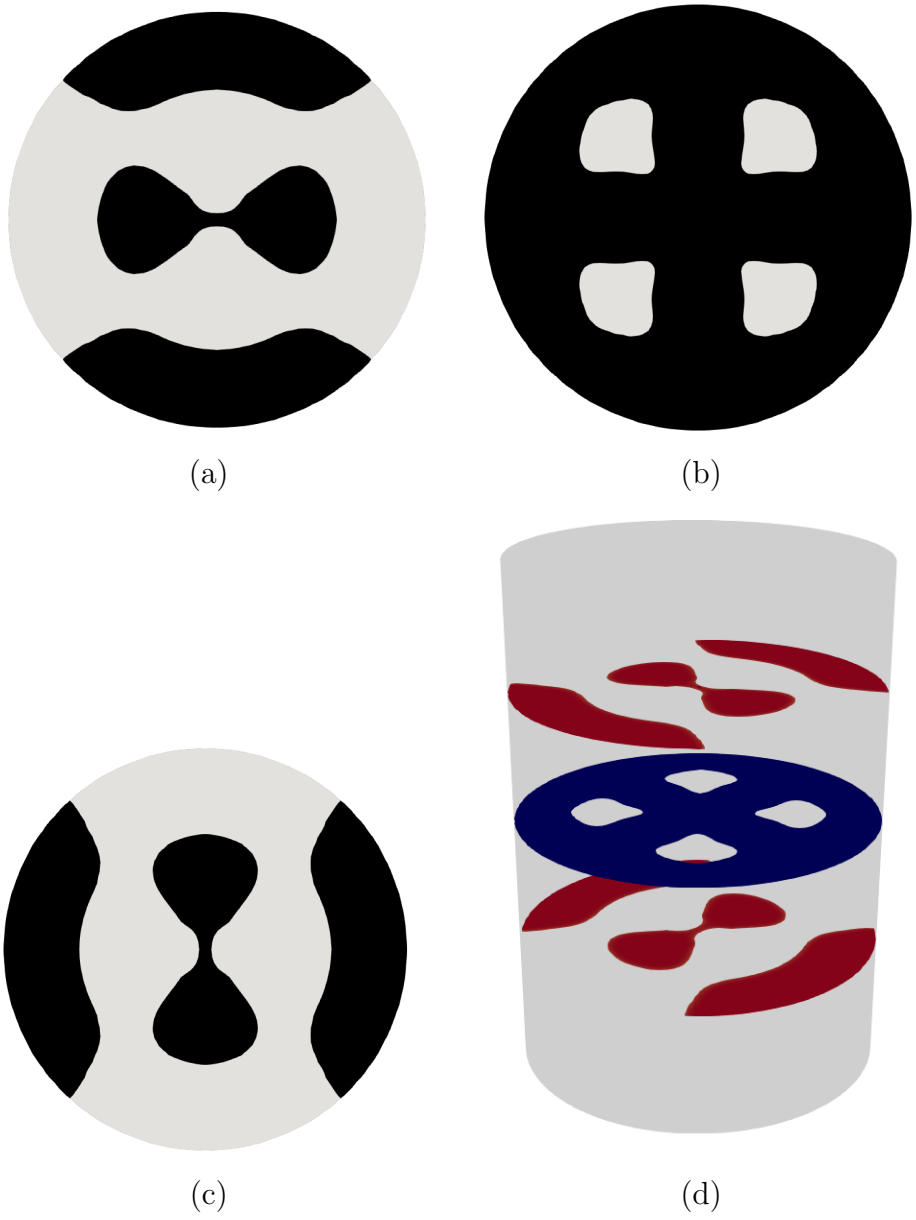

Figure 19: Example 1 (**actuation mode 1**). Final distribution of the phase-field functions at final TO iteration, namely $\{\psi_{\mathcal{E}^1}(\tau_m), \ldots, \psi_{\mathcal{E}^3}(\tau_m)\}$. Black colour is associated with $\psi_{\mathcal{E}^i} = 1$ and grey colour, with $\psi_{\mathcal{E}^i} = 0$. (f) Display of layer-by-layer layout with intercalated optimal electrode distribution (a threshold value of $\psi_{\mathcal{E}^i=0.5}$ has been used) where the Z dimension of the DE device has been enlarged for visualisation purposes.

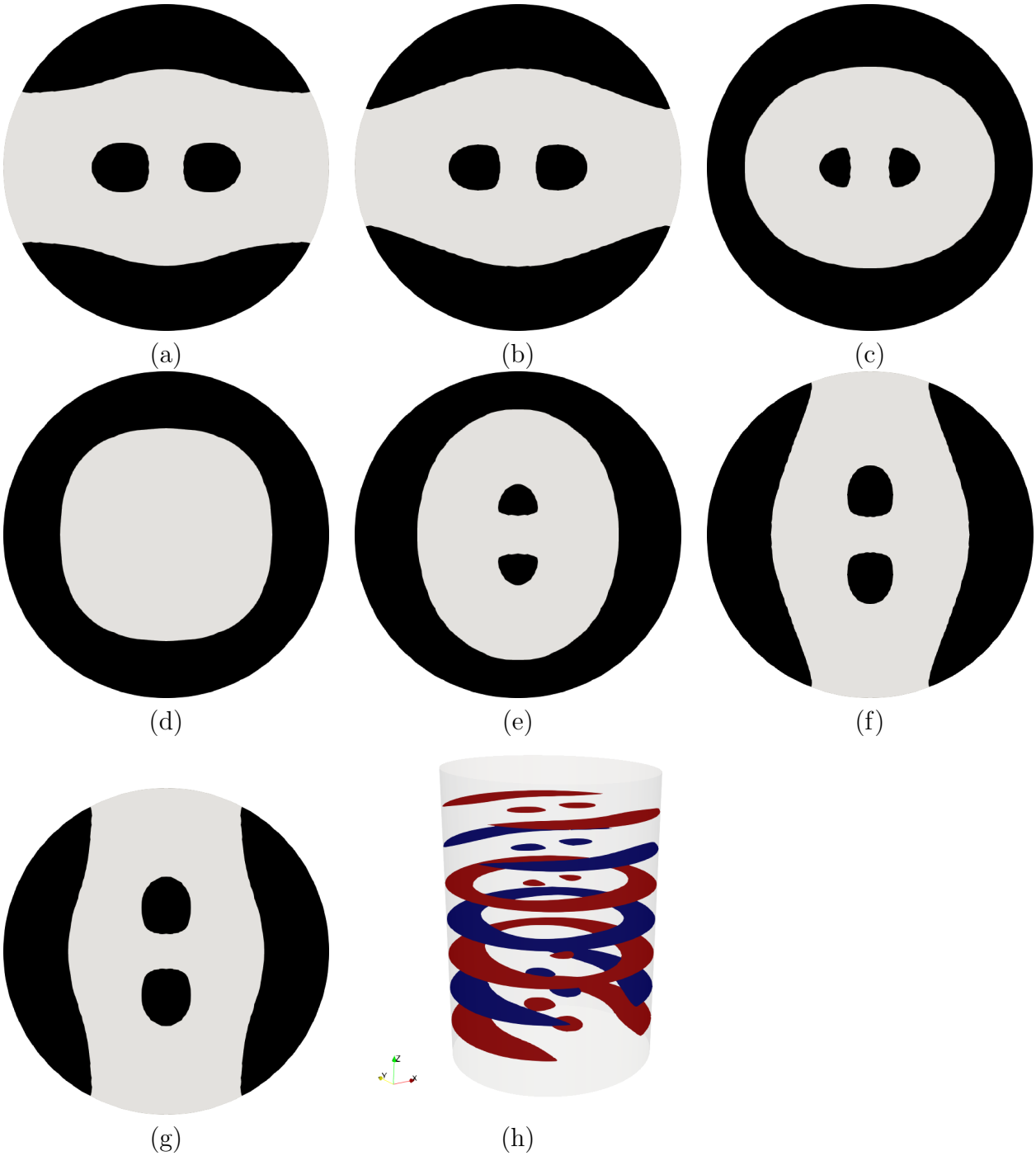

Figure 20: Example 1: Example 1 (**actuation mode 1**). Final distribution of the phase-field functions at final TO iteration, namely $\{\psi_{\mathcal{E}^1}(\tau_m), \ldots, \psi_{\mathcal{E}^7}(\tau_m)\}$. Black colour is associated with $\psi_{\mathcal{E}^i} = 1$ and grey colour, with $\psi_{\mathcal{E}^i} = 0$. (f) Display of layer-by-layer layout with intercalated optimal electrode distribution (a threshold value of $\psi_{\mathcal{E}^i=0.5}$ has been used) where the Z dimension of the DE device has been enlarged for visualisation purposes.

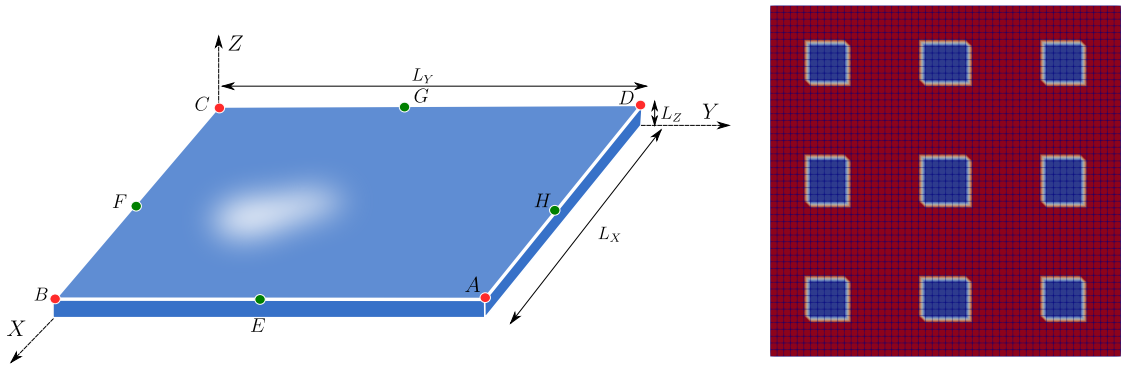

Figure 21: Example 2: (a) Geometry of the DE with $\{L_X, L_Y, L_Z\} = \{1, 1, 10^{-3}\}$ (m) and control points inducing desired actuation modes under electrical actuation; (b) Initial seed for all the phase-field functions $\{\psi_{\mathcal{E}^1}(0), \ldots, \psi_{\mathcal{E}^5}(0)\}$.

where the intercalated electrode layers are displayed in red and blue, and where the Z dimension of the device has been extruded. In addition, Figure 23 shows the deformed configuration corresponding with the optimised layout in Figure 22 under increasing electrical actuation. Clearly, the final shape of the electrically induced DE, exhibiting a saddle-point like deformation, is in agreement with the objective function $\mathcal{J}(\boldsymbol{\phi})|_{\text{mode1}}$ in equation (77a).

On the other hand, Figure 24 shows the electrode layout at the five regions $\{\mathcal{E}^1, \ldots, \mathcal{E}^5\}$ for the case of **actuation mode 2**. Notice that this actuation mode is indeed very similar to **actuation mode 1**, but the control points have been rotated 90 degrees clockwise around axis Z. Notice that in the case of a circular geometry, as that presented in the previous example in Section 5.2.2, its inherent infinite geometrical symmetry yields designs which are invariant with respect to rotations of the control points in Figure 13 around axis Z. However, the square geometry in this example, deprived from infinite circular symmetry, prevents the invariance of the optimised designs under rotations of the control points and hence, considerably different electrode designs are expected when the control points are rotated. This is corroborated from the comparison between Figures 22 and 24. In addition, Figure 25 shows the deformed configuration corresponding with the optimised layout in Figure 24 under increasing electrical actuation. Clearly, the final shape of the electrically induced DE is in agreement with the objective function $\mathcal{J}(\boldsymbol{\phi})|_{\text{mode2}}$ in equation (77b). Finally, Figure 26 displays the smooth evolution of the respective objective functions $\mathcal{J}$ for both **actuation mode 1** and **actuation mode 2** (see equation (77)) as well as various (pseudo)-time snapshots of the phase-field function at region $\mathcal{E}^1$, i.e. $\psi_{\mathcal{E}^1}$, for both DE designs.

6. Conclusions

This work has presented a novel computational methodology for the in-silico design of new electrode meso-architectures in Dielectric Elastomers (DEs). The proposed phase field topology optimisation approach is inspired in the very recent experimental work developed at Clarke Lab (Harvard) [21], where the authors put forward an original layer-by-layer layout concept for the manufacturing of DEs, where electrodes of alternating voltage are intercalated between adjacent thin elastomeric layers. The new electrode meso-architectures reported in [21] have been shown to result in extremely sophisticated actuation modes, well-beyond the current state of the art bi-morphing actuation, as exhibited by soft gripper type robots, for example.

From the design and computational standpoint, the main ingredients of the technique are as follows: (i) Consideration of the phase-field method for the implicit definition of the electrodes placed at interface regions between adjacent elastomeric layers, through the use of in-surface phase-field functions; (ii) Extension of the surface-restricted phase-field functions to the volume

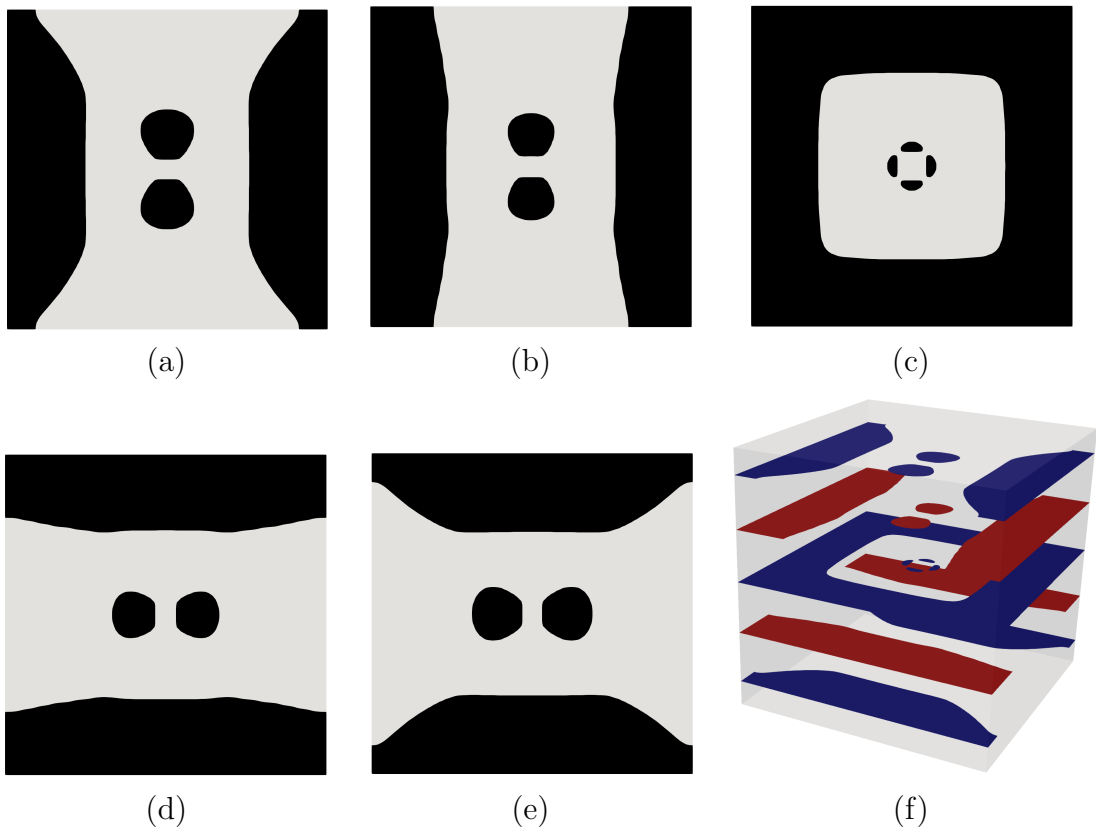

Figure 22: Example 2 (**actuation mode 1**): (a)-(e) Final distribution of the phase-field functions at final TO iteration, namely $\{\psi_{\mathcal{E}^1}(\tau_m), \ldots, \psi_{\mathcal{E}^5}(\tau_m)\}$. Black colour is associated with $\psi_{\mathcal{E}^i} = 1$ and grey colour, with $\psi_{\mathcal{E}^i} = 0$. (f) Display of layer-by-layer layout with intercalated optimal electrode distribution (a threshold value of $\psi_{\mathcal{E}^i=0.5}$ has been used) where the Z dimension of the DE device has been enlarged for visualisation purposes.

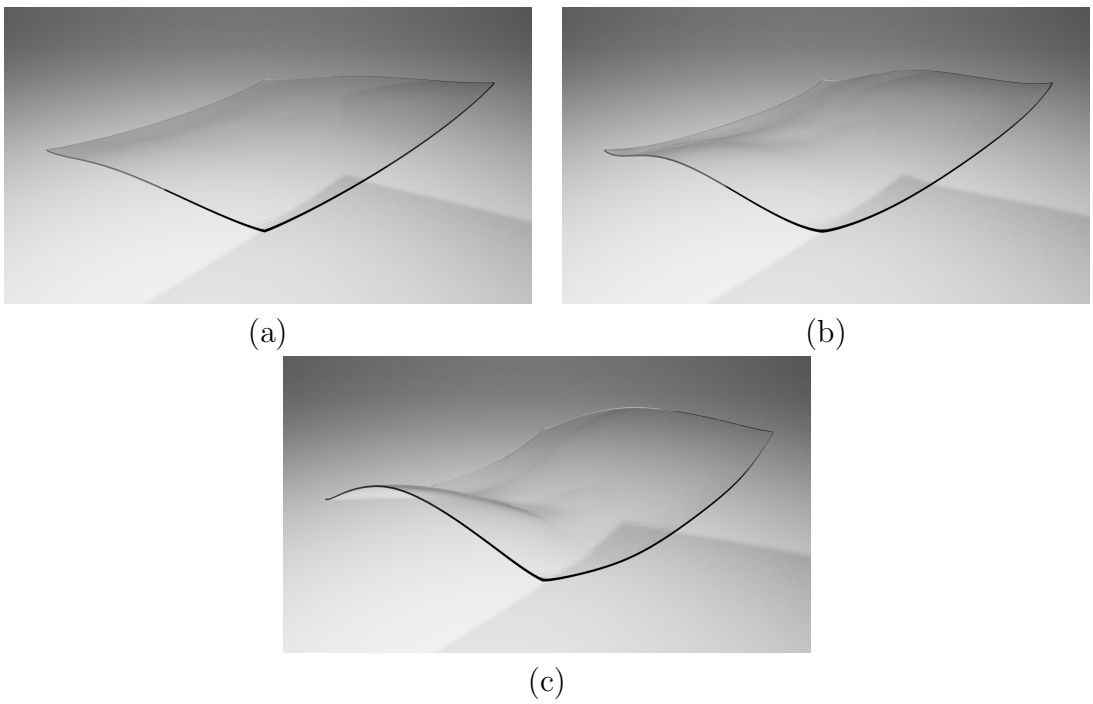

Figure 23: Example 2 (**actuation mode 1**): Evolution of the deformed configuration $\mathcal{B}$ of the optimised layer-by-layer DE device for increasing values of the voltage gradient $\Delta\varphi$ between alternating electrodes.

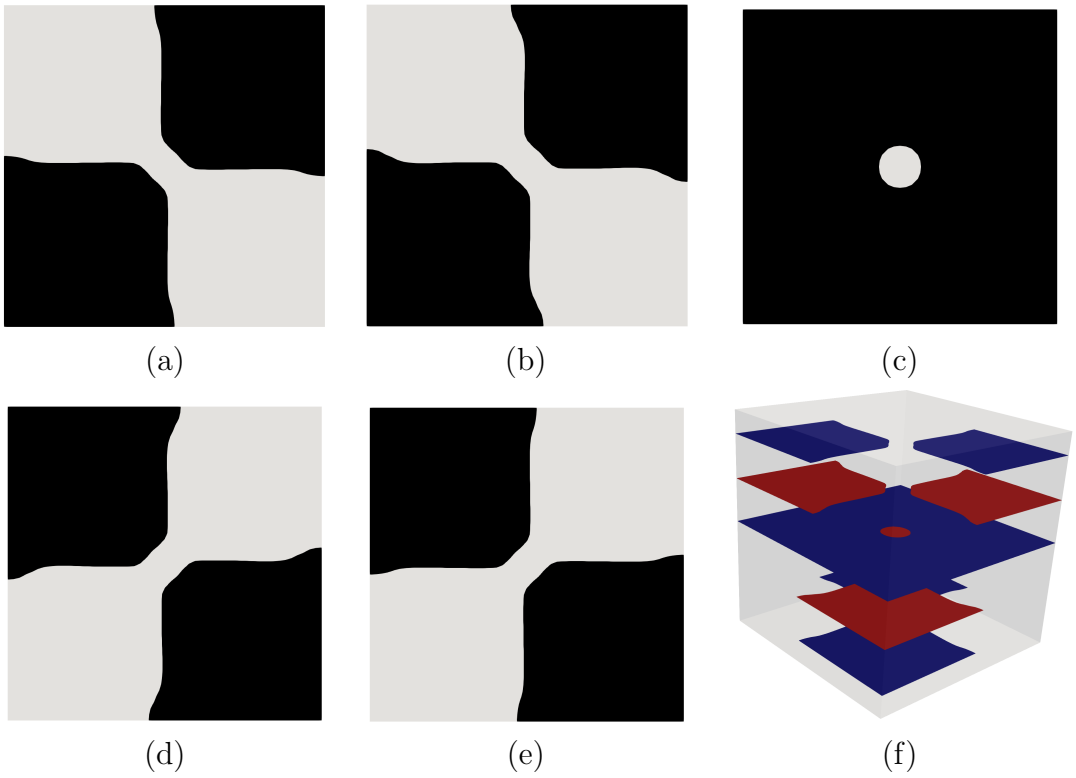

Figure 24: Example 2 (**actuation mode 2**): (a)-(e) Final distribution of the phase-field functions at final TO iteration, namely $\{\psi_{\mathcal{E}^1}(\tau_m), \ldots, \psi_{\mathcal{E}^5}(\tau_m)\}$. Black colour is associated with $\psi_{\mathcal{E}^i} = 1$ and grey colour, with $\psi_{\mathcal{E}^i} = 0$. (f) Display of layer-by-layer layout with intercalated optimal electrode distribution (a threshold value of $\psi_{\mathcal{E}^i=0.5}$ has been used) where the Z dimension of the DE device has been enlarged for visualisation purposes.

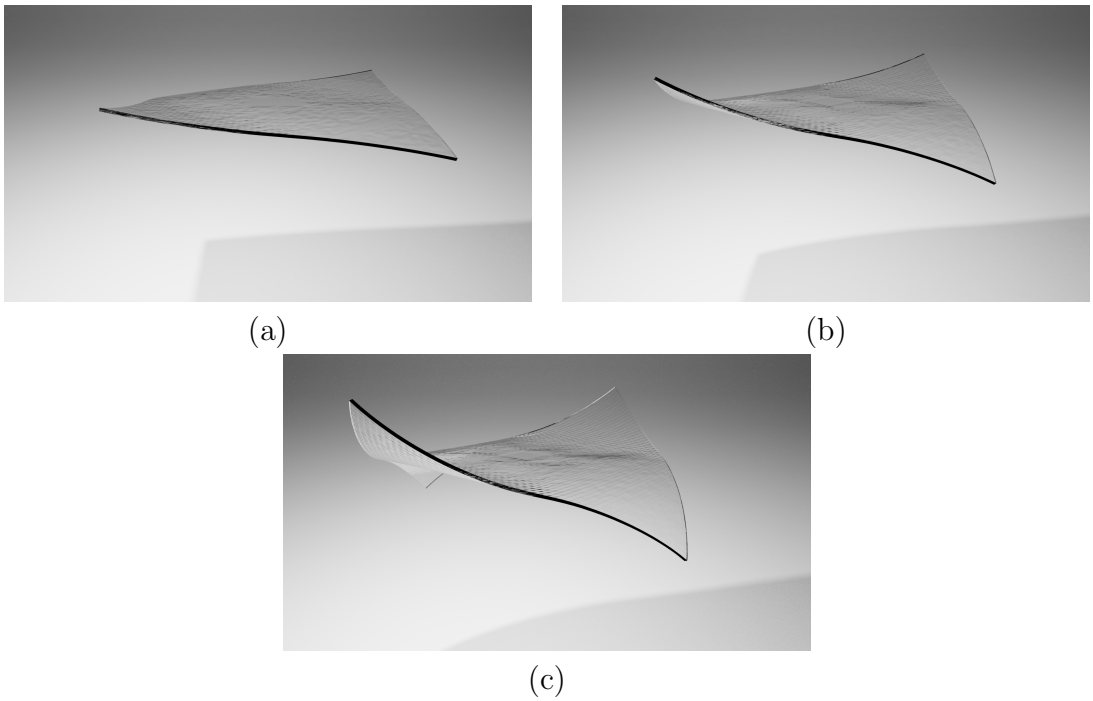

Figure 25: Example 1 (**actuation mode 1**): Evolution of the deformed configuration $\mathcal{B}$ of the optimised layer-by-layer DE device for increasing values of the voltage gradient $\Delta\varphi$ between alternating electrodes.

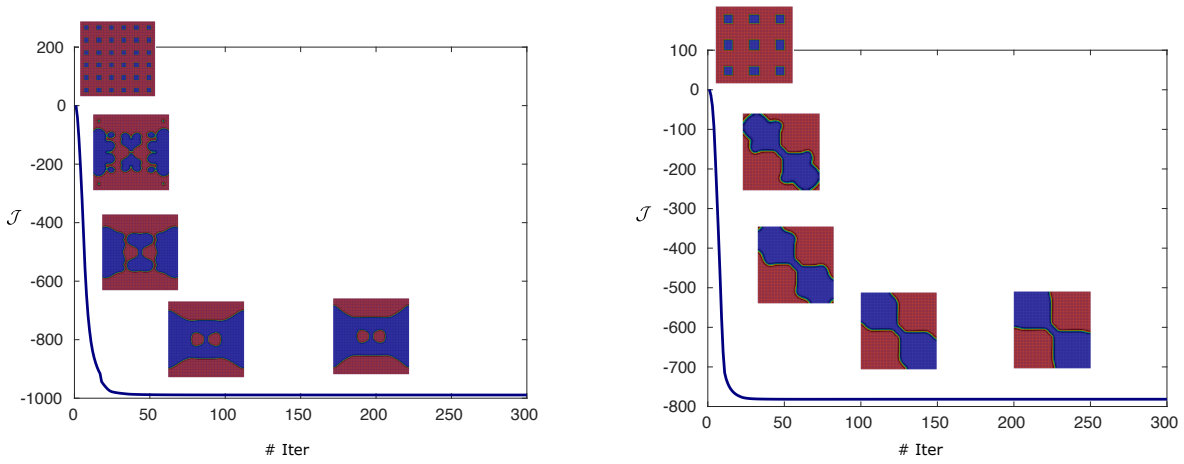

Figure 26: Example 1. Evolution of the objective function $\mathcal{J}(\boldsymbol{\phi})$ in equation (77) and of the phase-field function $\psi_{\mathcal{E}^1}(\tau)$ for (a) **actuation mode 1** and (b) **actuation mode 2** for electrode region $\mathcal{E}^1$.

of the surrounding elastomeric layers in order to incorporate the effect of the presence (or absence) of electrodes within the free energy density of the DE; (iii) Use of an original energy interpolation scheme of the free energy density where only the electromechanical contribution is affected by the extended phase-field function; (iv) Consideration of the Allen-Cahn type evolution laws proposed in Reference [60] for the surface-restricted phase-field functions, adapted to the current multiphysics electro-mechanical setting; (v) Solution of the underlying governing equations (i.e. equilibrium and Gauss' law) via a monolithic nonlinear Newton-Raphson technique.

A series of challenging proof-of-concept numerical examples are included in order to assess the applicability of the proposed methodology. As can be seen, the robustness of the computational formulation permits to explore extremely complex targeted actuation shapes, otherwise unachievable through a trial-and-error (solely) experimental based approach. Consideration of more sophisticated DE free energy density [20], incorporation of rank-n laminate constitutive models [33] or the inclusion of non-reversible rate dependent viscoelastic effects [4] constitute the next steps of our work.

Acknowledgements

The second author acknowledges the financial support of Fundación Séneca, through the contract with reference number 21132/SF/19 under the programe Subprograma Regional "Saavedra Fajardo de incorporación de doctores a Universidades y Centros de investigación de la Región de Murcia". First and second authors acknowledge the support provided by the Autonomous Community of the Region of Murcia, Spain through the programme for the development of scientific and technical research by competitive groups (20911/PI/18), included in the Regional Program for the Promotion of Scientific and Technical Research of Fundación Séneca - Agencia de Ciencia y Tecnología de la Región de Murcia. The third author acknowledges the financial support received through the European Training Network Protechtion (Project ID: 764636).

Appendix. Finite Element spatial semi-discretisation

Each elastomeric layer $\mathcal{B}_0^i$ is tessellated into a finite $|N_{\mathcal{B}_0}^i|$ set of non-overlapping volume elements and the interfaces $\mathcal{E}^i$ are tessellated into a finite $|N_{\mathcal{E}}^i|$ set of non-overlapping surface elements. In a standard Finite Element discretisation, the volume fields $\boldsymbol{\mathcal{Y}} = \{\boldsymbol{\phi}, \varphi, \boldsymbol{p}_{\boldsymbol{\phi}}, p_{\varphi}, \psi_{\mathcal{B}_0}\}$

are interpolated as

$$\boldsymbol{\phi} \approx \sum_{a=1}^{n_{\boldsymbol{\phi}}} N_a^{\boldsymbol{\phi}} \boldsymbol{\phi}^a; \quad \varphi \approx \sum_{a=1}^{n_\varphi} N_a^\varphi \varphi^a; \quad \boldsymbol{p}_{\boldsymbol{\phi}} \approx \sum_{a=1}^{n_{\boldsymbol{\phi}}} N_a^{\boldsymbol{\phi}} \boldsymbol{p}_{\boldsymbol{\phi}}^a; \quad p_\varphi \approx \sum_{a=1}^{n_\varphi} N_a^\varphi p_\varphi^a; \quad \psi_{\mathcal{B}_0} \approx \sum_{a=1}^{n_{\psi_{\mathcal{B}_0}}} N_a^{\psi_{\mathcal{B}_0}} \psi_{\mathcal{B}_0}^a, \tag{78}$$

where $N_a^{\boldsymbol{\mathcal{Y}}}$ represents the nodal shape function associated to the field $\boldsymbol{\mathcal{Y}}$ and node a of the volume discretisation, $n_{\boldsymbol{\mathcal{Y}}}$ denotes the number of nodes associated to the volume discretisation of the field $\boldsymbol{\mathcal{Y}}$, and $\boldsymbol{\mathcal{Y}}^a$ is the nodal value of the field $\boldsymbol{\mathcal{Y}}$. An identical discretisation is used for the corresponding virtual fields $\delta\boldsymbol{\mathcal{Y}}$. Notice that the same spatial discretisation is adopted for corresponding unknown fields and adjoint states. Analogously, the in-surface phase field functions are interpolated as

$$\psi_{\mathcal{E}^i} \approx \sum_{a=1}^{n_{\psi_{\mathcal{E}^i}}} N_a^{\psi_{\mathcal{E}^i}} \psi_{\mathcal{E}^i}^a, \tag{79}$$

where $N_a^{\psi_{\mathcal{E}^i}}$ represents the in-surface isoparametric shape function associated to the field $\psi_{\mathcal{E}^i}$ and node a of the in-surface discretisation, $n_{\psi_{\mathcal{E}^i}}$ denotes the number of nodes associated to the in-surface discretisation of the field $\psi_{\mathcal{E}^i}$, and $\psi_{\mathcal{E}^i}^a$ is the nodal value of the field $\psi_{\mathcal{E}^i}$. An identical discretisation is used for the corresponding virtual field $\delta\psi_{\mathcal{E}^i}$. Notice that both volume (78) and in-surface (79) discretisations are selected conforming to ensure *ab initio* C^0 continuity.

6.1. Spatial discretisation of the optimality conditions with respect to the adjoint states

The optimality conditions (56) can be spatially discretised as

$$D\Pi(\boldsymbol{\psi}_{\mathcal{B}_0}, \boldsymbol{\phi}, \varphi)[\delta\boldsymbol{p}_{\boldsymbol{\phi}}] = \sum_{a=1}^{n_{\boldsymbol{\phi}}} \delta\boldsymbol{p}_{\boldsymbol{\phi}}^a \cdot \boldsymbol{R}_a^{\boldsymbol{p}_{\boldsymbol{\phi}}} = 0; \qquad D\Pi(\boldsymbol{\psi}_{\mathcal{B}_0}, \boldsymbol{\phi}, \varphi)[\delta p_\varphi] = \sum_{a=1}^{n_\varphi} \delta p_\varphi^a R_a^{p_\varphi} = 0, \tag{80}$$

where the nodal residual components $\boldsymbol{R}_a^{\boldsymbol{p}_{\boldsymbol{\phi}}}$ and $R_a^{p_\varphi}$ are given by

$$\begin{aligned} \boldsymbol{R}_a^{\boldsymbol{p}_{\boldsymbol{\phi}}} &= \int_{\mathcal{B}_0} \boldsymbol{P}\left(\psi_{\mathcal{B}_0}, \boldsymbol{F}, \boldsymbol{E}_0\right) \boldsymbol{\nabla}_0 N_a^{\boldsymbol{\phi}} \, dV - \int_{\mathcal{B}_0} \boldsymbol{f} N_a^{\boldsymbol{\phi}} \, dV - \int_{\partial_{\boldsymbol{t}}\mathcal{B}_0} \boldsymbol{t}_0 N_a^{\boldsymbol{\phi}} \, dA; \\ R_a^{p_\varphi} &= \int_{\mathcal{B}_0} \boldsymbol{D}_0\left(\psi_{\mathcal{B}_0}, \boldsymbol{F}, \boldsymbol{E}_0\right) \cdot \boldsymbol{\nabla}_0 N_a^\varphi \, dV + \int_{\mathcal{B}_0} \rho_0 N_a^\varphi \, dV + \int_{\partial_\omega \mathcal{B}_0} \omega_0 N_a^\varphi \, dA. \end{aligned} \tag{81}$$

Solution of the discrete *nonlinear* optimality conditions (80) in terms of the nodal unknowns $\{\boldsymbol{\phi}^b, \varphi^b\}$ is carried out via the Newton-Raphson iterative strategy (50), which requires the computation of the following linearisation components

$$\begin{aligned} D^2\Pi(\boldsymbol{\psi}_{\mathcal{B}_0}, \boldsymbol{\phi}, \varphi)[\delta\boldsymbol{p}_{\boldsymbol{\phi}}; \Delta\boldsymbol{\phi}] &= \sum_{a=1}^{n_{\boldsymbol{\phi}}} \sum_{b=1}^{n_{\boldsymbol{\phi}}} \delta\boldsymbol{p}_{\boldsymbol{\phi}}^a \cdot \boldsymbol{K}_{ab}^{\boldsymbol{\phi}\boldsymbol{\phi}} \Delta\boldsymbol{\phi}^b; \\ D^2\Pi(\boldsymbol{\psi}_{\mathcal{B}_0}, \boldsymbol{\phi}, \varphi)[\delta\boldsymbol{p}_{\boldsymbol{\phi}}; \Delta\varphi] &= \sum_{a=1}^{n_{\boldsymbol{\phi}}} \sum_{b=1}^{n_\varphi} \delta\boldsymbol{p}_{\boldsymbol{\phi}}^a \cdot \boldsymbol{K}_{ab}^{\boldsymbol{\phi}\varphi} \Delta\varphi^b; \\ D^2\Pi(\boldsymbol{\psi}_{\mathcal{B}_0}, \boldsymbol{\phi}, \varphi)[\delta p_\varphi; \Delta\boldsymbol{\phi}] &= \sum_{a=1}^{n_\varphi} \sum_{b=1}^{n_{\boldsymbol{\phi}}} \delta p_\varphi^a \left(\boldsymbol{K}_{ba}^{\boldsymbol{\phi}\varphi}\right)^T \Delta\boldsymbol{\phi}^b; \\ D^2\Pi(\boldsymbol{\psi}_{\mathcal{B}_0}, \boldsymbol{\phi}, \varphi)[\delta p_\varphi; \Delta\varphi] &= \sum_{a=1}^{n_\varphi} \sum_{b=1}^{n_\varphi} \delta p_\varphi^a K_{ab}^{\varphi\varphi} \Delta\varphi^b, \end{aligned} \tag{82}$$

where the stiffness tangent contributions $\boldsymbol{K}^{\phi\phi}_{ab}$, $\boldsymbol{K}^{\phi\varphi}_{ab}$ and $\boldsymbol{K}^{\varphi\varphi}_{ab}$ can be expressed as

$$\begin{aligned}
\left(\boldsymbol{K}^{\phi\phi}_{ab}\right)_{ij} &= \int_{\mathcal{B}_0} \left(\boldsymbol{\nabla}_0 N^{\phi}_a\right)_I \left(\boldsymbol{\mathcal{C}}\left(\psi_{\mathcal{B}_0}, \boldsymbol{F}, \boldsymbol{E}_0\right)\right)_{iIjJ} \left(\boldsymbol{\nabla}_0 N^{\phi}_b\right)_J dV; \\
\left(\boldsymbol{K}^{\phi\varphi}_{ab}\right)_{i} &= \int_{\mathcal{B}_0} \left(\boldsymbol{\nabla}_0 N^{\phi}_a\right)_I \left(\boldsymbol{\mathcal{P}}^T\left(\psi_{\mathcal{B}_0}, \boldsymbol{F}, \boldsymbol{E}_0\right)\right)_{iIJ} \left(\boldsymbol{\nabla}_0 N^{\varphi}_b\right)_J dV; \\
K^{\varphi\varphi}_{ab} &= -\int_{\mathcal{B}_0} \boldsymbol{\nabla}_0 N^{\varphi}_a \cdot \boldsymbol{\varepsilon}\left(\psi_{\mathcal{B}_0}, \boldsymbol{F}, \boldsymbol{E}_0\right) \boldsymbol{\nabla}_0 N^{\varphi}_b \, dV.
\end{aligned} \tag{83}$$

6.2. Spatial discretisation of the optimality conditions with respect to the unknown fields

Spatial discretisation of the optimality conditions (57) yield the following *linear* system of equations in terms of the nodal unknowns $\{\boldsymbol{p}^b_{\boldsymbol{\phi}}, p^b_{\varphi}\}$ as

$$D\mathcal{L}(\boldsymbol{\psi}_{\mathcal{B}_0}, \boldsymbol{\mathcal{U}}, \boldsymbol{p}_{\boldsymbol{\mathcal{U}}})[\delta\boldsymbol{\phi}] = -\sum_{a=1}^{n_{\boldsymbol{\phi}}}\sum_{b=1}^{n_{\boldsymbol{\phi}}} \delta\boldsymbol{\phi}^a \cdot \boldsymbol{K}^{\phi\phi}_{ab}\boldsymbol{p}^b_{\boldsymbol{\phi}} - \sum_{a=1}^{n_{\boldsymbol{\phi}}}\sum_{b=1}^{n_{\varphi}} \delta\boldsymbol{\phi}^a \cdot \boldsymbol{K}^{\phi\varphi}_{ab} p^b_{\varphi} + \sum_{a=1}^{n_{\boldsymbol{\phi}}} \delta\boldsymbol{\phi}_a \cdot \boldsymbol{R}^{\mathcal{J}}_a = 0; \tag{84a}$$

$$D\mathcal{L}(\boldsymbol{\psi}_{\mathcal{B}_0}, \boldsymbol{\mathcal{U}}, \boldsymbol{p}_{\boldsymbol{\mathcal{U}}})[\delta\varphi] = -\sum_{a=1}^{n_{\varphi}}\sum_{b=1}^{n_{\boldsymbol{\phi}}} \delta\varphi^a \left(\boldsymbol{K}^{\phi\varphi}_{ba}\right)^T \boldsymbol{p}^b_{\boldsymbol{\phi}} - \sum_{a=1}^{n_{\varphi}}\sum_{b=1}^{n_{\varphi}} \delta\varphi^a K^{\varphi\varphi}_{ab} p^b_{\varphi} = 0, \tag{84b}$$

where, for the particular case of the objective function in (52), the residual vector $\boldsymbol{R}^{\mathcal{J}}_a$ corresponding to the discretisation of $D\mathcal{J}(\boldsymbol{\phi})[\delta\boldsymbol{\phi}]$ yields

$$\boldsymbol{R}^{\mathcal{J}}_a = \omega_{aI}\boldsymbol{E}_3; \qquad \omega_{aI} = \begin{cases} \delta_{aI}; & I = \{A, B, C, D\}; \\ -\delta_{aI}; & I = \{E, F, G, H\}, \end{cases} \tag{85}$$

and δ_{aI} is the delta Kronecker operator and $\boldsymbol{E}_3 = [0\ 0\ 1]^T$.

6.3. Spatial discretisation of the phase field volume extension

The spatial discretisation of (30) yields the following linear system of algebraic equations

$$D\Lambda(\boldsymbol{\psi}_{\mathcal{E}}, \psi_{\mathcal{B}_0})[\delta\psi_{\mathcal{B}_0}] = \sum_{a=1}^{n_{\psi_{\mathcal{B}_0}}}\sum_{b=1}^{n_{\psi_{\mathcal{B}_0}}} \delta\psi^a_{\mathcal{B}_0} K^{\psi_{\mathcal{B}_0}\psi_{\mathcal{B}_0}}_{ab} \psi^b_{\mathcal{B}_0} = 0; \qquad K^{\boldsymbol{\psi}_{\mathcal{B}_0}\boldsymbol{\psi}_{\mathcal{B}_0}}_{ab} = \int_{\mathcal{B}_0} \boldsymbol{\nabla}_0 N^{\psi_{\mathcal{B}_0}}_a \cdot \boldsymbol{\nabla}_0 N^{\psi_{\mathcal{B}_0}}_b \, dV. \tag{86}$$

Standard vector and matrix assembly of the system (86) and a convenient re-ordering of the nodal values $\psi^b_{\mathcal{B}_0}$, splitting these between n_f *true free degrees of freedom* (those to be determined from the solution of (86), compactly denoted as $\boldsymbol{\psi}^f_{\mathcal{B}_0}$) and n_p *prescribed values* (compactly denoted as $\boldsymbol{\psi}^p_{\mathcal{B}_0}$, with $\boldsymbol{\psi}^p_{\mathcal{B}_0} = \boldsymbol{\psi}_{\mathcal{E}}$) can be carried in order to re-write (86) as

$$\begin{bmatrix} \boldsymbol{K}^{\psi_{\mathcal{B}_0}\psi_{\mathcal{B}_0}}_{ff} & \boldsymbol{K}^{\psi_{\mathcal{B}_0}\psi_{\mathcal{B}_0}}_{fp} \\ \left(\boldsymbol{K}^{\psi_{\mathcal{B}_0}\psi_{\mathcal{B}_0}}_{fp}\right)^T & \boldsymbol{K}^{\psi_{\mathcal{B}_0}\psi_{\mathcal{B}_0}}_{pp} \end{bmatrix} \begin{bmatrix} \boldsymbol{\psi}^f_{\mathcal{B}_0} \\ \boldsymbol{\psi}^p_{\mathcal{B}_0} \end{bmatrix} = \boldsymbol{0}; \qquad \boldsymbol{\psi}^p_{\mathcal{B}_0} = \boldsymbol{\psi}_{\mathcal{E}}. \tag{87}$$

Following the solution of above system (87), permits to obtain

$$\frac{\partial\boldsymbol{\psi}^f_{\mathcal{B}_0}}{\partial\boldsymbol{\psi}_{\mathcal{E}}} = -\left(\boldsymbol{K}^{\psi_{\mathcal{B}_0}\psi_{\mathcal{B}_0}}_{ff}\right)^{-1} \boldsymbol{K}^{\psi_{\mathcal{B}_0}\psi_{\mathcal{B}_0}}_{fp}; \qquad \frac{\partial\boldsymbol{\psi}^p_{\mathcal{B}_0}}{\partial\boldsymbol{\psi}_{\mathcal{E}}} = \boldsymbol{I}_{n_p\times n_p}, \tag{88}$$

which is a key ingredient in the computation of the sensitivity (61).

6.4. Computation of the sensitivity and evolution of the phase field equation

Spatial discretisation of (61) leads to

$$D\mathcal{F}(\boldsymbol{\psi}_{\mathcal{E}})[\Delta\psi_{\mathcal{E}^i}] = \sum_{a=1}^{n_{\psi_{\mathcal{E}^i}}} \partial_{\psi_{\mathcal{E}^i}}\mathcal{F}_a \, \Delta\psi_{\mathcal{E}^i}^a; \qquad \partial_{\psi_{\mathcal{E}^i}}\mathcal{F}_a = -\sum_{b=1}^{n_{\psi_{\mathcal{B}_0}}} \left(\int_{\mathcal{B}_0} g(\boldsymbol{X}, \psi_{\mathcal{B}_0}) N_b^{\psi_{\mathcal{B}_0}} \, dV \right) \frac{\partial \psi_{\mathcal{B}_0}^b}{\partial \psi_{\mathcal{E}^i}^a}, \quad (89)$$

which defines the so-called nodal sensitivity, which can be compactly written in a vector format as $\partial_{\psi_{\mathcal{E}^i}}\boldsymbol{\mathcal{F}} = [\partial_{\psi_{\mathcal{E}^i}}\mathcal{F}_1 \dots \partial_{\psi_{\mathcal{E}^i}}\mathcal{F}_{n_{\psi_{\mathcal{B}_0}}}]^T$. This sensitivity can be used to drive the in-surface phase field evolution equation via the scalar field $\mathcal{G}_{\mathcal{E}^i}$ used in (68), which is defined as

$$\mathcal{G}_{\mathcal{E}^i} = \frac{1}{\|\partial_{\psi_{\mathcal{E}^i}}\boldsymbol{\mathcal{F}}\|} \sum_{a=1}^{n_{\psi_{\mathcal{E}^i}}} N_a^{\psi_{\mathcal{E}^i}} \partial_{\psi_{\mathcal{E}^i}}\mathcal{F}_a, \quad (90)$$

where $\partial_{\psi_{\mathcal{E}^i}}\boldsymbol{\mathcal{F}}$ is defined as the L_2 norm of the sensitivity over the surface $\mathcal{E}^i$. Notice that the L_2 norm featuring in above equation (90) is simply introduce to non-dimensionalise the sensitivity term. The spatial discretisation of the phase field evolution equation (69) yields

$$\sum_{a=1}^{n_{\psi_{\mathcal{E}^i}}} \sum_{b=1}^{n_{\psi_{\mathcal{E}^i}}} \delta\psi_{\mathcal{E}^i}^a K_{ab}^{\psi_{\mathcal{E}^i}\psi_{\mathcal{E}^i}} \Delta\psi_{\mathcal{E}^i}^b = \sum_{a=1}^{n_{\psi_{\mathcal{E}^i}}} \delta\psi_{\mathcal{E}^i}^a R_a^{\psi_{\mathcal{E}^i}}, \quad (91)$$

where the stiffness matrix component $K_{ab}^{\psi_{\mathcal{E}^i}\psi_{\mathcal{E}^i}}$ and the residual component $R_a^{\psi_{\mathcal{E}^i}}$ are expressed as

$$K_{ab}^{\psi_{\mathcal{E}^i}\psi_{\mathcal{E}^i}} = \int_{\mathcal{E}^i} \left(\frac{1}{\Delta\tau} N_{\psi_{\mathcal{E}^i}}^a N_{\psi_{\mathcal{E}^i}}^b + \kappa \boldsymbol{\nabla}_0 N_{\psi_{\mathcal{E}^i}}^a \cdot \boldsymbol{\nabla}_0 N_{\psi_{\mathcal{E}^i}}^b + N_{\psi_{\mathcal{E}^i}}^a N_{\psi_{\mathcal{E}^i}}^b P(\psi_{\mathcal{E}^i}^n) r(\boldsymbol{\xi}, \psi_{\mathcal{E}^i}^n) \right) dA, \quad (92)$$

and

$$R_a^{\psi_{\mathcal{E}^i}} = \int_{\mathcal{E}^i} \left(\frac{\psi_{\mathcal{E}^i}^n}{\Delta\tau} + Q(\psi_{\mathcal{E}^i}^n) r(\boldsymbol{\xi}, \psi_{\mathcal{E}^i}^n) \right) N_{\psi_{\mathcal{E}^i}}^a \, dA, \quad (93)$$

where

$$P(\psi_{\mathcal{E}^i}^n) = \begin{cases} (\psi_{\mathcal{E}^i}^n - 1); & \text{if } r(\boldsymbol{\xi}, \psi_{\mathcal{E}^i}^n) \leq 0; \\ \psi_{\mathcal{E}^i}^n; & \text{if } r(\boldsymbol{\xi}, \psi_{\mathcal{E}^i}^n) > 0; \end{cases} \qquad Q(\psi_{\mathcal{E}^i}^n) = \begin{cases} 0; & \text{if } r(\boldsymbol{\xi}, \psi_{\mathcal{E}^i}^n) \leq 0; \\ \psi_{\mathcal{E}^i}^n; & \text{if } r(\boldsymbol{\xi}, \psi_{\mathcal{E}^i}^n) > 0. \end{cases} \quad (94)$$

Appendix. Numerical comparison between sharp and diffuse interface approaches

In this appendix, a comparison of the diffuse interface approach against the sharp interface approach is carried out for the designs presented in examples 5.2.1 and 5.2.2. The squared geometry examples in Sections 5.2.3 are not included here, as they lead to the same conclusion.

In order to construct the sharp interface model, every Finite Element node at each surface region $\mathcal{E}^i$, $i = \{1, \dots, N^{L-1}\}$ associated with a value of $\psi_{\mathcal{E}^i}$ such that $\psi_{\mathcal{E}^i} \geq 0.5$ is treated as a Dirichlet boundary condition for the electric potential, yielding a sharp geometrical approximation of the boundary of the electrodes. Figure 27 shows the contour plot of the norm of the displacement field obtained for the various optimal electrode topologies. The agreement between both sharp and diffuse interface approaches is extremely good in terms of this metric.

An additional field which provides interesting insight is the Lagrangian electric field $\boldsymbol{E}_0 = -\boldsymbol{\nabla}_0\varphi$. Notice that the diffuse approach, which considers a uniform distribution of electric potential along each surface $\mathcal{E}^i$, yields therefore a uniform distribution of $\boldsymbol{E}_0$ on each volume layer $\mathcal{B}_0^i$. Here is where the energy interpolation scheme in equation (33) which, when particularised to

the case of an ideal dielectric elastomer (see equation (8)), permits to define the so called effective electric field as,

$$\begin{aligned}\bar{\Psi}_{em}(\psi_{\mathcal{B}_0}(\boldsymbol{X},\boldsymbol{\psi}_{\mathcal{E}}),\boldsymbol{F},\boldsymbol{E}_0) &= \left[(\psi_{\mathcal{B}_0}(\boldsymbol{X},\boldsymbol{\psi}_{\mathcal{E}}))^p+\alpha\right]\Psi_{em}(\boldsymbol{F},\boldsymbol{E}_0)\\ &= -\left[(\psi_{\mathcal{B}_0}(\boldsymbol{X},\boldsymbol{\psi}_{\mathcal{E}}))^p+\alpha\right]\frac{\varepsilon_r\varepsilon_0}{2J}\boldsymbol{H}\boldsymbol{E}_0\cdot\boldsymbol{H}\boldsymbol{E}_0\\ &= -\frac{\varepsilon_r\varepsilon_0}{2J}\boldsymbol{H}\hat{\boldsymbol{E}}_0\cdot\boldsymbol{H}\hat{\boldsymbol{E}}_0,\end{aligned} \tag{95}$$

with $\hat{\boldsymbol{E}}_0$ the effective electric field, defined as,

$$\hat{\boldsymbol{E}}_0 = \sqrt{\left[(\psi_{\mathcal{B}_0}(\boldsymbol{X},\boldsymbol{\psi}_{\mathcal{E}}))^p+\alpha\right]}\boldsymbol{E}_0. \tag{96}$$

The field responsible for the deformation of the dielectric material in the case of the smooth interface approach is indeed $\hat{\boldsymbol{E}}_0$, as it features quadratically in the electro-mechanical contribution of the first Piola-Kirchhoff stress tensor. Therefore, comparison of this field inferred from the smooth approach against the true electric field yielded by the geometrically sharp approach is a good indicator of the accuracy of the first. This comparison is carried out in Figure 28 (notice that the thickness of the DE device has been increased by a factor of 5 for visualisation purposes). Clearly, there is an excellent agreement between both the true electric field distribution $\boldsymbol{E}_0$ for the sharp interface approach and the effective electric field $\hat{\boldsymbol{E}}_0$ for the smooth interface approach. Naturally, the first approach yields a more realistic representation of the electric field (including border effects on the boundaries of the electrodes). However, these features (namely border effects) have proven not to be sufficiently relevant as to yield differences in the electrically induced deformations between both approaches.

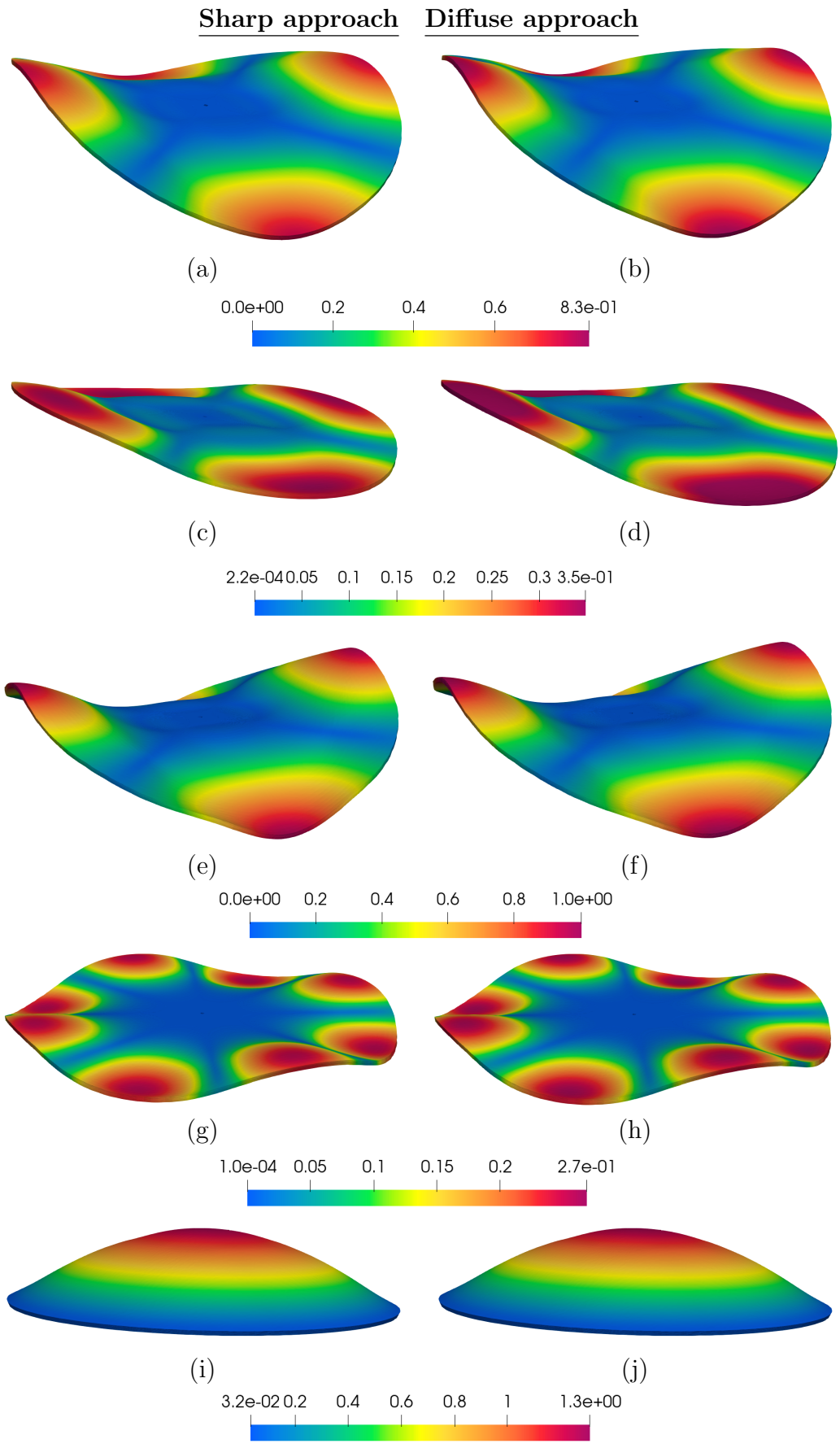

Figure 27: Contour plot distribution of the norm of the displacement field when considering the geometrically sharp interface approach (left column) and the diffuse approach (right column) pursued in this paper. Results corresponding with examples: (a)-(b) Actuation mode 1 in Section 5.2.2 with five electrode regions; (c)-(d) Actuation mode 1 in Section 5.2.2 with three electrode regions; (e)-(f) Actuation mode 1 in Section 5.2.2 with seven electrode regions; (g)-(h) Actuation mode 2 in Section 5.2.2; (i)-(j) Example in Section 5.2.1.

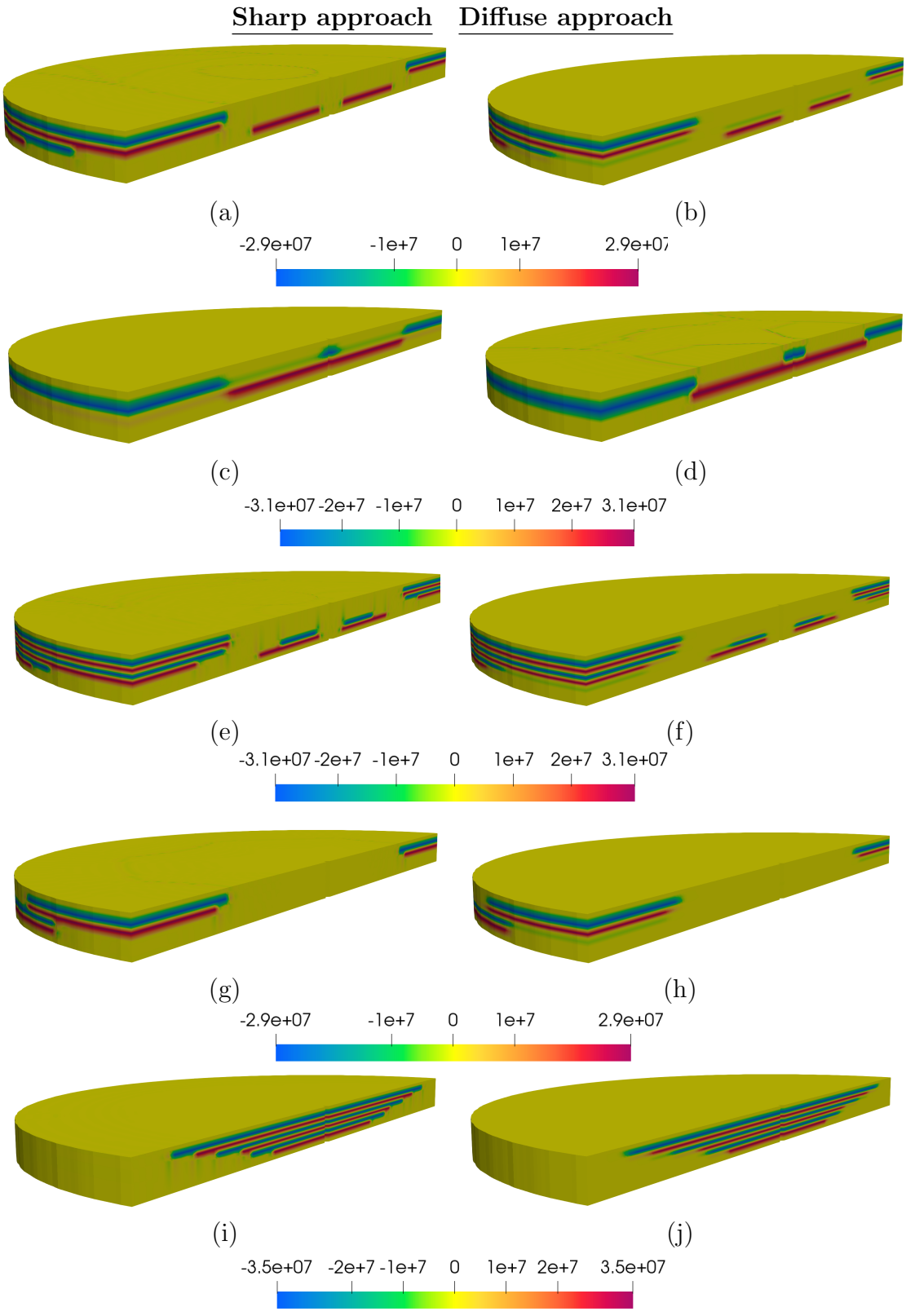

Figure 28: Contour plot distribution of the true Lagrangian electric field $\boldsymbol{E}_0$ when considering the geometrically sharp interface approach (left column). Contour plot distribution of the effective Lagrangian electric field $\hat{\boldsymbol{E}}_0$ in (96) when considering the smooth interface approach pursued in this paper (right column). For visualisation purposes, the thickness has been increased by a factor of 5, and the results have been plotted in the undeformed configuration. Results corresponding with examples: (a)-(b) Actuation mode 1 in Section 5.2.2 with five electrode regions; (c)-(d) Actuation mode 1 in Section 5.2.2 with three electrode regions; (e)-(f) Actuation mode 1 in Section 5.2.2 with seven electrode regions; (g)-(h) Actuation mode 2 in Section 5.2.2; (i)-(j) Example in Section 5.2.1.

References

[1] N. Aage, E. Andreassen, B.S. Lazarov, and O. Sigmund. Giga-voxel computational morphogenesis for structural design. *Nature*, 550:84–86, 2017.

[2] G. Allaire, F. Jouve, and Toader. A. Structural optimization using sensitivity analysis and a level-set method. *Journal of Computational Physics*, 194:363–393, 2004.

[3] M. P. Bendsøe and O. Sigmund. *Topology optimization*. Springer-Verlag, Berlin, 2003. Theory, methods and applications.

[4] Dana Bishara and Mahmood Jabareen. A reduced mixed finite-element formulation for modeling the viscoelastic response of electro-active polymers at finite deformation. *Mathematics and Mechanics of Solids*, 24(5):1578–1610, 2019.

[5] J. Bonet, A. J. Gil, C. H. Lee, M. Aguirre, and R. Ortigosa. A first order hyperbolic framework for large strain computational solid dynamics - Part I: Total Lagrangian isothermal elasticity. *Computer Methods in Applied Mechanics and Engineering*, 283(0):689–732, 2015.

[6] J. Bonet, A. J. Gil, and R. Ortigosa. A computational framework for polyconvex large strain elasticity. *Computer Methods in Applied Mechanics and Engineering*, 283:1061–1094, 2015.

[7] J. Bonet, A. J. Gil, and R. Ortigosa. On a tensor cross product based formulation of large strain solid mechanics. *International Journal of Solids and Structures*, 84:49–63, 2016.

[8] J. Bonet, A. J. Gil, and R. D. Wood. *Nonlinear Continuum Mechanics for Finite Element Analysis: Statics*. Cambridge University Press, 2016.

[9] E. Bortot, O. Amir, and G. Shmuel. Topology optimization of dielectric elastomers for wide tunable band gaps. *International Journal of Solids and Structures*, 143:262 – 273, 2018.

[10] M. Burger and R. Stainko. Phase-field relaxation of topology optimization with local stress constraints. *SIAM Journal on Control and Optimisation*, 192:147–1466, 2003.

[11] R. Bustamante, A. Dorfmann, and R.W. Ogden. On electric body forces and Maxwell stresses in nonlinearly electroelastic solids. *International Journal of Engineering Science*, 47(11-12):1131–1141, 2009.

[12] R. Bustamante and J. Merodio. Constitutive structure in coupled non-linear electroelasticity: Invariant descriptions and constitutive restrictions. *International Journal of Non-Linear Mechanics*, 46(10):1315 – 1323, 2011.

[13] F. Chen and M. Y. Wang. Design optimization of soft robots: A review of the state of the art. *IEEE Robotics Automation Magazine*, 27(4):27–43, 2020.

[14] Feifei Chen, Kun Liu, Yiqiang Wang, Jiang Zou, Guoying Gu, and Xiangyang Zhu. Automatic design of soft dielectric elastomer actuators with optimal spatial electric fields. *IEEE Transactions on Robotics*, 35(5):1150–1165, 2019.

[15] L. Chen, X. Yang, B. Wang, S. Yang, K. Dayal, and P. Sharma. The interplay between symmetry-breaking and symmetry-preserving bifurcations in soft dielectric films and the emergence of giant electro-actuation. *Extreme Mechanics Letters*, 43:101151, 2021.

[16] A. Donoso and J. Bellido. Systematic design of distributed piezoelectric modal sensors/actuators for rectangular plates by optimizing the polarization profile. *Structural and Multidisciplinary Optimization*, 38:347–356, 2009.

[17] A. Donoso, J. Bellido, and J. Chacón. Numerical and analytical method for the design of piezoelectric modal sensors/actuators for shell-type structures. *International Journal for Numerical Methods in Engineering*, 81:1700 – 1712, 2009.

[18] A. Dorfmann and R. W. Ogden. Nonlinear electroelasticity. *Acta Mechanica*, 174(3-4):167–183, 2005.

[19] A. Dorfmann and R.W. Ogden. Nonlinear electroelastic deformations. *Journal of Elasticity*, 82(2):99–127, 2006.

[20] A. J. Gil and R. Ortigosa. A new framework for large strain electromechanics based on convex multi-variable strain energies: variational formulation and material characterisation. *Computer Methods in Applied Mechanics and Engineering*, 302:293–328, 2016.

[21] E. Hajiesmaili and D.R. Clarke. Reconfigurable shape-morphing dielectric elastomers using spatially varying electric fields. *Nature Communicationes*, 10(183):1–7, 2019.

[22] David L. Henann, Shawn A. Chester, and Katia Bertoldi. Modeling of dielectric elastomers: Design of actuators and energy harvesting devices. *Journal of the Mechanics and Physics of Solids*, 61(10):2047 – 2066, 2013.

[23] Z. Kang and X. Wang. Topology optimization of bending actuators with multilayer piezoelectric material. *Smart Materials and Structures*, 19(7):075018, 2010.

[24] G. Kofod, P. Sommer-Larsen, R. Kornbluh, and R. Pelrine. Actuation response of polyacrylate dielectric elastomers. *Journal of Intelligent Material Systems and Structures*, 14(12):787–793, 2003.

[25] M. Kögl and E. Silva. Topology optimization of smart structures: Design of piezoelectric plate and shell actuators. *Smart Materials and Structures*, 14:387–399, 2005.

[26] Victor Lefèvre and Oscar Lopez-Pamies. Nonlinear electroelastic deformations of dielectric elastomer composites: I—ideal elastic dielectrics. *Journal of the Mechanics and Physics of Solids*, 99:409 – 437, 2017.

[27] B. Li, L. Liu, and Z. Suo. Extension limit, polarization saturation, and snap-through instability of dielectric elastomers. *International Journal of Smart and Nano Materials*, 2(2):59–67, 2011.

[28] T. Li, C. Keplinger, R. Baumgartner, S. Bauer, W. Yang, and Z. Suo. Giant voltage-induced deformation in dielectric elastomers near the verge of snap-through instability. *Journal of the Mechanics and Physics of Solids*, 61(2):611–628, 2013.

[29] Kun Liu, Shitong Chen, Feifei Chen, and Xiangyang Zhu. A unidirectional soft dielectric elastomer actuator enabled by built-in honeycomb metastructures. *Polymers*, 12(3), 2020.

[30] C. Lundgaard and O. Sigmund. A density-based topology optimization methodology for thermoelectric energy conversion problems. *Structural and Multidisciplinary Optimisation*, 57:1427–1442, 2018.

[31] C. Lundgaard and O. Sigmund. Design of segmented off-diagonal thermoelectric generators using topology optimization. *Applied Energy*, 236:950–960, 2019.

[32] C. Lundgaard and O. Sigmund. Design of segmented thermoelectric peltier coolers by topology optimization. *Applied Energy*, 239:1003–1013, 2019.

[33] F. Marín, J. Martínez-Frutos, R. Ortigosa, and A. J. Gil. A convex multi-variable based computational framework for multilayered electro-active polymers. *Computer Methods in Applied Mechanics and Engineering*, 374:113567, 2021.

[34] R. M. McMeeking and C. M. Landis. Electrostatic forces and stored energy for deformable dielectric materials. *Journal of Applied Mechanics*, 72(4):581–590, 2008.

[35] D. J. Munk and G. P. Steven. Topology and shape optimization methods using evolutionary algorithms: a review. *Structural and Multidisciplinary Optimization*, 52:613–631, 2015.

[36] S.S. Nanthakumar, Tom Lahmer, Xiaoying Zhuang, Harold S. Park, and Timon Rabczuk. Topology optimization of piezoelectric nanostructures. *Journal of the Mechanics and Physics of Solids*, 94:316 – 335, 2016.

[37] A. O'Halloran, F. O'Malley, and P. McHugh. A review on dielectric elastomer actuators, technology, applications, and challenges. *Journal of Applied Physics*, 104(7):071101, 2008.

[38] R. Ortigosa, M. Franke, A. Janz, A.J. Gil, and P. Betsch. An energy–momentum time integration scheme based on a convex multi-variable framework for non-linear electro-elastodynamics. *Computer Methods in Applied Mechanics and Engineering*, 339:1–35, 2018.

[39] R. Ortigosa and A. J. Gil. A new framework for large strain electromechanics based on convex multi-variable strain energies: Conservation laws, hyperbolicity and extension to electro-magneto-mechanics. *Computer Methods in Applied Mechanics and Engineering*, 309:202–242, 2016.

[40] R. Ortigosa and A. J. Gil. A new framework for large strain electromechanics based on convex multi-variable strain energies: Finite element discretisation and computational implementation. *Computer Methods in Applied Mechanics and Engineering*, 302:329–360, 2016.

[41] R. Ortigosa, A. J. Gil, and C. H. Lee. A computational framework for large strain nearly and truly incompressible electromecahnics based on convex multi-variable strain energies. *Computer Methods in Applied Mechanics and Engineering*, 310:297–334, 2016.

[42] R. Ortigosa, J. Martínez-Frutos, A. J. Gil, and D. Herrero-Pérez. A new stabilisation approach for level-set based topology optimisation of hyperelastic materials. *Structural and Multidisdiplinary Optimization*, 60:2343–2371, 2019.

[43] Suntak Park, Bongje Park, Saekwang Nam, Sungryul Yun, Seung Koo Park, Seongcheol Mun, Jeong Mook Lim, Yeonghwa Ryu, Seok Ho Song, and Ki-Uk Kyung. Electrically tunable binary phase fresnel lens based on a dielectric elastomer actuator. *Opt. Express*, 25(20):23801–23808, Oct 2017.

[44] R. Pelrine, R. Kornbluh, and J. Joseph. Electrostriction of polymer dielectrics with compliant electrodes as a means of actuation. *Sensors and Actuators A: Physical*, 64(1):77–85, 1998.

[45] R. Pelrine, R. Kornbluh, Q. Pei, and J. Joseph. High-speed electrically actuated elastomers with strain greater than 100 %. *Science*, 287(5454):836–839, 2000.

[46] R. Pelrine, R. Kornbluh, Q. Pei, S. Stanford, S. Oh, J. Eckerle, R. J. Full, M. A. Rosenthal, and K. Meijer. Dielectric elastomer artificial muscle actuators: toward biomimetic motion. In *Smart Structures and Materials 2002: Electroactive Polymer Actuators and Devices (EAPAD)*, volume 4695, pages 126 – 137. International Society for Optics and Photonics, SPIE, 2002.

[47] R. Poya, A. J. Gil, R. Ortigosa, R. Sevilla, J. Bonet, and W. A. Wall. A curvilinear high order finite element framework for electromechanics: From linearised electro-elasticity to massively deformable dielectric elastomers. *Computer Methods in Applied Mechanics and Engineering*, 329:75–117, 2018.

[48] D. Ruiz, J. Bellido, and A. Donoso. Design of piezoelectric modal filters by simultaneously optimizing the structure layout and the electrode profile. *Structural and Multidisciplinary Optimization*, 53:715–730, 2015.

[49] D. Ruiz, J. Bellido, A. Donoso, and J.L. Sanchez-Rojas. Design of in-plane piezoelectric sensors for static response by simultaneously optimizing the host structure and the electrode profile. *Structural and Multidisciplinary Optimization*, 48:1023–1026, 2013.

[50] D. Ruiz, Alex Díaz-Molina, O. Sigmund, A. Donoso, J. Bellido, and J.L. Sánchez-Rojas. Optimal design of robust piezoelectric unimorph microgrippers. *Applied Mathematical Modelling*, 55:1–12, 2018.

[51] D. Ruiz and O. Sigmund. Optimal design of robust piezoelectric microgrippers undergoing large displacements. *Structural and Multidisciplinary Optimization*, 55:71–82, 2018.

[52] X. Zhao S. Yang and P. Sharma. Avoiding the pull-in instability of a dielectric elastomer film and the potential for increased actuation and energy harvesting. *Soft Matter*, 13:4552–4558, 2017.

[53] J.L. Sánchez-Rojas, J Hernando, A Donoso, J. Bellido, T. Manzaneque, A. Ababneh, H. Seidel, and U. Schmid. Modal optimization and filtering in piezoelectric microplate resonators. *Journal of Micromechanics and Microengineering*, 20:055027, 2010.

[54] J. Schröder. Anisotropic polyconvex energies. In J. Schröder and P. Neff, editors, *Poly-, quasi- and rank-one convexity in Applied Mechanics, volume 516 of CISM Courses and Lectures*, volume 516 of CISM Courses and Lectures, pages 53–105. Springer-Verlag, 2010.

[55] Samuel Shian, Roger M. Diebold, and David R. Clarke. Tunable lenses using transparent dielectric elastomer actuators. *Opt. Express*, 21(7):8669–8676, Apr 2013.

[56] M. H. Siboni and P. P. Castañeda. Fiber-constrained, dielectric-elastomer composites: Finite-strain response and stability analysis. *Journal of the Mechanics and Physics of Solids*, 68(0):211–238, 2014.

[57] Morteza H. Siboni and Pedro Ponte Castañeda. Fiber-constrained dielectric elastomer composites: Finite deformation response and instabilities under non-aligned loadings. *International Journal of Solids and Structures*, 184:73 – 98, 2020. Physics and Mechanics of Random Structures: From Morphology to Material Properties.

[58] A. L. Skov, O. Pei, D. Opris, R. J. Spontak, G. Gallone, H. Shea, and M. Y. Benslimane. *Dielectric Elastomers (DEs) as EAPs: Materials*, pages 1–28. Springer International Publishing, Cham, 2016.

[59] J. Sokolowski and A. Zochowski. On the topological derivative in shape optimization. *SIAM Journal on Control and Optimisation*, 37:1251–1272, 1999.

[60] Akihiro Takezawa, Shinji Nishiwaki, and Mitsuru Kitamura. Shape and topology optimization based on the phase field method and sensitivity analysis. *Journal of Computational Physics*, 229(7):2697 – 2718, 2010.

[61] D. K. Vu, P. Steinmann, and G. Possart. Numerical modelling of non-linear electroelasticity. *International Journal for Numerical Methods in Engineering*, 70(6):685–704, 2007.

[62] M. Wang, X. Wang, and D. Guo. A level-set method for structural topology optimization. *Computer Methods in Applied Mechanics and Engineering*, 192:227–246, 2003.

[63] N. Wang, H. Guo, B. Chen, and X. Zhang. Design of a rotary dielectric elastomer actuator using topology optimization method. In *2017 International Conference on Manipulation, Automation and Robotics at Small Scales (MARSS)*, pages 1–6, July 2017.

[64] X. Zhang, A. Takezawa, and Z. Kang. Topology optimization of piezoelectric smart structures for minimum energy consumption under active control. *Structural and Multidisciplinary Optimization*, 58:185–199, 2018.

[65] J. Zhou, W. Hong, X. Zhao, Z. Zhang, and Z. Suo. Propagation of instability in dielectric elastomers. *International Journal of Solids and Structures*, 45(13):3739–3750, 2008.

[66] M. Zhou and G. Rozvany. The coc algorithm, part II: topological, geometrical and generalized shape optimization. *Computer Methods in Applied Mechanics and Engineering*, 89:309–336, 1991.